Royal Norwegian Council
for Scientific and Industrial Research
(NTNF)

NORSAR

NORSAR Scientific Report No. 1-88/89

Final Technical Summary

1 April – 30 September 1988

L.B. Loughran (ed.)

Kjeller, December 1988

UNCLASSIFIED
SECURITY CLASSIFICATION OF THIS PAGE

REPORT DOCUMENTATION PAGE

Form Approved
OMB No. 0704-0188

1a. REPORT SECURITY CLASSIFICATION UNCLASSIFIED	1b. RESTRICTIVE MARKINGS NOT APPLICABLE
2a. SECURITY CLASSIFICATION AUTHORITY NOT APPLICABLE	3. DISTRIBUTION/AVAILABILITY OF REPORT APPROVED FOR PUBLIC RELEASE DISTRIBUTION UNLIMITED
2b. DECLASSIFICATION/DOWNGRADING SCHEDULE NOT APPLICABLE	
4. PERFORMING ORGANIZATION REPORT NUMBER(S) Scientific Rep. 1-88/89	5. MONITORING ORGANIZATION REPORT NUMBER(S) Scientific Rep. 1-88/89
6a. NAME OF PERFORMING ORGANIZATION NTNF/NORSAR 6b. OFFICE SYMBOL (If applicable)	7a. NAME OF MONITORING ORGANIZATION HQ/AFTAC/TTS
6c. ADDRESS (City, State, and ZIP Code) Post Box 51 N-2007 Kjeller, Norway	7b. ADDRESS (City, State, and ZIP Code) Patrick AFB, FL 32925-6001
8a. NAME OF FUNDING/SPONSORING ORGANIZATION Defence Advanced Research Projects Agency 8b. OFFICE SYMBOL (If applicable) NMRO	9. PROCUREMENT INSTRUMENT IDENTIFICATION NUMBER Contract No. F08606-86-C-0004
8c. ADDRESS (City, State, and ZIP Code) 1400 Wilson Blvd. Arlington, VA 22209-2308	10. SOURCE OF FUNDING NUMBERS PROGRAM ELEMENT NO.: R&D PROJECT NO.: NORSAR PHASE 3 TASK NO: SOW TASK 5.0 WORK UNIT ACCESSION NO.: SEQUENCE No.003A2

11. TITLE (Include Security Classification)

FINAL TECHNICAL SUMMARY, 1 APRIL - 30 SEPTEMBER 1988 (UNCLASSIFIED)

12. PERSONAL AUTHOR(S)

L.B. Loughran (ed.)

13a. TYPE OF REPORT	13b. TIME COVERED	14. DATE OF REPORT (Year, Month, Day)	15. PAGE COUNT
SCIENTIFIC SUMMARY	FROM 1 Apr TO 30 Sep 88	December 1988	106

16. SUPPLEMENTARY NOTATION

NOT APPLICABLE

17. COSATI CODES			18. SUBJECT TERMS (Continue on reverse if necessary and identify by block number)
FIELD	GROUP	SUB-GROUP	
8	11		NORSAR, NORWEGIAN SEISMIC ARRAY

19. ABSTRACT (Continue on reverse if necessary and identify by block number)

This Final Technical Summary describes the operation, maintenance and research activities at the Norwegian Seismic Array (NORSAR), NORESS and ARCESS for the period 1 April - 30 September 1988.

(Continued on reverse side)

20. DISTRIBUTION/AVAILABILITY OF ABSTRACT ☒ UNCLASSIFIED/UNLIMITED ☐ SAME AS RPT. ☐ DTIC USERS	21. ABSTRACT SECURITY CLASSIFICATION UNCLASSIFIED
22a. NAME OF RESPONSIBLE INDIVIDUAL MR. LEE BRIDGES	22b. TELEPHONE (Include Area Code) (407) 494-7765 22c. OFFICE SYMBOL AFTAC/TTS

DD Form 1473, JUN 86 Previous editions are obsolete. SECURITY CLASSIFICATION OF THIS PAGE

Abstract (cont.)

The NORSAR Dectection Processing System has been operated throughout the reporting period with an average uptime of 98.2 per cent. A total of 1958 seismic events has been reported in the NORSAR monthly seismic bulletin. The performance of the continuous alarm system and the automatic bulletin transfer by telex to AFTAC has been satisfactory. Processing of requests for full NORSAR/NORESS data on magnetic tapes has progressed according to established schedules.

The satellite link for transmitting NORESS data in real time to the U.S. has had an average uptime of 99.3 per cent. On-line NORESS detection processing and data recording at the NORSAR Data Center (NDPC) has been conducted throughout the period, with an average uptime of 97.8 per cent.

The ARCESS array started operation in mid-October 1987, and the data were initially recorded and processed at NDPC using a Sun 2-based computer system. In May/June 1988, this system experienced significant hardware problems, and the time schedule for the planned change to a Sun 3 system was therefore accelerated. The changeover was successfully completed in early July. Average recording time for ARCESS was 77.2% for the total reporting period, and 91 per cent when disregarding the May/June period.

Field maintenance activity has included regular preventive maintenance at all array sites and occasional corrective actions when required. In particular, much work has been conducted at the ARCESS array site, including installation of a new Global Positioning System synchronized clock in cooperation with Sandia personnel and removal of the KS-36000 borehole seismometer for repair. The NORSAR and NORESS field systems performed entirely satisfactorily throughout the reporting period.

A considerable effort has been expended in upgrading the on-line and off-line detection/event processing software which is being developed at NORSAR for general array applications. The program systems have been tested on data from NORSAR, NORESS, ARCESS, FINESA and Gräfenberg, and the implementation will be coordinated with the Intelligent Array System developments.

A study of Lg spectra of NORSAR-recorded explosions from the Shagan River test area near Semipalatinsk, USSR, has shown that the main energy in the Lg wavetrain is confined to the frequency range 0.6-1.0 Hz. There is some evidence of source size scaling effects (i.e., lower dominant Lg frequency for larger events), but the variation is small and appears to be of little significance in RMS Lg magnitude

estimation. The Lg spectra show no significant differences for events from the two portions of the test site (NE Shagan and SW Shagan). On the other hand, the spectral difference between early P coda and Lg is larger for SW events than for NE events, and this holds true in the entire frequency band 0.6-3.0 Hz.

An analysis has been made of statistics on P, PcP, PKP and PKKP travel time residuals with respect to the isotropic PREM earth model using ISC bulletin data for the years 1964-1984 as well as other data sources. The scatter in the residuals is significantly greater for shallow events than for deep events. For P phases at distances less than 65^{o} this increased scatter reflects increases in number of "early" as well as "late" arrivals, whereas for more distant P phases and other phases the increase in scatter is dominated by a larger number of late arrivals. The statistics further show that after applying the isotropic PREM model there is still a significant mean residual left in the data, and this is particularly pronounced for core phases.

The coupling mode technique for modelling surface wave propagation in 2-D structures presented in previous Semiannual Technical Summaries has been applied to a model of the North Sea Graben. The purpose has been to examine how a large-scale and very strong lateral variation of the crustal structure affects the propagation of the short-period surface wavetrains. Our continued work has confirmed the conclusions given in earlier reports. Thus, our numerical modelling of Lg wave propagation in a simplified model of the North Sea Central Graben does not predict the severe attenuation of the wavetrain actually observed in this region. On the contrary, the Lg wavetrain appears very robust when crossing a zone where its waveguide is strongly deformed. Since the large-scale geometry of the Graben fails to explain the observed data, it is suggested that future work explore alternative explanations for the observed attenuation, such as scattering by 2D or 3D basaltic intrusions in the lower crust, extensive faulting associated with intra-fault weak material, or more rheological aspects of this problem.

A detailed analysis has been made of the recent (August 8, 1988) earthquake offshore Norway, which was recorded at NORSAR, NORESS, ARCESS as well as a large number of stations at regional and teleseismic distances. This earthquake is the largest in the region for at least 30 years, with an estimated $m_b = 5.2$. Our focal mechanism solution indicates thrust faulting along a NNE-SSW striking fault plane, in response to E-W compressional stress. The seismic moment has been estimated at 10^{17} Nm, with indications of scaling consistent with an ω-square source model. A major source of uncertainty in this analysis is tied to the lack of accurate knowledge of the anelastic attenuation.

In cooperation with the University of Helsinki, an analysis has been conducted of events recorded by the three regional arrays in Fennoscandia (NORESS, ARCESS, FINESA). The latter array has been reconfigured to closely resemble the subgeometry of NORESS and ARCESS obtained when excluding the D-ring. As a first part of this study, the detection capabilities of the upgraded FINESA configuration, using the RONAPP algorithm, was investigated. The results were excellent, in that 98 out of 103 reference events (listed in the Helsinki bulletin) had at least one detected P or S phase at FINESA. Many additional events were also detected. The second part of the study has addressed the location capabilities of the three-array network, again using the Helsinki bulletin as a reference for comparison. On the average, joint three-array locations deviate from the reference location by only 16 km, whereas comparable deviations using one or two arrays for location purposes were 68 and 26 km, respectively. Since the arrival times used were those determined automatically by on-line processing, there are clear possibilities for further improvements in multi-array location accuracy. This could be achieved both through more accurate readings, introduction of more detailed regionalized travel-time tables and application of master-event location techniques.

As a continuation of earlier studies on Lg magnitudes and yield estimation of Semipalatinsk explosions, we have now completed the analysis of all available Gräfenberg Lg recordings of large Shagan River explosions. Because of the varying number of channels available and the relatively large systematic variations in Lg amplitudes across the array, we have used station correction terms for individual channels when computing average magnitudes. The resulting values show excellent correspondence with NORSAR Lg, with the standard deviation of magnitude differences between the two arrays being about 0.03 units for well-recorded events (more than 5 of the 13 GRF channels available). We have also investigated the effect of applying individual instrument correction terms to NORSAR Lg data and have found the effects to be modest. A study comparing joint NORSAR/Gräfenberg Lg magnitudes to maximum-likelihood m_b based on ISC data has confirmed the pattern previously observed, i.e., a low P-Lg bias for NE Shagan in comparison to SW Shagan. The JVE explosion of 14 September 1988 had a P-Lg bias close to the average for the SW Shagan event set. This explosion was estimated at m(Lg) = 5.97 at both NORSAR and Gräfenberg.

AFTAC Project Authorization	:	T/6141/B/PMP
ARPA Order No.	:	4138
Program Code No.	:	0F10
Name of Contractor	:	Royal Norwegian Council for Scientific and Industrial Research
Effective Date of Contract	:	1 October 1985
Contract Expiration Date	:	30 September 1988
Project Manager	:	Frode Ringdal (06) 81 71 21
Title of Work	:	The Norwegian Seismic Array (NORSAR) Phase 3
Amount of Contract	:	$ 3,702,816
Contract Period Covered by Report	:	1 Apr - 30 Sep 1988

The views and conclusions contained in this document are those of the authors and should not be interpreted as necessarily representing the official policies, either expressed or implied, of the Defense Advanced Research Projects Agency, the Air Force Technical Applications Center or the U.S. Government.

This research was supported by the Advanced Research Projects Agency of the Department of Defense and was monitored by AFTAC, Patrick AFB, FL 32925, under contract no. F08606-86-C-0004.

NORSAR Contribution No. 405

TABLE OF CONTENTS

		Page
I.	SUMMARY	1
II.	NORSAR OPERATION	3
II.1	Detection Processor (DP) operation	3
II.2	Array communications	7
II.3	Event Detection operation	11
III.	OPERATION OF NORESS AND ARCESS	12
III.1	Satellite transmission of NORESS data to the U.S.	12
III.2	Recording of NORESS data at NDPC, Kjeller	13
III.3	Recording of ARCESS data at Kjeller	17
IV.	IMPROVEMENTS AND MODIFICATIONS	20
IV.1	NORSAR detection processing	20
IV.2	MODCOMP subarray communication	20
IV.3	NORSAR event processing	20
IV.4	NORESS detection processing	20
IV.5	ARCESS detection processing	21
IV.6	Event processing	21
IV.7	Upgrade of the ARCESS data acquisition and processing hardware	22
V.	MAINTENANCE ACTIVITIES	23
V.1	Activities in the field and at the Maintenance Center	23
V.2	Array status	27
VI.	DOCUMENTATION DEVELOPED	29

TABLE OF CONTENTS
(cont.)

			Page
VII.	SUMMARY OF TECHNICAL REPORTS / PAPERS PUBLISHED		30
	VII.1	Spectral analysis of Shagan River explosions recorded at NORSAR and NORESS	30
	VII.2	Statistics of ISC travel time residuals	42
	VII.3	Modelling of Lg-wave propagation across the Central Graben of the North Sea	48
	VII.4	The August 8, 1988, Møre Basin earthquake: Observed ground motions and inferred source parameters	62
	VII.5	Analysis of regional seismic events using the NORESS/ARCESS/FINESA arrays	74
	VII.6	Comparative analysis of NORSAR and Gräfenberg Lg magnitudes for Shagan River explosions	88

I. SUMMARY

This Final Technical Summary describes the operation, maintenance and research activities at the Norwegian Seismic Array (NORSAR), Norwegian Regional Seismic Array (NORESS) and the Arctic Regional Seismic Array (ARCESS) for the period 1 April - 30 September 1988.

The NORSAR Detection Processing System has been operated throughout the reporting period with an average uptime of 98.2 per cent. A total of 1968 seismic events have been reported in the NORSAR monthly seismic bulletin. The performance of the continuous alarm system and the automatic bulletin transfer by telex to AFTAC has been satisfactory. Processing of requests for full NORSAR/NORESS data on magnetic tapes has progressed according to established schedules.

The satellite link for transmitting NORESS data in real time to the U.S. has had an average uptime of 99.3 per cent. On-line NORESS detection processing and data recording at the NORSAR Data Center (NDPC) has been conducted throughout the period, with an average uptime of 97.8 per cent.

The ARCESS array started operation in mid-October 1987, and the data were initially recorded and processed at NDPC using a Sun 2-based computer system. In May/June 1988, this system experienced significant hardware problems, and the time schedule for the planned change to a Sun 3 system was therefore accelerated. The changeover was successfully completed in early July. Average recording time for ARCESS was 77.2% for the total reporting period, and 91 per cent when disregarding the May/June period.

Field maintenance activity has included regular preventive maintenance at all array sites and occasional corrective actions when required. In particular, much work has been conducted at the ARCESS array site, including installation of a new Global Positioning System (GPS) synchronized clock in cooperation with Sandia engineers and removal of the KS-36000 borehole seismometer for repair. The NORSAR and NORESS

field systems performed entirely satisfactorily throughout the reporting period.

A considerable effort has been expended in upgrading the on-line and off-line detection/event processing software which is being developed at NORSAR for general array applications. The program systems have been tested on data from NORSAR, NORESS, ARCESS, FINESA and Gräfenberg, and the implementation will be coordinated with the Intelligent Array System developments.

The research activity is summarized in Section VII. Section VII.1 gives results from analysis of P coda and Lg spectra of Shagan River explosions recorded at NORSAR and NORESS. Statistics of ISC travel time residuals in comparison to the PREM model are presented in Section VII.2. Section VII.3 reports on modelling of Lg-wave propagation across the Central Graben of the North Sea, while observed ground motions and inferred source parameters for the August 8, 1988, Møre Basin earthquake are discussed in Section VII.4. An analysis of regional seismic events using the NORESS/ARCESS/FINESA arrays is presented in Section VII.5. In Section VII.6 results of a comparative analysis of NORSAR and Gräfenberg Lg magnitudes for Shagan River explosions are given.

II. NORSAR OPERATION

II.1 Detection Processor (DP) Operation

There have been 54 breaks in the otherwise continuous operation of the NORSAR online system within the current 6-month reporting interval. The uptime percentage for the period is 98.2 as compared to 96.9 for the previous period.

Fig. II.1.1 and the accompanying Table II.1.1 both show the daily DP downtime for the days between 1 April and 30 September 1988. The monthly recording times and percentages are given in Table II.1.2.

The breaks can be grouped as follows:

a)	Hardware failure	7
b)	Stops related to program work or error	0
c)	Hardware maintenance stops	1
d)	Power jumps and breaks	6
e)	TOD error correction	15
f)	Communication lines	25

The total downtime for the period was 80 hours and 4 minutes. The mean-time-between-failures (MTBF) was 3.3 days, as compared to 1.3 for the previous period.

J. Torstveit

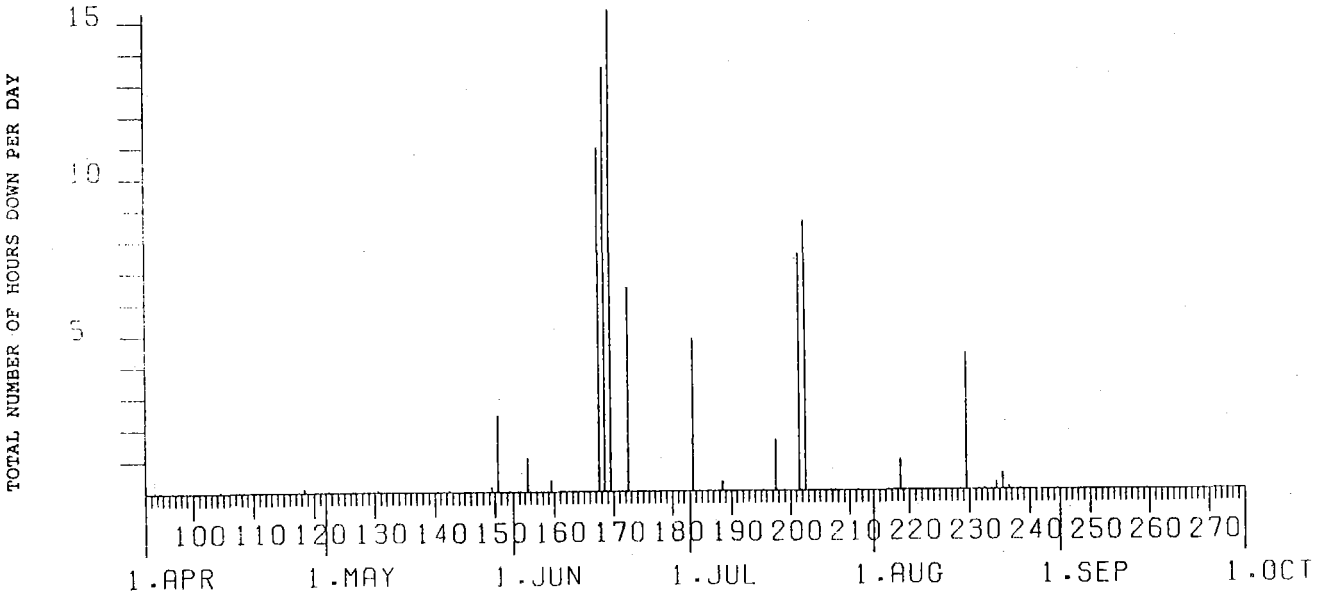

Fig. II.1.1. Detection Processor downtime in the period 1 April - 30 September 1988.

LIST OF BREAKS IN DP PROCESSING THE LAST HALF-YEAR

DAY	START		STOP		COMMENTS.....
93	9	56	9	57	LINE FAILURE
94	6	1	6	2	lINE FAILURE
96	6	1	6	2	TOD RETARED 20MS
97	9	0	9	2	LINE FAILURE
99	5	57	5	58	LINE FAILURE
101	19	57	19	58	LINE FAILURE
104	6	1	6	2	TOD RETARED 10MS
104	9	10	9	13	LINE FAILURE
111	6	1	6	2	TOD RETARED 17MS
118	11	3	11	10	TOD RETARED 10MS
122	14	40	14	43	LINE FAILURE
126	8	40	8	41	TOD RETARED 20MS
130	7	19	7	21	LINE FAILURE
130	8	26	8	27	LINE FAILURE
132	8	29	8	30	LINE FAILURE
139	7	0	7	1	LINE FAILURE
140	5	12	5	16	LINE FAILURE
141	6	1	6	2	TOD RETARED 10MS
142	14	28	14	31	LINE FAILURE
145	6	1	6	2	TOD RETARED 12MS
149	11	14	11	23	MODCOMP FAILURE
150	16	26	18	51	POWER FAILURE
155	14	0	15	5	MODCOMP FAILURE
159	8	20	8	40	DISK FAILURE
159	9	12	9	13	LINE FAILURE
167	13	4	24	0	2701 FAILURE
168	0	0	13	30	2701 FAILURE
169	4	24	19	44	2701 FAILURE
172	6	20	12	48	2701 FAILURE
183	1	56	6	47	POWER FAILURE
186	6	1	6	2	TOD RETARED 13 MS
188	7	29	7	48	CE MAINTENANCE 2701
195	6	21	6	22	TOD RETARED 23MS
197	18	30	20	7	POWER FAILURE
201	16	30	17	30	POWER FAILURE
201	17	30	24	0	MODCOMP FAILURE

DAY	START		STOP		COMMENTS.....
202	0	0	8	34	MODCOMP FAILURE
217	9	50	9	51	LINE FAILURE
218	2	33	3	31	POWER FAILURE
221	6	2	6	3	TOD RETARED 46MS
228	9	29	9	30	LINE FAILURE
229	13	30	17	50	POWER FAILURE
231	5	33	5	34	LINE FAILURE
232	7	10	7	12	LINE FAILURE
234	10	2	10	16	LINE FAILURE
235	6	18	6	20	LINE FAILURE
235	11	25	11	52	LINE FAILURE
235	12	3	12	4	LINE FAILURE
236	6	0	6	3	TOD RETARED 12MS
236	13	28	13	31	LINE FAILURE
238	13	20	13	21	LINE FAILURE
238	15	44	15	45	LINE FAILURE
239	8	30	8	31	LINE FAILURE
244	6	2	6	3	TOD RETARED 15MS
250	6	1	6	2	TOD RETARED 16MS
259	6	1	6	2	TOD RETARED 22MS
274	7	1	7	2	TOD RETARED 14MS

Table II.1.1. Daily DP downtime in the period 1 April - 30 September 1988.

Month	DP Uptime hours	DP Uptime %	No. of DP Breaks	No. of Days with Breaks	DP MTBF* (days)
APR 88	719.41	99.9	10	9	2.8
MAY	741.08	99.6	12	11	2.4
JUN	672.20	93.4	6	6	4.0
JUL	721.07	96.9	6	7	4.3
AUG	737.42	99.2	17	13	1.7
SEP	719.57	100.0	3	3	7.5

* Mean-time-between-failures = total uptime/no. of up intervals.

Table II.1.2. Online system performance, 1 April - 30 September 1988.

II.2 Array communications

Table II.2.2 reflects the performance of the system through the reporting period. All the subarrays except 01A have been affected by occasional communication outages. Problems encountered have connection with bad communication cables in the ground and on poles, lack of power and carrier system outages. Also other irregularities have contributed to errors and shorter outages, such as failing CTV equipment like modems and SLEMS.

In addition, there were problems with 02B (telemetry) antennas caused by heavy snowfall. The antennas were repaired in April.

April (weeks 9-13), 4.4 - 1.5.88
02B was still out of operation, although NTA/Hamar declared the line operational 13 April. Danger of snowslides prevented the power plant people from repairing the broken power line.

02B (telemetry) is not dependent upon external power (supplied by solar cells), and resumed operation (partly) with channels 23, 24, 25 and 27 active. Channel 26 and 28 were "dead" but the NMC staff repaired the antennas (14, 15 and 25 April) related to these channels. The antennas had been broken after heavy snowfalls in the area.

06C was affected by a power outage week 15.

The performance of the remaining NORSAR communications systems was most satisfactory.

May (weeks 18-22), 2.5 - 5.6.88
02B remained down also in May, and 06C had its modem/SLEM checked and tested.

The remaining communications system was almost free from errors.

June (weeks 23-26), 6.6 - 3.7.88

02B resumed operation week 25 after having been down since November 1987.

All communications systems were affected for about 1 hour 20 June in connection with a broken coaxial cable at Kjeller, which among other things carried the NORSAR subarrays and NORESS. 01A and 01B resumed operation after a couple of hours, while 02C-04C were operational a few hours later in the afternoon, 06C the next morning.

On 15 June the IBM 2701 communications adapter failed. This machine interfaces the Modcomp to the IBM 4341 via two highspeed modems. On 20 June the source of the failure was identified and the problem corrected. In the meantime, the Modcomp had to be stopped/started each time a card in the 2701 was replaced, or other actions implemented as part of the fault-finding procedure.

Apart from the interruptions mentioned above, the communications systems were reliable in June.

July (weeks 27-30), 4 - 31.7.88

Also throughout this period the systems performance was most satisfactory. An exception was 02B where NTA/Hamar found the line toward the CTV had failed and 06C which had line problems in connection with lightning.

August (weeks 31-35), 1.8 - 4.9.88

The NTA coaxial carrier cable was broken 19 August causing significant problems weeks 33 and 34. All subarrays were affected (01A for a very short period).

01B, which had been down since 15 July due to a bad cable was back in operation 1 September.

The remaining systems (except for 02B, 03C) were back in operation 22 August.

02B, 03C resumed operation later due to a SLEM-failure (02B) and a cable problem (03C).

September (weeks 36-39), 5.9 - 2.10.88

Generally satisfactory performance, in spite of problems such as a damaged cable after lightning (02B) between 30 September and 4 October, carrier system outages affecting 03C, 04C 25 September, and between 30 September and 1 October.

06C was affected totally 85.71 minutes weeks 37 and 38.

O.A. Hansen

Sub-array	APR (4) (4.4-1.5)	MAY (5) (2.5-5.6)	JUN (4) (6.6-3.7)	JUL (4) (4-31.7)	AUG (5) (1.8-5.9)	SEP (4) (5.9-2.10)	AVERAGE 1/2 YEAR
01A	0.02	0.003	0.16	0.02	0.01	0.04	0.04
01B	0.02	0.001	0.15	*58.93	*89.64	0.03	7) 0.05
02B	*100.00	*100.00	*59.83	0.03	2) 0.02	6) 0.05	8) 0.03
02C	0.02	0.002	0.15	0.02	3) 0.45	0.03	0.11
03C	0.02	0.005	0.17	0.02	4) 0.01	*1.87	0.35
04C	0.02	0.09	0.16	0.02	5) 0.01	*1.83	0.35
06C	1) 0.001	0.83	2.61	*10.28	*25.92	0.43	9) 0.97
AVER	14.29	14.40	9.03	9.90	16.85	0.61	0.27
LESS	02B	02B	02B	01B,06C	01B,06C	02B,03C 04C	01B,02B,06C
	0.02	0.14	0.56	0.02	0.10	0.13	0.21

* See Section II.2 regarding figures preceded by an asterisk.
Figures representing error rate (in per cent) preceded by a number 1), 2), etc., are related to legend below.

1) Average 3 weeks, week 14 N/A
2) -"- 3 weeks, week 33,34 N/A
3) -"- 4 weeks, week 33 N/A
4) -"- 3 weeks, week 33,34 N/A
5) -"- 3 weeks, week 29 N/A
6) Average 3 weeks, week 39 N/A
7) -"- 4 months
8) -"- 3 months
9) -"- 4 months

Table II.2.1 Communications performance. The numbers represent error rates in per cent based on total transmitted frames/week (1 April - 30 September 1988).

II.3 Event Detection operation

In Table II.3.1 some monthly statistics of the Detection and Event Processor operation are given. The table lists the total number of detections (DPX) triggered by the on-line detector, the total number of detections processed by the automatic event processor (EPX) and the total number of events accepted after analyst review (Teleseismic phases, core phases and total).

	Total DPX	Total EPX	Accepted events P-phases	Core Phases	Sum	Daily
APR 88	10825	1135	277	72	349	11.6
MAY 88	5400	941	264	96	360	11.6
JUN 88	6600	910	199	55	254	8.5
JUL 88	8850	1191	295	87	382	12.3
AUG 88	12750	1191	270	71	341	11.0
SEP 88	9075	945	222	60	282	9 4
			1527	441	1968	10.7

Table II.3.1 Detection and Event Processor statistics, October 1987 - March 1988.

B. Paulsen

III. OPERATION OF NORESS AND ARCESS

III.1 Satellite transmission of NORESS data to the U.S.

The satellite transmission of data to the U.S. from the NORESS field installation has generaly been very stable, exept for occasional interruptions due to power breaks and control line breaks. These outage periods are listed in Table III.1.1.

10	Apr	0600 to	0745	power break
20	Apr	0605 to	1310	power break
22	Apr	0617 to	0916	power break
30	Apr	0838 to	1417	power break
4	May	2056 to 5 May	0023	power break
9	May	2100 to 10 May	0321	power break
12	May	2200 to	2317	power break
20	May	1123 to	1124	control lines down
20	Jun	1050 to	1125	control lines down
19	Aug	1200 to	1205	checking out transmitter

Table III.1.1. Outage period for NORESS satellite transmission system April - September 1988.

The total uptime for the NORESS Earth Station for satellite transmission of data to the U.S. was 99.3% as compared to 97.7% for the previous period.

III.2 Recording of NORESS data at NDPC, Kjeller

As can be seen from Table III.2.1 the reasons causing NORESS outage can be placed under the following four groups: Transmission line failure, power failure at HUB, power failure at NDPC and hardware maintenance or failure.

The average recording time was 97.8% as compared to 95.4% for the previous period.

Date	Time	Duration	Cause
18 Apr	1403-1427	24 m	Transmission line failure
20 Apr	0817-1115	4 h 58 m	Power failure at HUB
22 Apr	0826-1047	2 h 21 m	Power failure at HUB
30 Apr	1050-1736	6 h 46 m	Power failure at HUB
4 May	2311-	49 m	Transmission line failure
5 May	-0458	4 h 58 m	Transmission line failure
9 May	2313-	47 m	Power failure at HUB
10 May	-0509	5 h 9 m	Power failure at HUB
10 May	0722-0749	27 m	Power failure at HUB
11 May	0844-1304	4 h 20 m	Hardware maintenance at NDPC
11 May	1308-1309	1 m	Hardware maintenance at NDPC
11 May	1417-1535	1 h 18 m	Hardware maintenance at NDPC
29 May	1626-1846	2 h 20 m	Power failure at NDPC
29 May	1856-1911	15 m	Power failure at NDPC
10 Jun	0501-0615	1 h 14 m	Transmission line failure
20 Jun	1008-1908	9 h 0 m	Transmission line failure
22 Jun	1336-1346	10 m	Transmission line failure
28 Jun	1900-1932	32 m	Transmission line failure
29 Jun	0825-0957	1 h 32 m	Hardware error at NDPC
1 Jul	0156-0304	1 h 8 m	Power failure at NDPC
6 Jul	1016-1254	2 h 38 m	Hardware maintenance at NDPC
14 Jul	2002-2106	1 h 4 m	Transmission line failure
15 Jul	1810-2017	2 h 7 m	Power failure at NDPC
16 Jul	1658-1813	1 h 15 m	Transmission line failure
19 Jul	1653-2037	3 h 44 m	Power failure at NDPC
5 Aug	0248-0404	1 h 16 m	Power failure at NDPC
10 Aug	1046-1102	16 m	Hardware maintenance at NDPC
16 Aug	1330-	10 h 30 m	Hardware failure at NDPC
17 Aug	-1102	11 h 2 m	Hardware failure at NDPC

13 Sep	1630-1842	2 h 12 m	Transmission line failure
13 Sep	1845-1846	1 m	Transmission line failure
15 Sep	1054-1251	1 h 57 m	Power failure at NDPC
20 Sep	0903-1239	3 h 36 m	Hardware maintenance at NDPC
26 Sep	2303-	57 m	Transmission line failure
27 Sep	-0554	5 h 54 m	Transmission line failure
27 Sep	1402-1406	4 m	Hardware maintenance at HUB
27 Sep	1445-1451	6 m	Hardware maintenance at HUB
29 Sep	1124-1146	22 m	Hardware maintenance at HUB
29 Sep	1203-1238	35 m	Hardware maintenance at HUB
29 Sep	1324-1329	5 m	Hardware maintenance at HUB
29 Sep	1409-1410	1 m	Hardware maintenance at HUB
29 Sep	1415-1416	1 m	Hardware maintenance at HUB
29 Sep	1421-1422	1 m	Hardware maintenance at HUB

Table III.2.1. Interruptions in NORESS recordings at NDPC, April - September 1988.

Monthly uptimes for the Noress on-line data recording task, taking into account all factors (field installations, transmissions line, data center operation) affecting this task were as follows:

April	:	98.0%
May	:	97.3%
June	:	98.3%
July	:	98.4%
August	:	96.9%
September	:	97.8%

Fig. III.2.1 shows the uptime for the data recording task, or equivalently, the availability of NORESS data in our tape archive, on a day-by-day basis, for the reporting period.

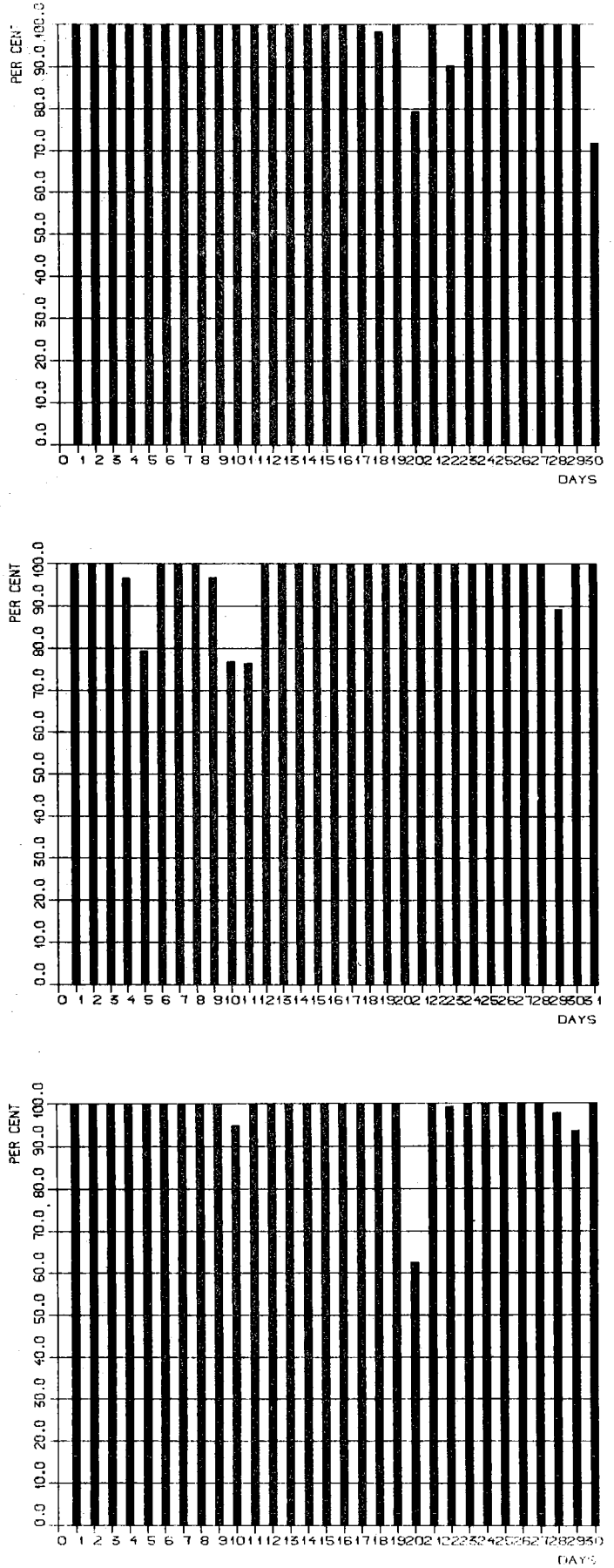

Fig. III.2.1. NORESS data recording uptime for April (top), May (middle) and June 1988 (bottom).

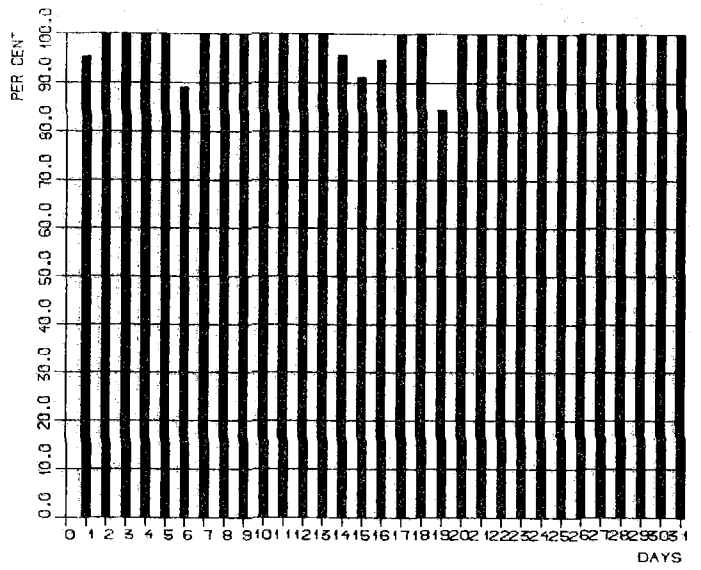

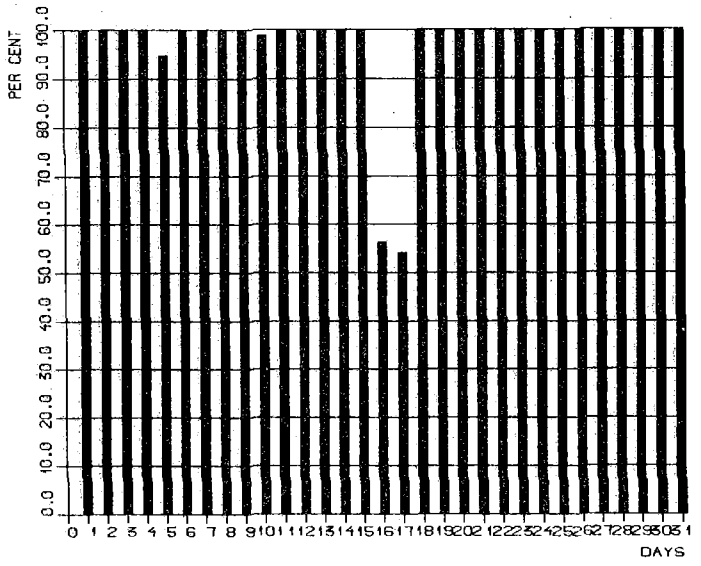

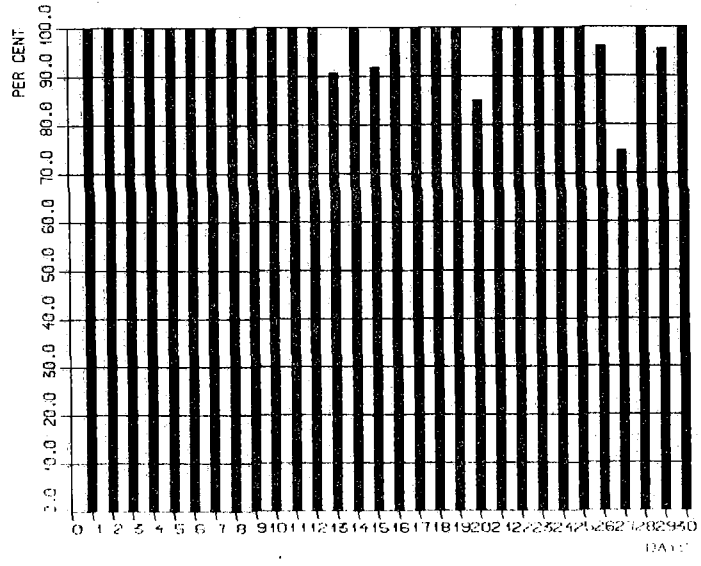

Fig. III.2.1. (cont.) NORESS data recording uptime for July (top), August (middle) and September 1988 (bottom).

III.3 Recording of ARCESS data at NDPC, Kjeller

Monthly uptimes for the ARCESS on-line data recording at NDPC, taking into account all factors (field installations, transmissions line, data center operation) affecting this task were as follows:

April	:	97.2%
May	:	79.6%
June	:	19.6%
July	:	87.8%
August	:	87.0%
September	:	92.0%

The main reason causing most of the ARCESS outage in June was a serious breakdown of the Sun 2 processing system and subsequent work in aonnection with transferring the data recording and processing to a Sun 3-based system. In August work on a new power line at the array site was the main reason for the outages. Other reasons causing outage in the period are: Transmission line failure or line testing, power failure at the HUB or at NDPC, hardware and software work or tests at NDPC.

The average recording time for the period was 77.2%

Fig. III.3.1 shows the uptime for the data recording task, or equivalently, the availability of ARCESS data in our tape archive, on a day-by-day basis, for the reporting period.

J. Torstveit

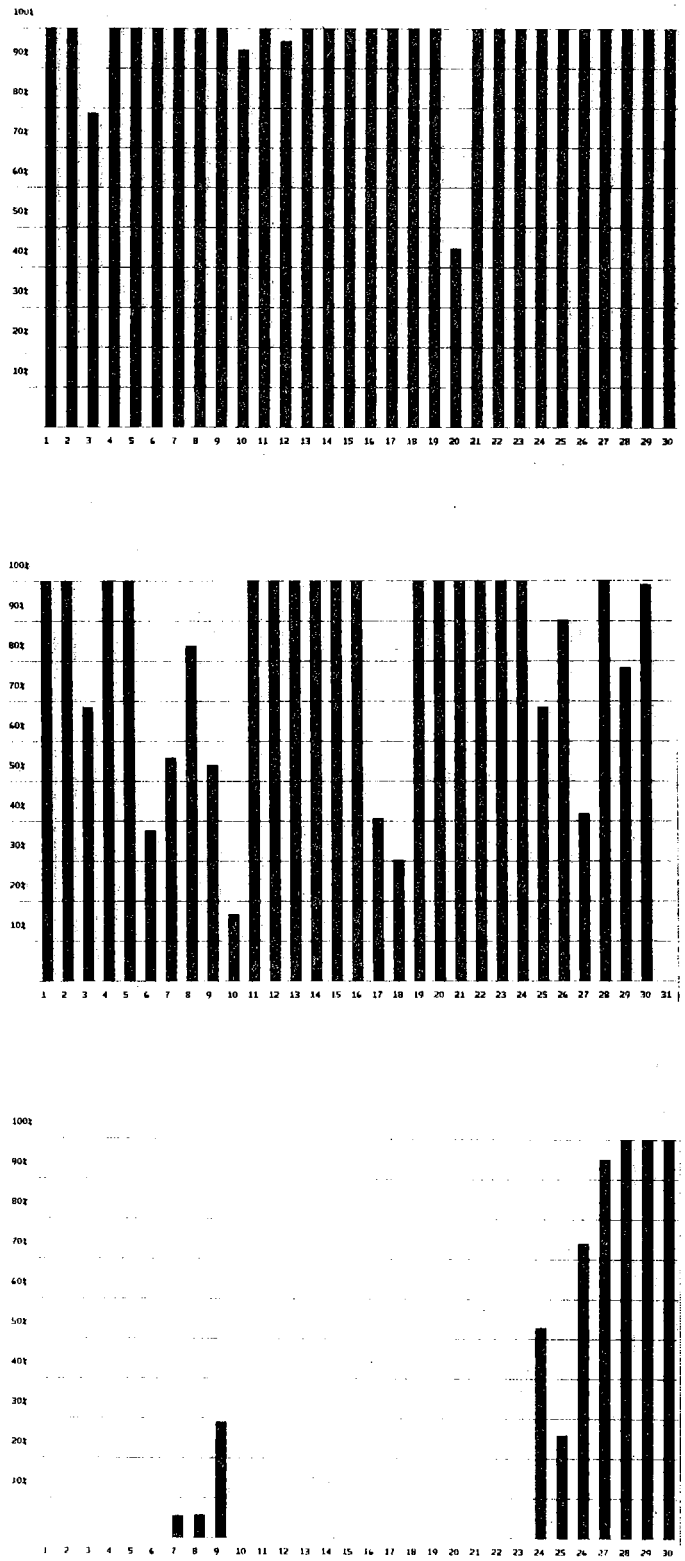

Fig. III.3.1. ARCESS data recording uptime for April (top), May (middle) and June 1988 (bottom).

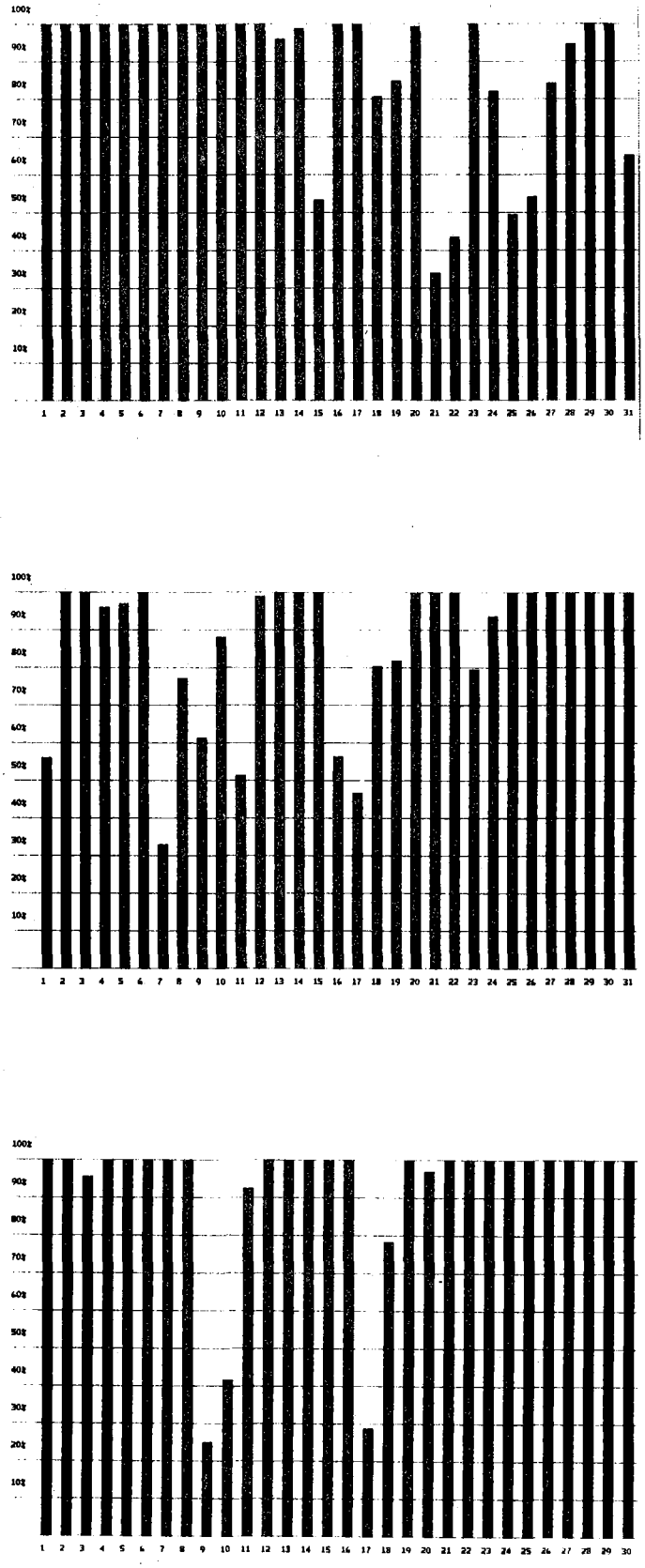

Fig. III.3.1. ARGESS data recording uptime for July (top), August (middle) and September 1988 (bottom).

IV. IMPROVEMENTS AND MODIFICATIONS

IV.1 NORSAR Detection processing

The 'new' NORSAR detection processor has been running satisfactorily during this reporting period. Detection and data quality reports are now grouped into day-files. File names are, e.g., NAO88231.DPX for detections and NAO88231.REP for data quality reports for day-of-year 231 1988. File naming is automatic with file name prefix equal to array code (i.e., NAO for NORSAR, NRS for NORESS, FRS for ARCESS,...).

Detection processing for NORSAR, NORESS, ARCESS, FINESA, GRAFENBERG and other data sources has been executed satisfactorily with the new detector program using a macro language recipe as described in semiannual report No. 2-86/87.

IV.2 MODCOMP subarray communication

No modification has been made to the MODCOMP system.

IV.3 NORSAR event processing

There are no changes in the NORSAR event processor code.

IV.4 NORESS detection processing

There are no changes in the 'online' RONAPP detection processing. Parallel detection processing with various beam sets has been performed to investigate detection capabilities.

IV.5 ARCESS detection processing

Detection processing and f-k analysis for each detection have been performed in an off-line mode for the periods: 1987 (days 306 through 364); 1988 (days 006 through 131 and days 229 through 233). Regular detection processing in near real time has been performed on the Sun system since day 223 of 1988. The automatic data quality control software has been updated to detect and mask channels with data spikes and events within or very close to the ARCESS array.

IV.6 Event processing

A new event processor code is under development, and f-k analysis for NORESS/ARCESS/FINESA has been periodically performed on both IBM and Sun systems.

The event processor package follows the same design as the detection processor with regard to macro language input. The ARRMAN program system which handles input from NORSAR, NORESS, ARCESS, FINESA, Grafenberg, GSE level 2 as well as the CSS 2.8 format, is included in both packages. The package operates on archive tapes, disk files and disk loops, as available. CSS 2.8 is implemented only on the Sun computers, whereas the other formats can be accessed from either IBM or Sun.

NOGRA - NORSAR Graphics package - has been implemented by NTNF/NORSAR for graphics output under IBM/GDDM, IBM/GKS, IBM/PHIGS, Sun/X11 and Sun/Laser. Standard graphics user routines using NOGRA have been developed for f-k plots, power spectra, interactive trace displays, etc.

The event processor code executes broadband f-k analysis and uses velocity to report preliminary phase determination. The intention is to process detection information from one array at a time, and produce reports with velocity, azimuth, quality, polarization, frequency,

amplitude, and (preliminary) phase determination. Preliminary epicenter determination will be based upon one-array data. Improved location estimates will be based upon these reports using several arrays and Scandinavian stations when available.

Emphasis will be put on flexibility and suitability for research applications, and the work will be coordinated with the efforts on the Intelligent Array Processing System (IAS), which is scheduled for delivery to NORSAR during the summer of 1989.

IV.7 Upgrade of the ARCESS data acquisition and processing hardware

Up to June 1988, the ARCESS data acquisition system at NDPC was based on a temporary solution, using a Sun-2 computer on loan from Science Horizons. Vital hardware components of this system failed in early June, and there was a halt in the recording of ARCESS data, which lasted until the new Sun-based system (which was delivered in late June) became operational in early July. After the installation of the new system, the hardware configuration is essentially as shown in Fig. IV.7.1 in NORSAR Scientific Report No.1-87/88. Two Sun-3/280-computers handle the data acquisition and data processing tasks, and a Sun-3/260-computer is available for off-line data analysis.

J. Fyen
R. Paulsen

V. MAINTENANCE ACTIVITIES

V.1 Activities in the field and at the maintenance center

This section summarizes the maintenance activities in the field, at the maintenance center (NMC) at Hamar and NDPC activities related to monitoring and control of the NORSAR, NORESS and ARCESS arrays.

Activities related to the NORSAR array have been diverse, and most tasks concern corrective maintenance. Scanning Table V.1, we find that repair/splicing of seismic cables is prominent, but we also find repair/replacement of electronic equipment such as modems, SLEMs and LP seismometers adjustment devices (RCDs).

In addition to repair/repositioning of antennas related to the 02B telemetry stations, the NMC staff have taken care of such jobs as adjustment of Long Period seismometer parameters Free Period (FP) and Mass Position (MP).

The NDPC staff regularly monitor the subarray electronics, including communication systems. LP seismometer parameters FP and MP are remotely adjusted. SP channel parameters such as RA-5 gain, RA-5 3 dB point, filter ripple, LTA time constant, seismometer sensitivity and natural frequency are evaluated by means of special on-/offline programs.

The NORESS field system performed entirely satisfactorily throughout the reporting period, and only a few corrective actions were needed. Details are given in Table V.1.

During a visit 9-15 June to ARCESS, a new Global Positioning System (GPS) Synchronized Clock was installed by Sandia engineers in cooperation with NORSAR field personnel. During the same visit, all the fiber optical cards were modified. The modification made it possible to adjust the frequency and the phase of the clock signal for the optical data links between the HUB and the remote sites.

The KS-36000 borehole seismometer has not been operating properly due to 120 Hz oscillations in the two horizontal sensor modules. It was therefore decided to pull the seismometer from the borehole and to send it back to Teledyne Geotech for repair. This was done during the 9-15 June visit to ARCESS.

During the same visit, a cold soldering on the interface card in the Communications Interface Module (CIM) was repaired. After that repair was carried out, there has been no failure in the data link to Kjeller, which can be traced to the CIM at ARCESS.

It was found in September that the GPS unit did not operate properly. We found that the United States Naval Observatory (USNO) and Department of Defence (DOD) had changed the data content of the GPS signals being transmitted by satellites 6 and 9. This change of data contents inhibits the NAVCORE Signal Processor from acquiring these satellites. In addition, this change also inhibits the NAVCORE from acquiring any other satellite while satellite 6 and 9 are selected.

Since the USNO was in the process of changing the data content on all of the satellites, and in order to fully correct this problem, the GPS unit was sent back to Kinemetrics for a software modification that will allow the NAVCORE to decode the new data format.

In order to have a timing system at ARCESS during the period the GPS will be in the U.S. for repair, the two LF-DC Synchronized Digital Clocks were modified to work properly under marginal receiving conditions.

During the summer months, all seismometer housings of the ARCESS array were covered by moss, in order to reduce as much as possible on background seismic noise from wind and rain.

Subarray Area	Task	Date
02B (telem.)	Temporary antenna repair and repositioning	14,15,25 April
06C	Three visits to the SA in connection with testing of a SLEM which had caused timing problems before	May
NDPC	Remotely measured/adjusted LP seismometers with respect to Mass Position (MP) and Free Period (FP). Subarrays 01A, 01B, 02C, 03C and 04C	May
	02C, 03C SP channels evaluated by means of the Offline program Chanev SP. Parameters such as filter ripple, LTA time constant, RA-5 gain, RA-5 lower 3 dB point, Seismometer sensitivity, and natural frequency determined	
02B	Adjusted SP/LP gain and Offset	3 June
04C	Remote Centering Device (RCD) EW seismometer replaced	24 June
01A,01B	SP/LP gain and offset adjusted	27 June
01B	Seismic cable SP02 spliced	29 June
03C	SP/LP gain and offset adjusted	30 June
02B	Found seismic cable SP02 damaged	30 June
NORESS	Array checked together with Sandia representatives	8 June
ARCESS	NMC staff and Sandia representatives visited the array in connection with modification and timing of Fiber Optical systems. A Global Positioning System (GPS) was installed	10-15 June

Table V.1. Activities in the field and the NORSAR maintenance venter, including NDPC actitivites related to the NORSAR array, 1 April - 30 September 1988.

Subarray Area	Task	Date
NDPC	Daily check of SP and LP data, including comm. systems. LP seismometers outside specifications adjusted, Free Period (FP) and Mass Pos. (MP). SP channels 01B, 02B and 04C analyzed with respect to vital parameters by means of the Offline program Chanev SP	June
01A	Cable repair SP03	3,8,12 July
01B	Cable repair SP02	1 July
01B	Cable repair SP05	19 July
02B	Cable repair SP02	22 July
04C	Cable repair SP01	20,26,27 28 July
06C	Cable repair SP04	13,14 July
NDPC	Daily routine checks throughout the month	July
ARCESS	Replaced satellite receiver clock by the "old" receivers (HF + array)	4 August
NORESS	Satellite transmitter frequency decreased by 305 Hz. Hub preventive maintenance carried out.	19 August
	Remote sites power supply repaired	26 August
01B	Cable work SP05	3,4 August
02B	Replaced modem and SLEM Digital Unit	11,17,23, 24 August
02B	Cable work SP02	10 August
04C	The SA was visited in order to solve a special NS LP seism. problem	19 August

Table V.1. (cont.)

Subarray Area	Task	Date
NDPC	Regular check of SP/LP data and comm. systems. Weekly calibration of SP/LP seism. carried out. Adjustment of LP seismometer (MP/FP) done when outside tolerances. In August the capability of the 02B, 02C, 03C and 04C A/D converters was verified by "online" data acquisition "test 48" and the "offline" program MISNO	August
NORESS	Routine visits	September
ARCESS	On site A1 the Optical Fiber Transmitter was replaced. On D6 the Hub 61 and 70 cards were replaced. The DHL 70 card on the north-south component on C2 was replaced.	September
NORSAR	Regular check of SP/LP data and comm. systems. Weekly calibration of SP/LP seismometers. Mass Position (MP) and Free Period (FP) outside tolerances adjusted. Besides, data acquisition "test 48" and offline data analyzing program Misno run on subarray 01A.	September

Table V.1. (cont.)

V.2 Array status

No changes or modifications have been implemented since the last report.

As of 30 September 1988 the following NORSAR channels deviated from tolerances:

01A	01	8 Hz filter
	02	8 Hz filter
	04	30 dB attenuation
01B	05	bad cable

02B 08 FP not adjustable/measurable from NDPC

04C 08 FP not adjustable from NDPC

06C 05 Broadband filter installed

On the occasion of the Semipalatinsk JVE explosion on 14 September, the gain of the NORESS 3-component instrument at site C2 was reduced by 20 dB. This change was effective on 13 September at 1700 GMT, and the gain was back to normal from 16 September at 1400 GMT.

No ARCESS channels deviated from their standards during the reporting period.

O.A. Hansen
P.W. Larsen

VI. DOCUMENTATION DEVELOPED

Bungum, H. (1988): Earthquake occurrence and seismotectonics in Norway and surrounding areas. NATO Workshop Proceedings, S. Gregersen (ed.).

Kvamme, L.B. & R.A. Hansen (1988): The seismicity in the continental margin areas of northern Norway. NATO Workshop Proceedings, S. Gregersen (ed.).

Kværna, T. (1988): On exploitation of small-aperture NORESS type arrays for enhanced P-wave detectability. Accepted for publication Bull. Seism. Soc. Am.

Loughran, L.B. (ed.) (1988): Semiannual Technical Summary, 1 October 1987 - 31 March 1988, NORSAR Sci. Rep. No. 2-87/88, NORSAR, Kjeller, Norway.

Maupin, V. (1988): Surface waves in weakly anisotropic structures: On the use of ordinary or quasi-degenerate perturbation methods. Submitted to the Geophys. J.

Maupin, V. (1988): Numerical modelling of Lg wave propagation across the North Sea Central Graben. Submitted to the Geophys. J.

VII. SUMMARY OF TECHNICAL REPORTS / PAPERS PUBLISHED

VII.1 Spectral analysis of Shagan River explosions recorded at NORSAR and NORESS

As shown by Ringdal and Hokland (1987), NORSAR recordings of Lg and P coda can provide very stable estimates of the magnitudes of underground nuclear explosions at the Shagan River test site. These data thus hold considerable promise in relation to obtaining accurate yield estimates for the purpose of verifying a threshold test ban treaty.

To investigate the observational basis for estimation of magnitudes based on P-coda and Lg measurements, we have calculated power spectra from NORSAR recordings of about twenty Shagan River explosions.

The mean spectrum of the NORSAR short-period channels and the curves representing plus/minus two standard deviations are estimated for noise preceding the P-phase, for P-coda and for Lg. The time windows are equal to those applied by Ringdal and Hokland (1987) for estimating RMS based magnitudes. We will not go into detail on their procedure, but point out that the RMS of noise, P-coda and Lg were calculated from traces bandpass-filtered between 0.6 and 3.0 Hz. Fig. VII.1.1(a-c) give the spectra from the Joint Verification Experiment (JVE) explosion in the Shagan River region of September 14, 1988. The plots show the mean spectrum across NORSAR as well as curves corresponding to plus/minus two standard deviations. In the range 0.6-3.0 Hz, we find that the variations across the NORSAR array are of comparable size for both noise, P coda and Lg, and the same variation characteristics also apply to the other events investigated in this study.

A procedure to compensate for the background noise level forms part of the RMS magnitude measurements. This procedure can be simulated on the power spectra by subtracting the pre-P noise from the P-coda or Lg spectra. In Fig. VII.1.2 we illustrate the background noise compensation by showing the spectra of the noise, of Lg and of Lg minus noise.

We note that in this case the effect of the noise compensation is small in the frequency band with the maximum power (around 0.8 Hz). In fact, the noise compensation only becomes important for the lower magnitude events. In the following, references will be made to noise-corrected Lg spectra only.

Note that the Lg spectrum of Fig. VII.1.2 exhibits a peak between 0.7 and 0.8 Hz. From the NORSAR short-period response given in Fig. VII.1.3, we can see that in the frequency range 0.6 to 3.0 Hz the amplification is varying by a factor of ten. If the dominant frequency of the Lg phase were to vary significantly from event to event, the RMS-based magnitude estimates could be influenced by the varying amplification. To investigate this problem further, Fig. VII.1.4a shows expanded Lg spectra of eleven events from the southwestern part of the Shagan River test region. The RMS Lg magnitudes range from 5.67 to 6.19. Although there is a trend of lower dominant frequencies for the highest peaks, the actual variation is small. In Fig. VII.1.4b we show similar spectra for seven events from the northeastern part of the Shagan River test region. The RMS Lg magnitudes for these events vary from 5.87 to 6.11.

Ringdal and Hokland (1987) found in their study of Lg and P-coda magnitudes from the Shagan River test site that there was a significant regional anomaly within that site. In the northeastern part, the P-coda and ISC magnitudes were consistently low compared to Lg, whereas in the southwestern part they were consistently high. To investigate whether this anomaly is reflected in the Lg spectra, we have plotted in Fig. VII.1.5 the peak frequencies for the events investigated as a function of RMS Lg magnitude, with different symbol types for the two subregions. Although there are a couple of outliers, both the events from the NE part (crosses) and the SE part (filled rectangles) follow the same trend of lower dominant frequencies for higher magnitudes. From the results given in Fig. VII.1.5 we can infer that the Lg peak frequency characteristics do not differ significantly from the NE to the SW part of the Shagan River test site. The overall variation of the dominant frequency among the events of different

magnitude is less than 0.15 Hz. We therefore find that amplification differences, see Fig. VII.1.3, will not influence the variation of the magnitude estimates significantly.

In Fig. VII.1.6a and VII.1.6b we have calculated P-coda and Lg spectra for two Shagan River events with comparable RMS Lg magnitudes. The event represented in Fig. VII.1.6a is located in the SW region and has an RMS Lg magnitude of 5.96, whereas the event given in Fig. VII.1.6b is located in the NE region and has a magnitude of 5.87. The feature we want to emphasize from these figures is that the P-coda spectrum of the SW event is well above that from the NE event in the entire frequency range 0.6 to 3.0 Hz. On the other hand, the differences in the Lg spectra are small and are confined to the frequency range 0.6 to 1.0 Hz.

For events below a certain magnitude, the SNR of Lg at NORSAR is too low for application of Lg-based magnitude measurements. In theory, the SNR could be improved through beamforming, but in practice the Lg phase has too low coherency across NORSAR for this to be meaningful. On the other hand, the NORESS array has shown an excellent capability of improving the SNR. In Fig. VII.1.7a we show the mean NORESS spectra for noise preceding the P-phase and for Lg. The event considered is the JVE explosion of September 14, 1988. At 0.8 Hz, the SNR is about 11 decibels. By forming a beam from the center instrument and the D-ring of the NORESS array with steering delays corresponding to an apparent velocity of 4.3 km/s and the azimuth to the Shagan River test site (80 degrees), the SNR can be significantly improved. In Fig. VII.1.7b, we show the beam spectra of noise and Lg and find and SNR of 17 decibels at 0.8 Hz, implying that NORESS Lg measurements of Shagan River explosions may be done for event of 6 dB (0.3 m_b units) lower than for NORSAR. However, in the low-SNR cases where we have to apply the beamforming technique on NORESS array recordings to obtain an Lg magnitude estimate, the variance in the estimate will be larger than for the high SNR cases where we can average over the full NORSAR array.

To illustrate how NORESS beamforming works for the Lg phase, we have applied the wide-band slowness estimation techinque to NORESS short-period recordings of a 16 min long wavetrain comprising all phases from the JVE explosion. The center instrument and the C- and D-rings were analyzed in the frequency band 0.6 to 3.0 Hz. Each time window was three seconds long and the separation between the windows was one second. The results are given in Fig. VII.1.8 and show the following: In the upper panel, the intermediate period vertical channel, bandpass filtered between 0.6 and 3.0 Hz is displayed. In order to more clearly visualize the PP phase, occurring after about 120 seconds and the Lg phase arriving between 750 and 870 seconds, we have clipped the amplitude of the P-phase in the plot. In the second panel, the azimuth from the slowness analysis is given. The size of the rings represent a coherency measure of the slowness solution. Although there is a relatively large scatter in azimuth around the theoretical value of about 80 degrees, the time intervals around P, the early P-coda, PP and Lg show a more uniform pattern than the rest. The slowness or apparent velocity estimates, given in the lower panel, show that between P and PP the apparent velocity is consistently above 10 km/s. It then drops to below 5 km/s after about 6 minutes, and then stays at about this level throughout the wavetrain. The relatively consistent azimuth and apparent velocity estimates within the Lg wavetrain explain why the beamforming works well for this phase.

Conclusions

In this study we have presented some results illustrating some of the features related to magnitude estimation based on RMS Lg and RMS P-coda measurements. The Lg spectra from both the NE and the SW part of the Shagan River region show little variation in spectral shape and dominant frequency. Even though the RMS Lg magnitudes are computed from traces filtered in the 0.6-3.0 Hz band, the spectra show that the signal energy level between 0.6 and 1.0 Hz essentially determines the Lg magnitudes.

For events from SW Shagan, the spectral difference between P-coda and Lg is larger than for events from the NE part. This applies to the entire frequency range 0.6 to 3.0 Hz . It also follows that the spectral level of the entire frequency band analyzed (0.6 to 3.0 Hz) contributes to the RMS P-coda magnitude estimates.

In cases where the single station SNR of the Lg is too low for Lg magnitude estimation, we can employ the beamforming capability of the NORESS array to improve the SNR. About 6 decibels SNR improvement can be achieved, i.e., about 0.3 magnitude units. The applicability of beamforming of the Lg phases has been demonstated by running moving time window slowness analysis on a 16 minutes long window covering all phases from a Shagan River nuclear explosion.

T. Kværna
F. Ringdal

References

Ringdal, F. and B.Kr. Hokland (1987): Magnitudes of Semipalatinsk explosions using P coda and Lg measurements at NORSAR. Semiannual Technical Summary 1 April - 30 September 1987, No.1-87/88.

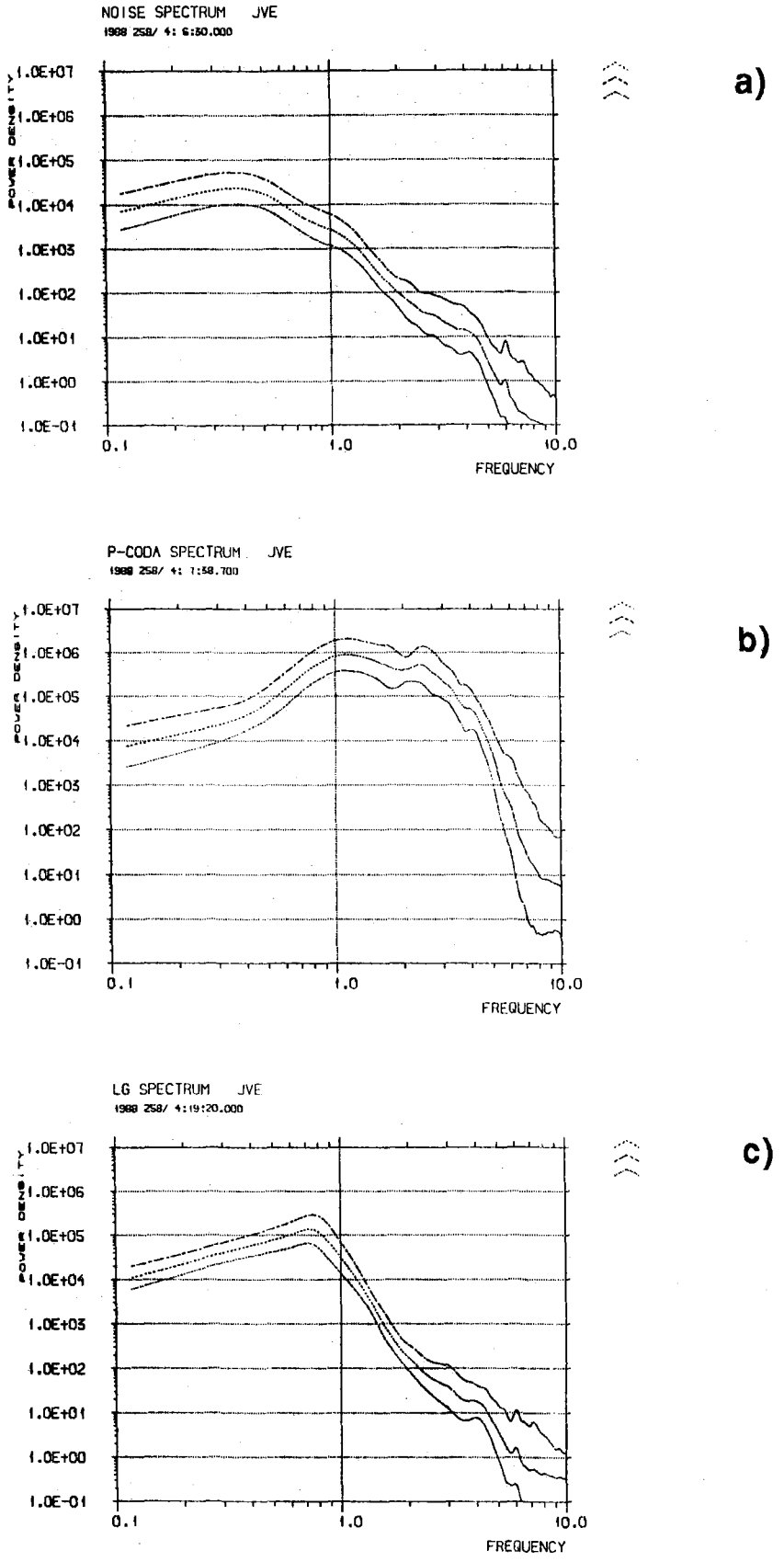

Fig. VII.1.1. Mean uncorrected NORSAR power spectra of noise preceding the P-phase (a), P-coda (b) and Lg (c). The upper and lower curves indicate plus/minus two standard deviations. The event analyzed is the Joint Verification Experiment (JVE) explosion at the Shagan River test site on September 14, 1988.

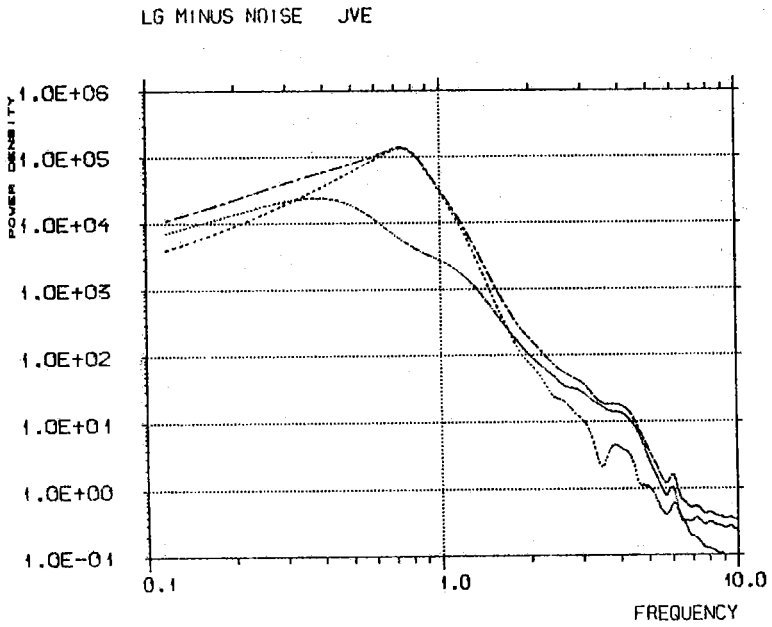

Fig. VII.1.2. The noise compensation procedure is illustrated in this figure. The upper spectrum represents the Lg phase from the JVE, the lower spectrum represents noise preceding the P-phase and the difference is given in the middle. Note that the frequency range around the spectral peak of Lg is marginally influenced by the noise compensation.

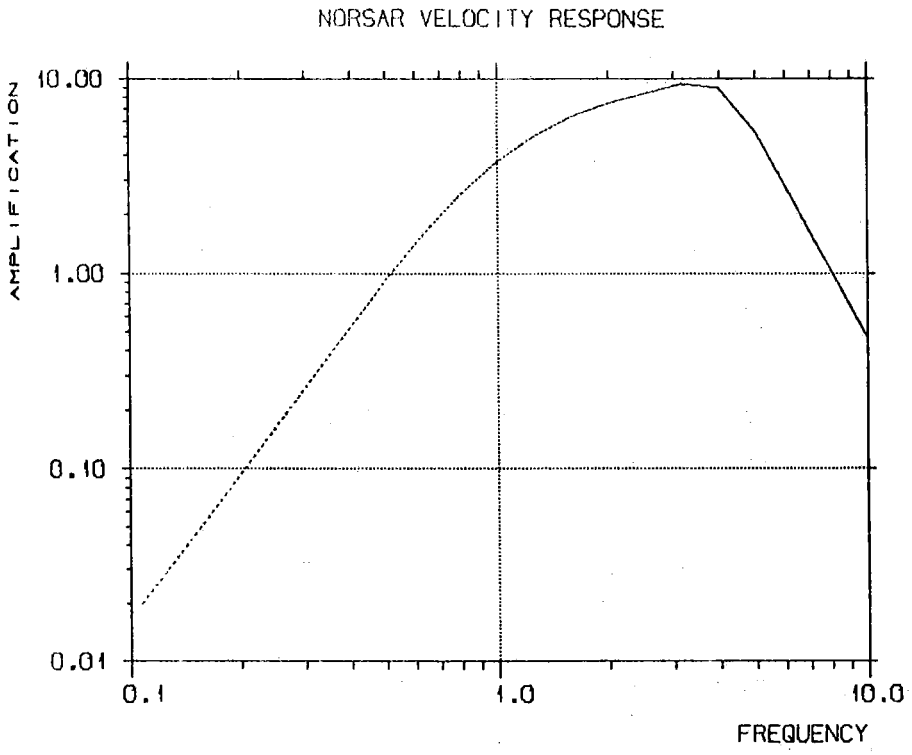

Fig. VII.1.3. NORSAR short-period velocity response function.

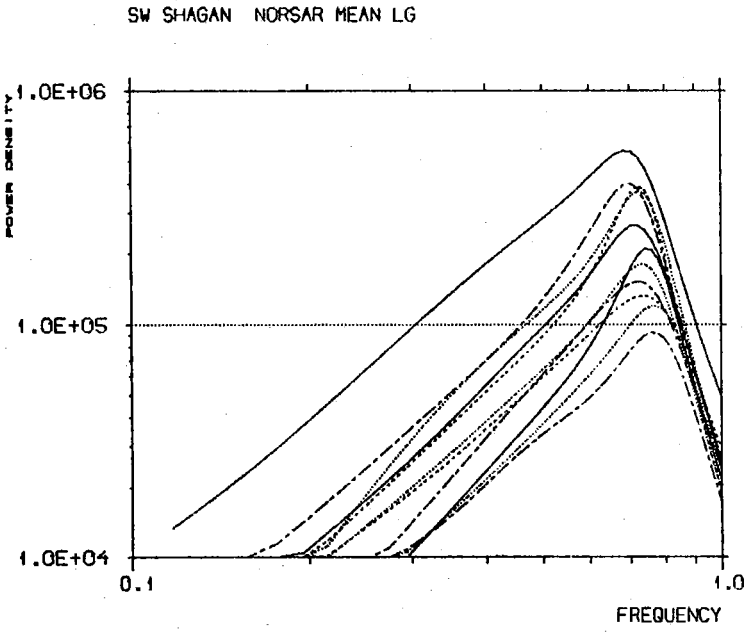

Fig. VII.1.4a Expanded plot of Lg spectra calculated from NORSAR recordings of eleven explosions from the southwestern part of the Shagan river test site.

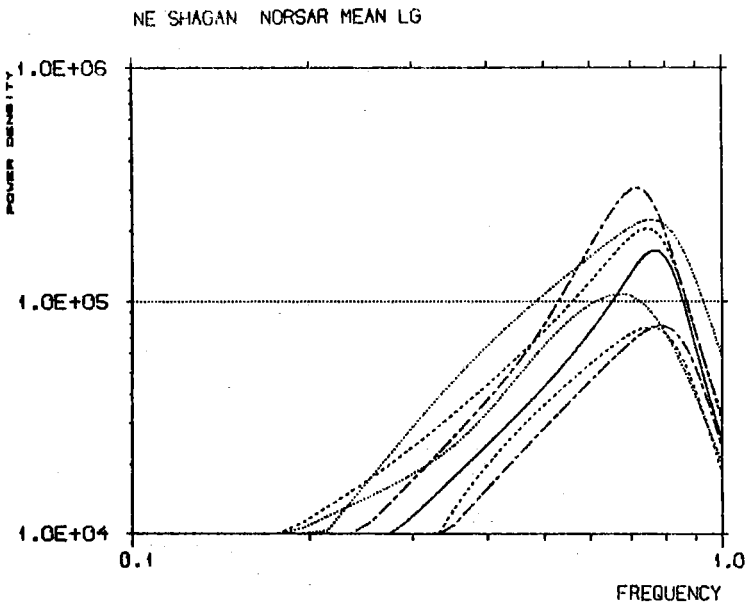

Fig. VII.1.4b. Expanded plot of Lg spectra calculated from NORSAR recordings of seven explosions from the northeastern part of the Shagan river test site.

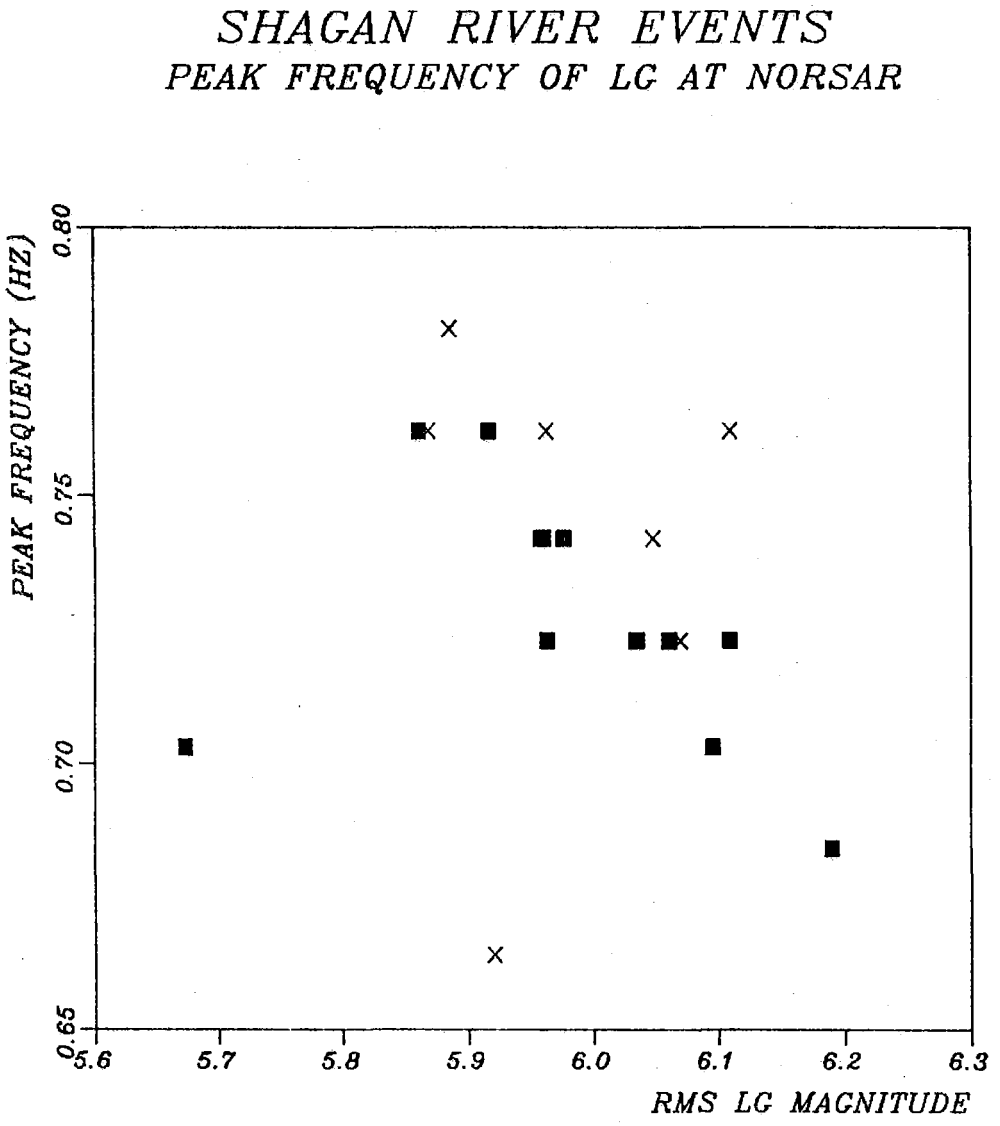

Fig. VII.1.5. Peak frequency versus RMS Lg magnitude for the events given in Fig. VII.1.4a and 4b. Crosses represent events from the NE part of the Shagan River test site, whereas filled rectangles represent events from the SW part.

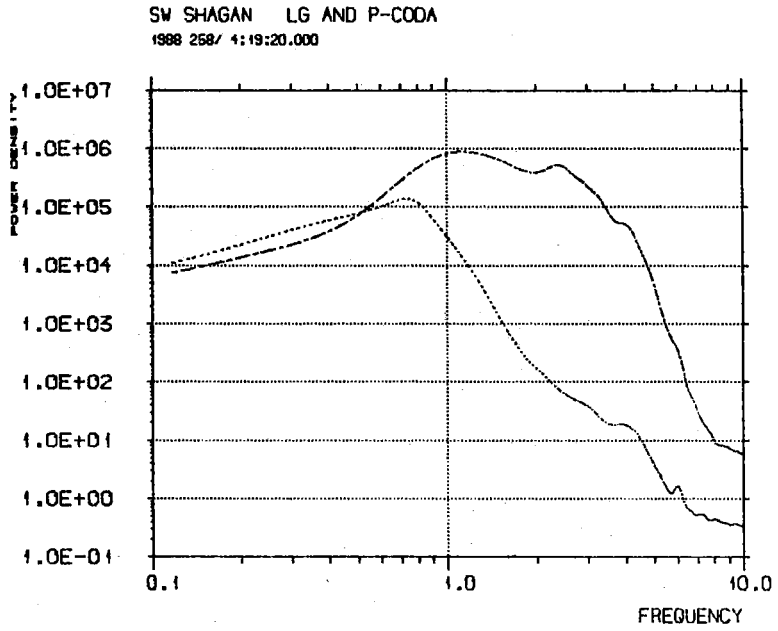

Fig. VII.1.6a. P-coda and Lg spectra from the JVE explosion of September 14, 1988. This event is located in the SW part of the Shagan River test site. The RMS Lg magnitude is estimated at 5.96.

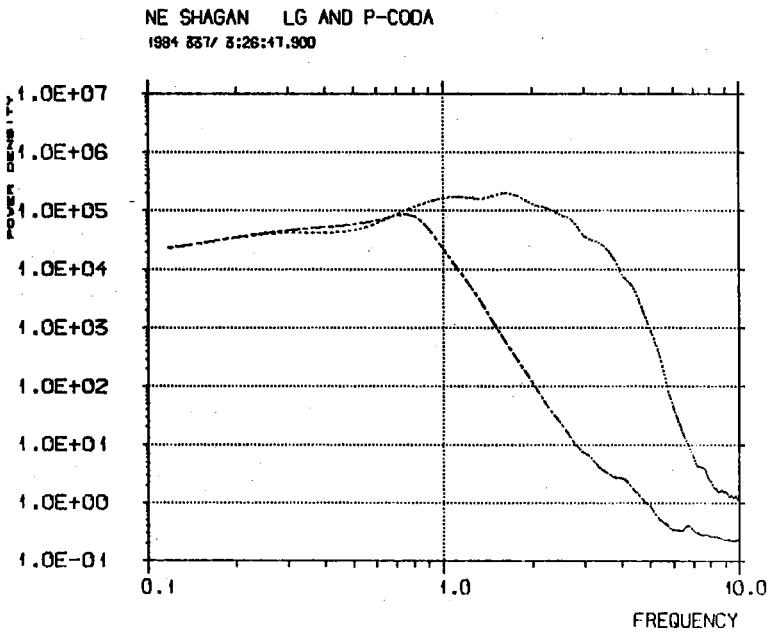

Fig. VII.1.6b. P-coda and Lg spectra from an event of 12 December 1984. This event is located in the NE part of the Shagan River test site and the RMS Lg magnitude is estimated at 5.87.

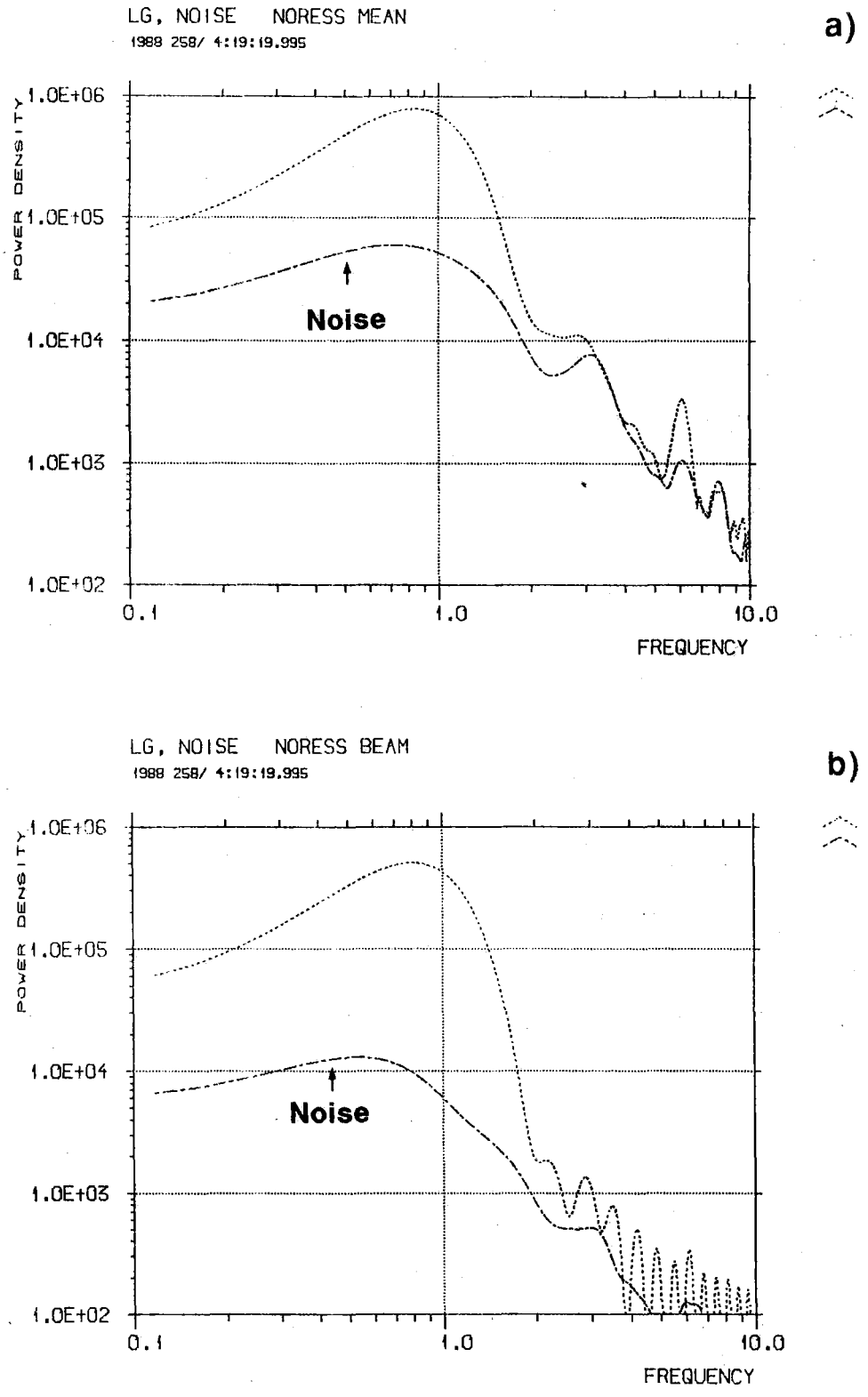

Fig. VII.1.7. Illustration of SNR gain for Lg by beamforming using NORESS data from the JVE explosion. Panel a) shows uncorrected NORESS power spectra for Lg and noise averaged over all individual seismometers. Panel b) is based on a beam formed from the center instrument and the D-ring, using steering delays typical of Lg phases from Semipalatinsk (phase velocity 4.3 km/s, azimuth 80 deg). Note the considerably greater SNR for the NORESS beam.

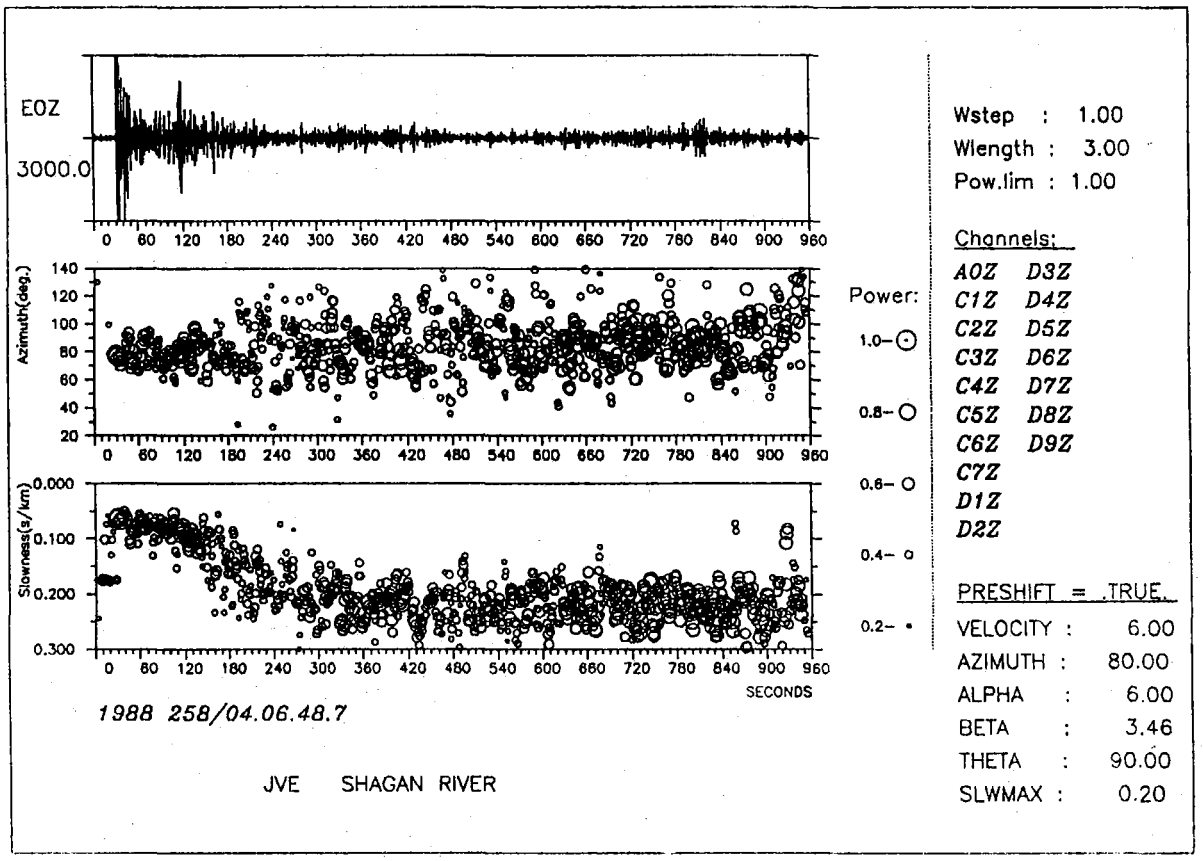

Fig. VII.1.8. Results from slowness analysis of NORESS recordings of the JVE explosion. The upper panel shows the intermediate period vertical component bandpass filtered between 0.6 and 3.0 Hz. The middle panel gives the azimuth solutions and the lower panel the absolute slowness (inverse of apparent velocity) solutions. The size of the circles represents a coherency measure of the individual estimates.

VII.2 Statistics of ISC travel time residuals

The location of seismic events by a network of stations requires that adequate theoretical travel times are available, either by interpolation in tables, or by calculating the times in a reference velocity model. Despite obvious shortcomings the Jeffreys-Bullen tables are still in use at the major seismological centers for locating events. The more recent PREM model (Dziewonski and Anderson, 1981) is more satisfying in that it was constructed to fit a large seismological data set including free oscillation eigenfrequencies, but the original transversely isotropic model is not well suited for routine travel time calculations, and the isotropic version of PREM has not been adequately tested against arrival time observations. Here we report on the statistics of teleseismic travel time residuals with respect to the isotropic PREM.

We have extracted P arrival time data from the ISC bulletins for the year 1984, PcP and PKP for the years 1975-1984, and PKKP for the years 1964-1984. Additional PKKP and PnKP, $n > 2$, were taken from bulletins of the original LASA and NORSAR arrays, and from special publications. All data were subjected to a standard processing sequence, similar to that of others: Residuals were computed relative to PREM, subjected to station corrections, corrected for ellipticity and lower mantle variations, and corrected for the effects of source structure and/or mislocation. Data belonging to a particular branch were finally averaged to form 'summary ray' data, based on pairs of approximately equal area blocks (equalling 10×10^{o} at the equator). For details of the data selection and processing we refer to Doornbos and Hilton (1988). The number of 'summary ray' data finally obtained were 5415 for P, 1668 for PcP, 1395 for PKP (13C), 871 for PKP (AB), 686 for PKKP (13C), and 189 for PnKP (AB).

Typical examples of histograms of summary residual data are shown in Fig. VII.2.1. In this figure we have also plotted the data from deep events. A comparison suggests that reading errors are significant especially for arrivals from shallow events; note that the number of

late readings is reduced in the data from deep events. For the core phases and for P at distances larger than 85° (P2), the early parts of the histograms for all data and for the data from deep events overlay quite well. This means that the upper mantle model of PREM is consistent with the ISC depth estimates. The P data at distances smaller than 85° (P1) are different in that there are anomalously many early arrivals from shallow events; this may also explain the relatively large variance of these data. It is possible that one begins to see here the effect of subduction zones, since many of the events occur within these zones.

Fig. VII.2.1 also shows that there is a significant mean residual left in the data. This is especially clear for the core phases, and we can infer their relation. If the sampling by summary rays is reasonably uniform and if nonlinear effects can be neglected, then for any particular phase the mean residual represents the effects of differences between PREM and the spherically averaged earth, and/or systematic reading errors. The PcP, PKP and PnKP mean residuals for summary rays in the same ray parameter interval are expected to follow a linear trend:

$$\overline{\delta T}(\mathrm{PnKP}) = \overline{\delta T}_m + n\overline{\delta T}_c, \qquad n = 1,2,\ldots \tag{1}$$

where $\overline{\delta T}_m \equiv \overline{\delta T}(\mathrm{PcP})$, and $\overline{\delta T}_c$ represents the residual after one passage of the wave through the core; both the velocity structure and the core-mantle boundary level may contribute to the residual. A relation of the form (1) can be discerned for the phases with ray parameters above 4 s/d, but surprisingly, PcP, PKP and PKKP in the ray parameter range 2-3 s/d do not follow a linear trend. One possible explanation, now under investigation, is based on the fact that PcP at small distances is weak, and known to be often unobservable. It is therefore possible that PcP (and possibly PKKP) is observed primarily in circumstances of relatively strong focusing, with an accompanying phase delay.

It is also of interest to note that the variance of the PKKP data is not much larger than that of PKP in the same ray parameter range (2-3 s/d). It is convenient to plot the variance of the various phases as a function of their sensitivity to variations of deep earth structure. Here we give such a relation between the variance of the data σ_T^2 and the variance of core-mantle boundary topography σ_r^2. For PcP:

$$\sigma_T^2 = \sigma_o^2 + \frac{4}{r^2} (\eta^{+2} - p^2)\, \sigma_r^2 \qquad (2a)$$

and for PnKP if the perturbations δr in the sampling points r_i are uncorrelated:

$$\sigma_T^2 = \sigma_o^2 + \frac{2}{r^2} [\{(\eta^{-2} - p^2) - (\eta^{+2} - p^2)^{1/2}\}^{1/2} + 2 \sum_{i=2}^{n} (\eta^{-2} - p^2)]\sigma_r^2 \qquad (2b)$$

Here $\eta = r/v$, and a superscript $^{+}/^{-}$ refers to the top/bottomside of the boundary. In Fig. VII.2.3 the variance of the data subsets is plotted following equation (2). One inference from this figure is that the PKKP data imply a relatively smooth core-mantle boundary on a large scale; for illustrative purposes the expected travel time variance for $\sigma_r^2 = 1\ km^2$ is shown in Fig. VII.2.3. Another inference is that models of large-scale lateral variation of deep earth structure can explain only a relatively small part of the data variance.

D.J. Doornbos
T. Hilton

References

Doornbos, D.J. and T. Hilton (1988): Models of the core-mantle boundary and the travel times of internally reflected core phases, submitted for publication.

Dziewonski, A.M. and D.L. Anderson (1981): Preliminary Reference Earth Model (PREM). Phys. Earth Planet. Inter., 25, 297-356.

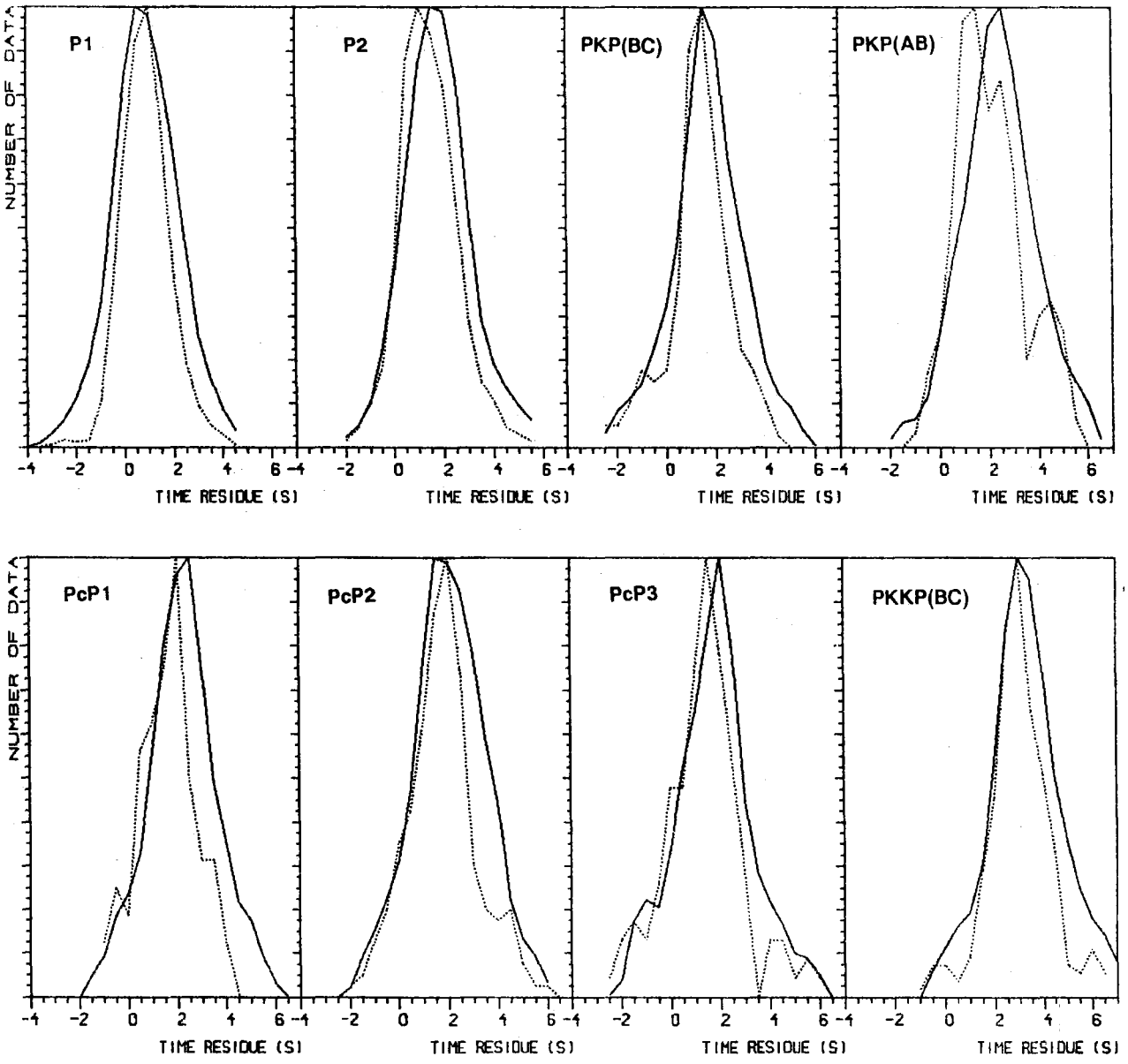

Fig. VII.2.1. Histograms of travel time residuals of 'summary ray' data. Ray parameter ranges are 2-3 s/d for the BC branches of PKP and PKKP and for PcP1, 3.5-4 s/d for PcP2 and >4 s/d for the AB branches of PKP and PnKP and for PcP3. Distance interval for P1 is 65-85°, for P2 85-95°. ——— : all data; ----- : data from deep events (>400 km depth).

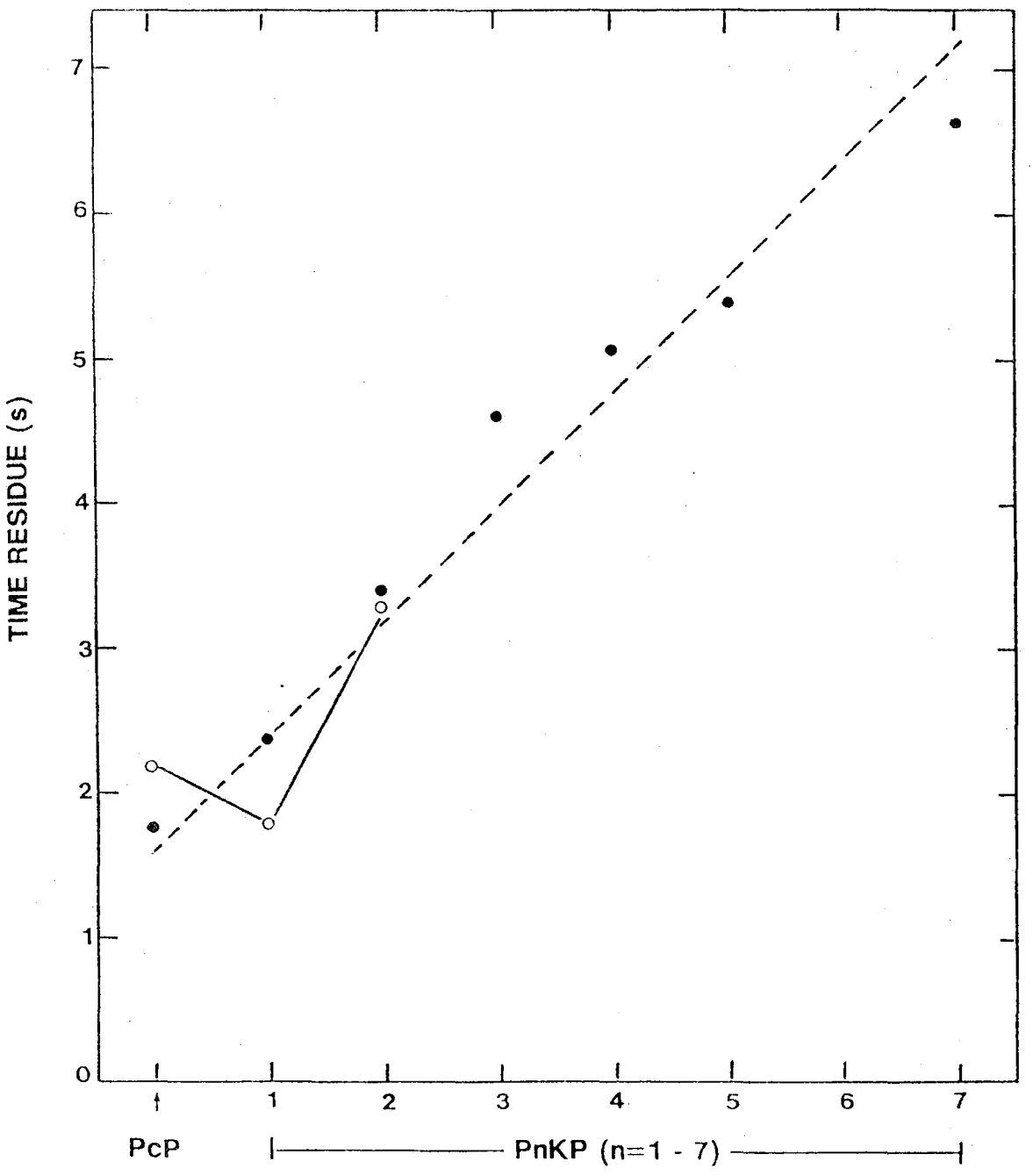

Fig. VII.2.2. Mean 'summary ray' travel time residuals of PcP and PnKP, $n \geq 2$. o: $2 \leq p \leq 3$ s/d; ●: $p > 4$ s/d. The dotted line is a linear fit to the data with $p > 4$ s/d.

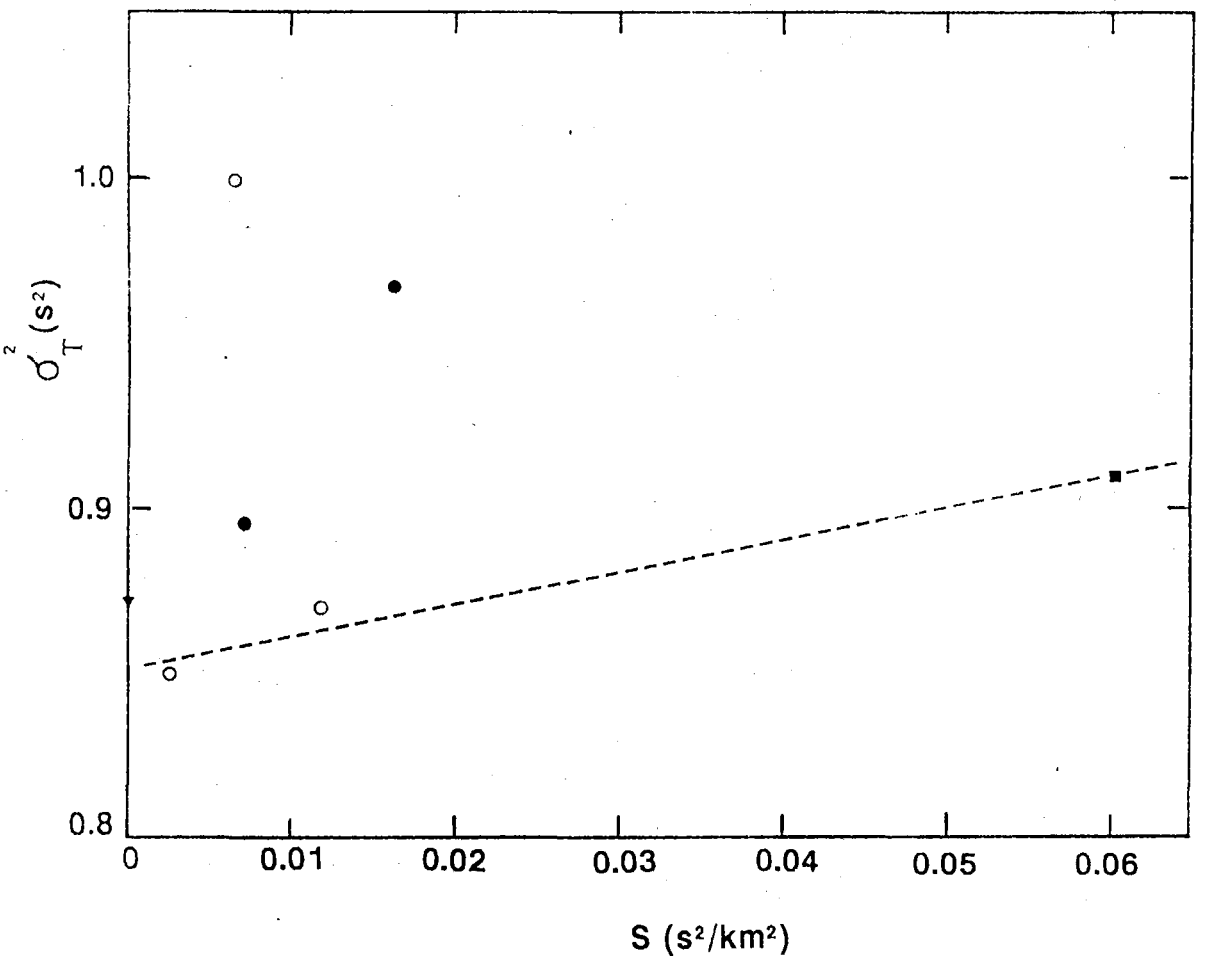

Fig. VII.2.3. Variance σ_T^2 of 'summary ray' travel time residuals, as a function of sensitivity S to boundary topography: $\sigma_T^2 = \sigma_o^2 + S\sigma_r^2$ where σ_r^2 is variance of boundary topography. Data subsets of PcP(o), PKP(●), PKKP(■) and P(▼). The dotted line has a slope $\sigma_r^2 = 1$ km^2.

VII.3 Modelling of Lg-wave propagation across the Central Graben of the North Sea

This is the third and final report on modelling of Lg wave propagation in the Central Graben of the North Sea in an attempt to explain the very strong attenuation of the Lg wavetrain observed in this area. In the first report (Maupin, 1987), we presented the modelling method and some preliminary tests. The bulk of the modelling results, i.e., the reflection and transmission matrices for Rayleigh and Love type Lg-modes propagating at a right angle or at an oblique angle across a graben model, were presented in the second report (Maupin, 1988). A first interpretation of the matrices showed that on the average over many Lg wavetrains, 80% of the incoming Lg energy remains in the Lg wave after propagation across the graben model.

The transmission matrix affects differently incoming Lg wavetrains with different modal contents. The relative amplitudes of the different modes, which depend on their excitation by the seismic source, as well as their phase differences when reaching the Graben, which vary with epicentral distance, define the modal content. In order to exploit more completely the transmission matrix, we analyze here its effect on Lg wavetrains from different sources at different distances from the Graben. Since the transmission of Rayleigh and Love waves at a right angle or at an oblique angle across the model have been found very similar in the second report, we concentrate our analysis here to Rayleigh waves propagating at right angles across the structure. On the other hand, the transmission across three variants of the Central Graben model used in the previous reports (and now called model 1) are also examined, to account for possible block-faulting of the Graben margin (models 2 and 3, Fig. VII.3.1) or roughness of the sediment-basement interface (model 4, Fig. VII.3.1). We also examine the phase stability with period of the transmitted wavetrain.

After inspection of the results for different sources, we retain three typical cases for discussion: an explosion, a strike-slip earthquake with a fault trace at 75^{o} from the symmetry direction of the Graben,

and an earthquake which occurred on the western flank of the Viking Graben on 29 July 1982 (strike: 100°, dip: 63°, slip: -170°, after Havskov and Bungum, 1987), for which we study the waves travelling due east perpendicularly across the Viking Graben and to Norway. We use explosions with 4 different focal depths, ranging from 0 to 3 km, and earthquakes at 7 different focal depths sampling the whole crust. The distances of the events from the Graben are taken ranging from 0 to 1000 km, with a step of 10 km, providing a good sampling of possible phase shifts between the different modes when reaching the Graben. These events do not intend to model a complete or realistic situation, but to provide an oversight of the effect of the Graben on different Lg wavetrains. We recall that Gregersen (1984) used many earthquakes in his study of the attenuation across the North Sea Central Graben, and pointed out that the effect does not depend on the source.

The total energy transmission

For each source type, depth and distance, we calculate the amount of total energy contained in the Lg wavetrain before and after propagation across the Graben. This total energy includes the energy contained in the whole crust for the 11 Lg modes. For each source mechanism and depth, the results are summarized in a histogram of the transmission ratios, which illustrates how their values vary for different source-graben distances.

One of these histograms is shown on Fig. VII.3.2. It displays the values of the transmission ratios across model 1 for an Lg wavetrain excited by a Viking Graben earthquake at 15 km focal depth. The distribution is well peaked around transmission ratios of 80%. Histograms for other focal depths, source mechanisms or models are very similar in shape, with a slight shift of -10% for explosions close to the surface. Fig. VII.3.3, where incident and mean transmitted energies are plotted as a function of source type and depth, also testifies that in the large majority of cases, 80% of the incident energy is transmitted as an Lg wave across our models of the Central Graben. The remaining 20% is converted to Sn or other S waves propagating in the mantle.

This result is in agreement with the findings in report no. 2, and shows that the total energy transmission ratio is only slightly dependent on the source mechanism which has excited the Lg wavetrain.

The surface energy transmission

Since surface waves have their energy distributed with depth differently from one mode to the other, their total energy does not directly indicate how much of the energy is confined close to the surface, or equivalently the surface displacement. More in agreement with what can actually be measured, we therefore also analyze the ratios of transmitted over incident surface energy. This surface energy is the energy of the whole Lg wavetrain measured on the vertical component of a seismometer. The ratios of transmitted over incident maximum vertical displacement at the surface were also calculated, but are not discussed here since the more global character of the energy makes it *a priori* a more stable quantity for estimating the attenuation. We do, however, observe a high degree of similarity between the ratios in energy and in maximum displacement.

The pattern of surface energy transmission is very different from the pattern of total energy transmission. Three typical histograms of surface energy transmission ratios for different source-graben distances are displayed on Fig. VII.3.4, and incident and mean transmitted surface energies as a function of source depth are plotted in Fig. VII.3.5 and VII.3.6 for different sources. In order to indicate the dispersion in the transmission due to changes in the models, we plot the maximum and minimum values of the mean transmitted energies calculated with models 1 to 4. No rule applies as to which model usually gives the lower or higher value.

Fig. VII.3.4a is a typical histogram for explosions or very shallow earthquakes, for which the surface transmission ratios are smaller than the total energy transmission ratios. For these sources, a large part of the total Lg energy is confined close to the surface of the model, mainly in the sedimentary layer, before reaching the Graben. Crossing

the Graben shifts part of the energy deeper in the crust by redistributing the energy more evenly among the different Lg modes. This effect amplifies at the surface the global loss of Lg energy. The surface signature of the Lg wave is therefore decreased by a factor of 0.6 to 0.75 in terms of mean amplitude of the signal.

Some earthquakes with certain focal mechanisms or located at the bottom of the crust excite more evenly the different modes of the Lg waves. This is the case for mid-crustal or deep strike-slip earthquakes, for example, which have rather well-peaked transmission ratio distributions (Fig. VII.3.4b), similar to those for the total energy, and mean values of surface energy transmission around 80% (Fig. VII.3.5). In that case, the mean surface displacement is decreased by a factor of 0.9 after crossing the Graben, and this directly accounts for the total loss of energy in the Lg wavetrain.

Other types of mid-crustal earthquakes, like the mid-crustal Viking Graben earthquake, excite primarily the Lg modes having their energy confined in the middle of the crust. The surface energy before reaching the Graben is thus small compared to the total energy involved in the Lg wavetrain. By crossing the Graben, the energy is redistributed among the modes, and some energy is thereby shifted from the middle of the crust towards the sedimentary layer and the surface. The net effect is an increase in surface energy (Figs. VII.3.4c and VII.3.5), despite the decrease of total energy. In that case, an increase of 1.4 can be expected for the mean amplitude of the recorded Lg wavetrain.

The total energy transmission ratios have shown that the Moho remains a rather energy-proof barrier (only 20% of the energy leaks into the mantle). On the other hand, the surface energy ratios show that the crustal thinning of the Central Graben causes important transfers of energy among the different units of the crust. Comparing the surface energy curves (Figs. VII.3.5 and VII.3.6) with the total energy ones (Fig. VII.3.3), we see that the surface energy curves are very different from the total energy ones before propagation across the Graben (filled symbols), but much more similar afterwards (open

symbols). The Graben has redistributed more evenly within the crust the total energy involved in the Lg wavetrain, and the surface energy reflects better the total amount of energy contained in the whole crust.

Propagation across our Graben models leads to some Lg amplitude variations at the surface, though limited in size and both positive and negative. They are very different from the factor 0.25 to 0.5 actually observed in the North Sea Graben area. Moreover, the preferred focal depth of seismic events in the North Sea is very often around 15 km (Havskov and Bungum, 1987), which would bias our transmission ratios towards their highest values. Our modelling would at the most explain a factor of 2 between the attenuation of Lg waves produced by explosions and Lg waves produced by earthquakes, but can in no case explain the general and strong attenuation observed in this area.

Coherency of the phase with period

The previous calculations have been made at a single frequency. The phase behavior of the waves as a function of period is a key element to the effective build-up of a wavetrain. If rapid variations are observed, interferences between neighboring periods might destroy the wavetrain. In order to check the stability of the phase as a function of period, we now compare the phases of the Lg wave modes propagating out of the Central Graben at 2 neighboring periods, 1.0 and 1.02 s.

We calculate the transmission matrices at the 2 periods. For the same series of sources and source-graben distances as earlier in this report, we calculate the phase of each Lg mode propagating out of the Graben at the 2 periods. We must note that a mode propagating out of the Graben originates from the combination in the Graben of different modes initially excited by the source. Its phase thus depends in a complicated way on the phases of these modes when they enter the structure. We subtract from the total phase the pure propagation phase, i.e., the integral over horizontal distance of the mode local phase slowness. By using a phase free of pure propagation effect, the phase difference between the modes at the 2 different periods is actually

measured at the arrival time of the mode predicted by its group velocity.

On Fig. VII.3.7 are displayed three histograms of the phase differences for the different modes and different source-graben distances after propagation across model 1. Due to the unknown but certainly poor accuracy of the transmission matrix phase, which is influenced by the zoning of the model, we cannot use these histograms very quantitatively. Even if in the second one large phase differences occur rather frequently, cases a) and c) testify that the phases of the modes are not systematically random after crossing the Graben, and therefore cannot give rise to a generally strong attenuation of the wavetrain by destructive interference.

Conclusion

The investigations presented in this report confirm the conlusions already drawn in the second report.

Our numerical modelling of Lg wave propagation in a simplified model of the North Sea Central Graben does not predict the severe attenuation of the wavetrain actually observed in this region. On the contrary, the Lg wavetrain appears very robust when crossing a zone where its waveguide is strongly deformed.

Since the large-scale geometry of the Graben fails to explain the observed data, we suggest that future work explore alternative explanations for the observed attenuation. Scattering by 2D or 3D basaltic intrusions in the lower crust, extensive faulting associated with intra-fault weak material, or more rheological aspects might be good candidates.

V. Maupin, Postdoctorate Fellow

References

Gregersen, S. (1984): Lg-wave propagation and crustal structure differences near Denmark and the North Sea. Geophys. J.R. astr. Soc., 79, 217-234.

Havskov, J. and H. Bungum (1987): Source parameters for earthquakes in the Northern North Sea. Norsk Geol. Tidsskr., 67, 51-58.

Maupin, V. (1987): Preliminary tests for surface waves in 2-D structures. NORSAR Semiann. Tech. Summ. 1 Apr - 30 Sep 1987, NORSAR, Kjeller, Norway.

Maupin, V. (1988): Coupling of short period surface wavetrains across the North Sea Graben, NORSAR Semiann. Tech. Summ. 1 Oct 1987 - 31 Mar 1988, NORSAR, Kjeller, Norway.

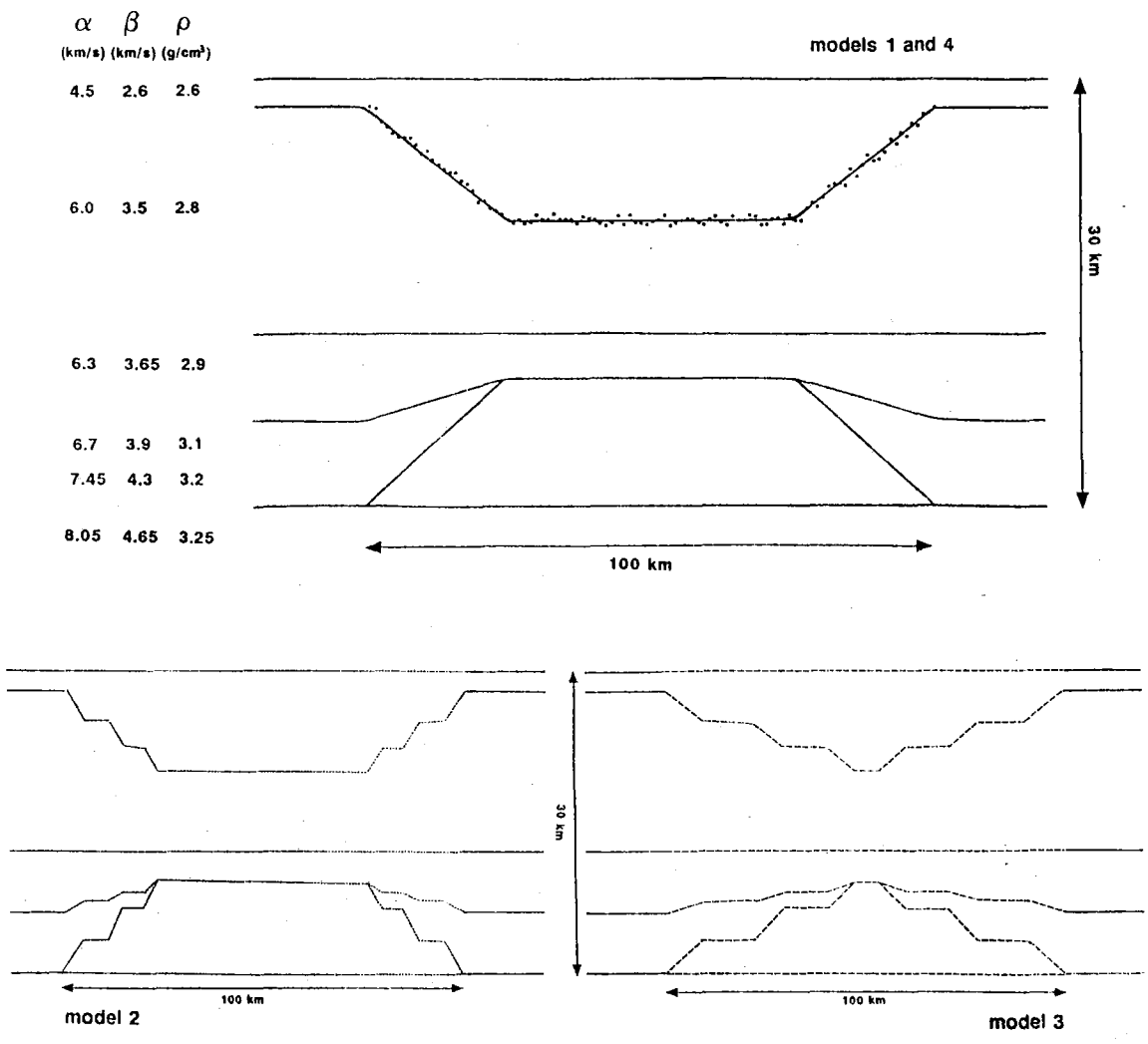

Fig. VII.3.1. Models of the North Sea Central Graben.

Model 1: Full line model, used in the previous reports
Models 2 and 3: Block-faulted models
Model 4: The same as Model 1 with perturbations of the sediment-basement interface represented by a dotted line.

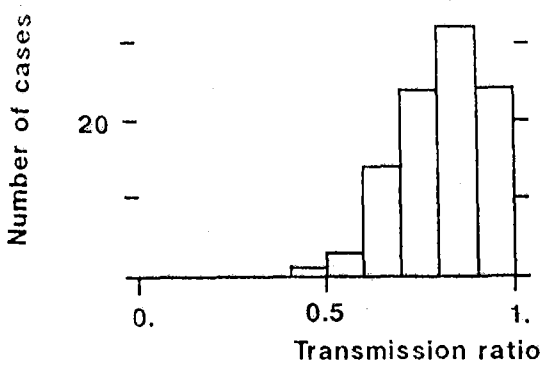

Fig. VII.3.2. Histogram of the energy transmission ratios for a Viking Graben-type event at 15 km focal depth and distances from the Graben ranging from 0 to 1000 km.

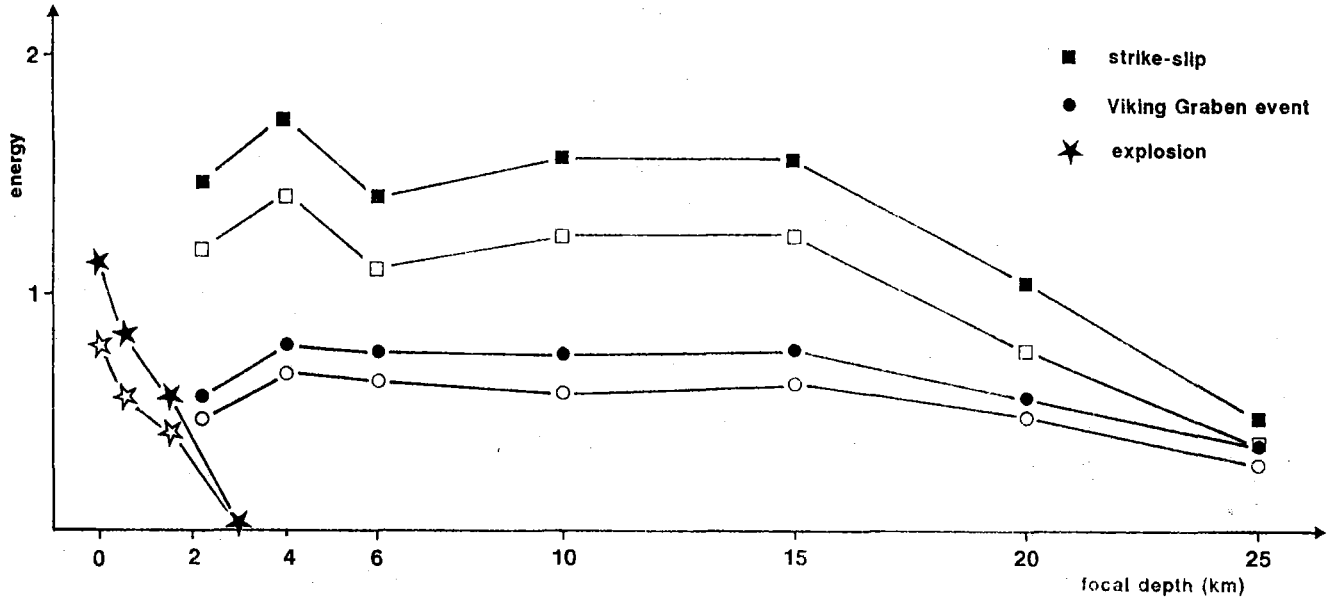

Fig. VII.3.3. Total energy in the Lg wave before (filled symbol) and after propagation across model 1 (open symbol), as a function of source type and depth. The energy scale is only relative since no physical source size is included in the modelling.

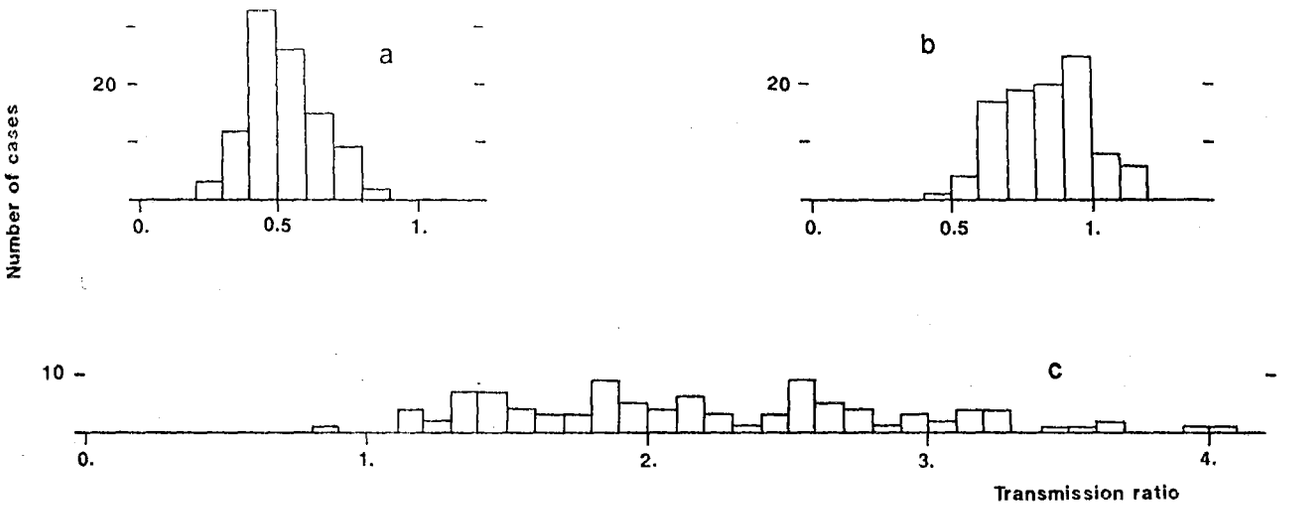

Fig. VII.3.4. Histogram of surface energy transmission ratios for: a) an explosion at the surface; b) a strike-slip event at 15 km focal depth; and c) a Viking Graben-type event at 15 km focal depth and, for all cases, distances from the Graben ranging from 0 to 1000 km.

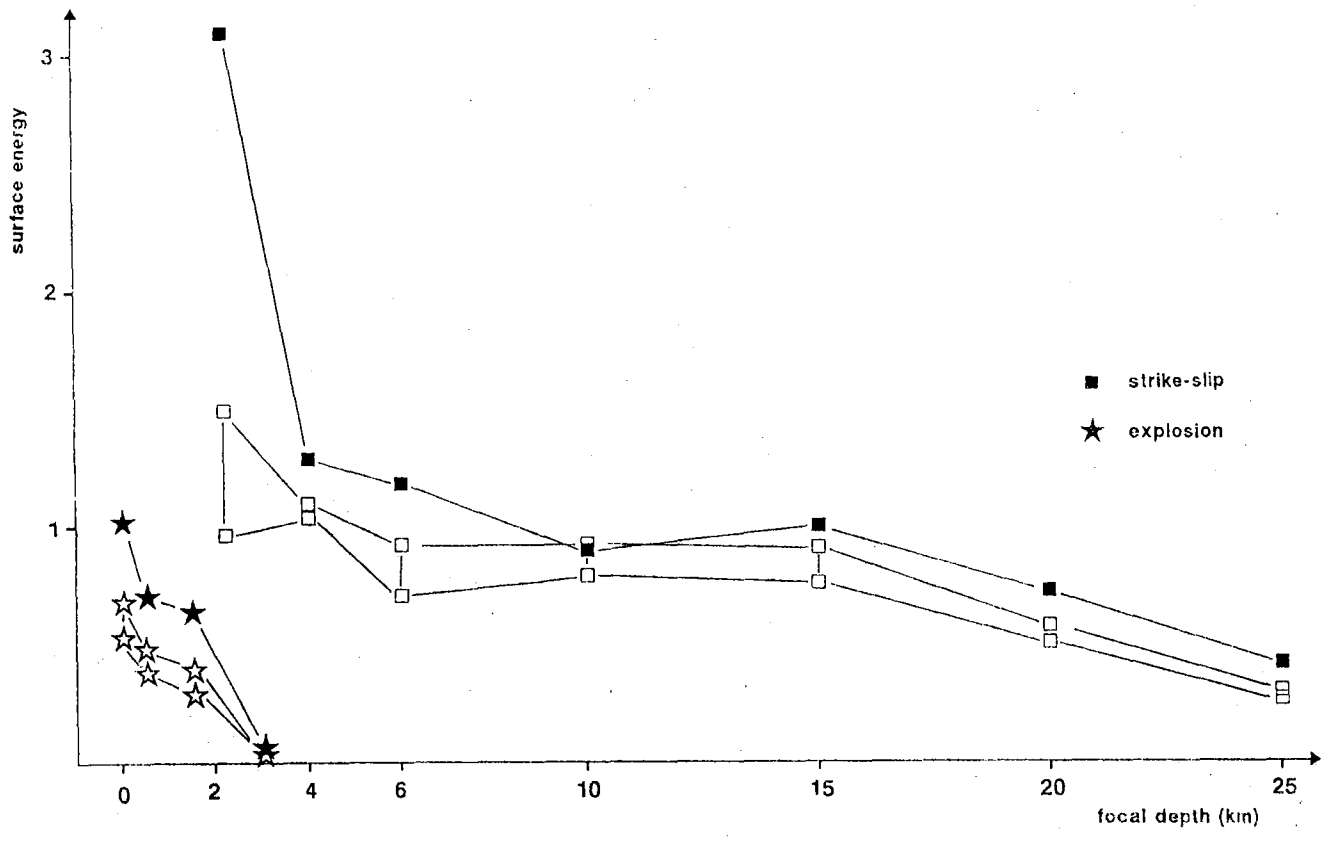

Fig. VII.3.5. Surface energy in the Lg wave measured on the vertical component before (filled symbol) and after propagation across the Central Graben (open symbol), as a function of source type and depth. The minimum and maximum values of transmitted surface energies averaged over different source-graben distances for the four Graben models are represented. The energy scale is only relative since no physical source size is included in the modelling.

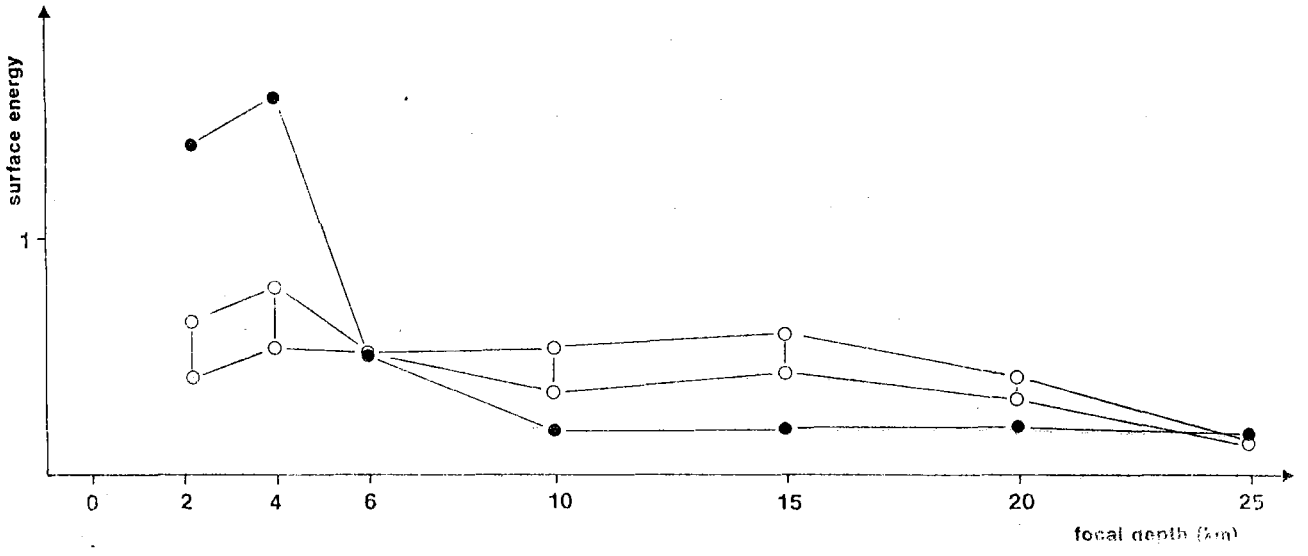

Fig. VII.3.6. The same as Fig. VII.3.5 for Viking Graben-type events.

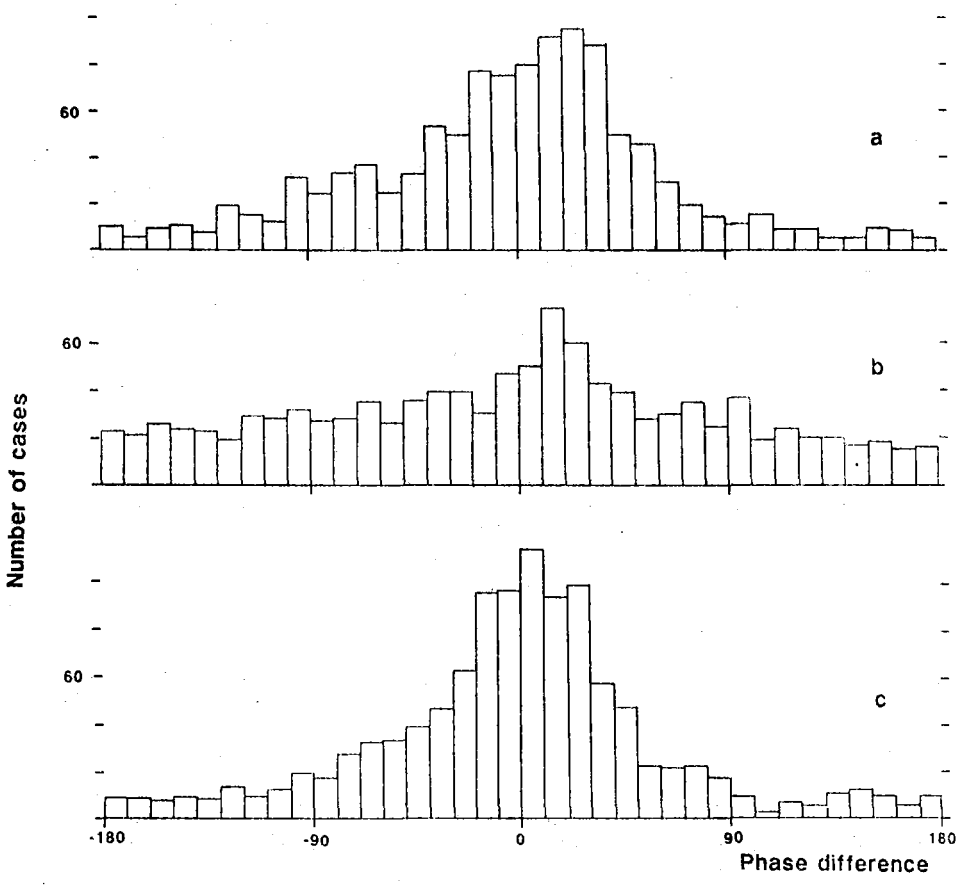

Fig. VII.3.7. Histogram of the phase difference between Lg modes at periods 1.0 and 1.02 s after propagation across model 1, for: a) an explosion at the surface; b) a Viking Graben-type event at 2.2 km focal depth; and c) a Viking Graben-type event at 15 km focal depth, and, in all cases, distances from the graben ranging from 0 to 1000 km.

VII.4 The August 8, 1988, Møre Basin earthquake: Observed ground motions and inferred source parameters

An earthquake of magnitude around 5.2 occurred in the Møre Basin on August 8, 1988, with tremors felt over most of southern and central Norway. The earthquake was the largest one in the region for at least 30 years, with a focal mechanism solution that indicates thrust faulting along a NNE-SSW striking fault plane, in response to E-W compressional stress. The seismic moment was of the order of 10^{17} Nm, with indications of a scaling consistent with an ω-square source model. A major source of uncertainty in this analysis is tied to anelastic attenuation.

Background seismicity

The seismicity of this part of Norway and the Norwegian Continental Shelf is shown in Fig. VII.4.1, where three different time periods have been plotted, with different symbols. The map indicates a reasonably good correlation between seismicity and regional geological features such as faults, fault zones, fracture zones and grabens, and there are also indications of the seismicity following the continental margin. The map moreover shows a certain bias between the different time periods in that the areas south of 63°N obviously are better covered in terms of microseismic surveillance during the 1980s (Bungum, 1988).

Epicenter location

The location of the August 8, 1988, earthquake in the Møre Basin is shown in Fig. VII.4.1 at 63.7°N, 2.4°E, slightly west of most earlier events in this area, but still east of the prominent Færøe-Shetland Escarpment. The earthquake was widely recorded on seismic instruments throughout northern Europe and the entire world. Nearly 80 seismic phases have been reported, all within the distance range of 300 to 1300 km. Experiments with locating the event with subsets of these data insured the consistency and reliability of the location. No reliable depth estimate is yet available, however (Hansen et al, 1988).

Felt effects and magnitude

This earthquake was widely felt throughout much of central and southern Norway, along the coast from Stavanger to Mo i Rana, as well as in southeastern Norway and in Sweden. Responses to questionnaires sent out by the Seismological Observatory in Bergen give felt radii of about 300 and 440 km for intensities IV and III, respectively. In using relationships developed recently between felt area and surface wave magnitude M_S (Muir Wood and Woo, 1987), this results in M_S values of 5.2 and 5.3, respectively. In comparison, an M_S value of 5.1 ± 0.24 has been computed by N.N. Ambraseys for this earthquake, while NORESS data have given an M_L value of 5.2. This magnitude makes this earthquake the largest one in the region for at least 30 years, possibly even the largest one since 1895 (Hansen et al, 1988; Bungum and Selnes, 1988).

Focal mechanism

The sense of faulting for this earthquake was explored through the use of the direction of vertical motion of about 50 of the first arriving P-phases for all available recordings. A focal mechanism solution, using this approach, is given in Fig. VII.4.2, where a combination of local and teleseismic data helps in constraining the nodal planes. From the graph, the faulting parameters for the two planes are strike 20°E, dip 46° and rake (slip) 116°, and strike 165°E, dip 50° and rake 66°, respectively. The solution leaves an ambiguity as to which of the two planes is the faulting plane, but in either case this solution gives a reverse mechanism. From the geologic data, however (see Fig. VII.4.1), we find that the preferred fault plane for this earthquake is the one striking 20°E. It can be seen from Fig. VII.4.2 that this northeasterly striking plane is only constrained by the stations whose azimuths vary from about 40° through about 90°. These are the stations of the SEISNOR network and ARCESS. The sense of first motion changed from dilatation to compression through the middle of this network of stations, allowing for a well-constrained fault plane solution (Hansen et al, 1988).

Observed ground motions

An earthquake of magnitude 5.2 naturally causes most conventional seismometers within regional distance ranges to saturate. Unclipped

recordings have, however, in the present case been obtained at three sites: (1) Molde (MOL) accelerometer site within the SEISNOR (Northern Norway) network (288 km); (2) Sulen (SUE) accelerometer site within the Western Norway network (318 km); and (3) NORESS HF (high frequency) and IP (intermediate period) elements (578 km). Since all of these moreover yield broadband recordings, they become especially valuable in terms of inferences about source parameters (NORSAR and Risk Engineering, Inc., 1988).

Observed source displacement spectra for these stations are shown in Fig. VII.4.3, where the time series were rotated to yield the radial (R) and the transverse (T) components. The data are corrected for system response (including a special processing of the accelerometer data), and converted from acceleration to displacement for Molde and Sulen and from velocity to displacement for NORESS (including a careful bandpass filtering in both cases). Energy spectra are then estimated as a basis for the plotted displacements, with a time window covering 24 seconds of the Lg waves.

What is seen from Fig. VII.4.3 is that the observed displacements fall off with frequency at a rate not very different from ω^2 (as indicated by straight lines). At higher frequencies, the slope decreases somewhat, possibly influenced by noise, and at low frequencies it should be kept in mind that the spectra are certainly affected by noise. The filters used in processing these data have been defined at lower cutoffs at 0.20 Hz for Molde (where quantization noise also may have been a problem) and Sulen, at 0.15 Hz for NORESS IP, and at 0.80 Hz for NORESS HF.

Corrected ground motions

In order to be able to compare the observed ground motion displacement spectra more conveniently, we have corrected all of them for the effects of geometrical spreading and anelastic attenuation back to a reference distance of 10 km from the source, with results as shown in Fig. VII.4.4.

The correction used for geometrical spreading has been the commonly used model by Herrmann and Kijko (1983) in which there is a change from spherical to cylindrical spreading at a distance of 100 km:

$$G(R) = \begin{cases} R^{-1} & R < 100 \text{ km} \\ 0.01(R/100)^{-1/2} & R \geq 100 \text{ km} \end{cases}$$

For anelastic attenuation, we have for test and sensitivity purposes used two very different models, by Kvamme and Havskov (1988):

$$Q = 120 \cdot f^{1.1} \qquad \text{(Model 1)}$$

and by Sereno et al (1988):

$$Q = 560 \cdot f^{0.26} \qquad \text{(Model 2)}$$

The first of these has been developed from spectral ratio and coda decay methods based on data typically within a 100-300 km distance range, while the second has been developed from a simultaneous inversion for seismic moment and apparent attenuation based on data between 200 and 1400 km. The first model covers 2-15 Hz, and the second 1-7 Hz.

Even with these differences in mind, it is not obvious which one of the two models will be most appropriate in the present case. With such large differences in frequency sensitivity of the Q-models, however, it is understandable that the effects of the path corrections will be very different, as shown by Fig. VII.4.4. It is useful here to note that if the observed and corrected spectra have slopes proportional to f^{δ} and f^{γ}, respectively, then the following frequency sensitivity of the Q model will be required ($Q = Q_o f^{\eta}$):

$$\eta = 1 - \log\left[1 + \frac{vQ_o(\delta-\gamma)\ln 10}{\pi R}\right]$$

where v is wave velocity and R is distance. This relation shows that if one requires the observed slope to be maintained after corection ($\delta = \gamma$), then Q must be directly proportional to frequency ($\eta = 1$).

From Fig. VII.4.3 it is seen that the observed spectral slopes are reasonably close to ω^2 for most of the data, at least in the 1-5 Hz range. This slope is therefore more or less maintained through the path correction when using the Model 1 attenuation ($\eta = 1.1$) as shown in Fig. VII.4.4, which in turn gives indications of a source model close to the standard ω^2 Brune model (see also Chael and Kromer, 1988). The Model 2 attenuation, on the other side, is more difficult to reconcile with this particular set of data.

Source displacement spectra and seismic moment

From the observed displacement spectra in Fig. VII.4.3 (or from the corrected ones in Fig. VII.4.4), source displacement spectra are obtained simply by correcting all the way back to the source, with the following parameters involved:

$$M_\omega = 4\pi\rho v^3 (S \cdot G \cdot P)^{-1} \Omega_\omega$$

where $P = \exp(\omega R/vQ)$ is anelastic attenuation, G is geometrical spreading as defined above, S is radiation pattern coefficient (0.6) times free-surface amplification (2.0) divided by a possible vectorial partitioning of energy ($\sqrt{2}$), v is wave velocity, ρ is density, and Ω_ω is the observed displacement spectrum. In applying these corrections with a Model 1 attenuation, we get source displacement spectra as shown in Fig. VII.4.5, where a seismic moment of the order of 10^{17} Nm (10^{24} dyne·cm) is indicated. In using the Hanks and Kanamori (1979) moment magnitude relationship

$$M_W = 2/3 \log M_O - 6.0$$

we then get $M_W = 5.3$, which is quite consistent with the other magnitude estimates discussed above. For an earthquake this size, the

Brune source model gives a corner frequency at 0.8 Hz for 100-bar stress drop.

It is not possible from Fig. VII.4.5, however, to determine corner frequency with any reasonable accuracy. The reason for this is partly low frequency noise (as mentioned above), but primarily the fact that the Q-model ($Q = 120 \cdot f^{1.1}$) most probably is not applicable for frequencies below 1 Hz. A lower limit in Q, possibly even combined with an increase towards lower frequencies (Aki, 1980), would yield the low frequency asymptotic effects called for by the commonly accepted source models. The sensitivities and the uncertainties involved here are properly illustrated by the low frequency differences between the two correction models in Fig. VII.4.4: one order of magnitude difference at a distance of about 300 km (Molde, Sulen) and two orders of magnitude differences at about twice that distance (NORESS).

Another question that is raised from the present observations is concerned with the small differences between the Lg amplitudes at Molde/Sulen as compared to NORESS. In the corrected spectra (see Fig. VII.4.5) this shows up in the higher NORESS levels, in spite of the fact that the same time window has been used in the two cases (as compared to using comparable group velocity windows). Since we have not found any technical reasons for this difference (such as errors in gain) we assume that the reason must be tied to Lg wave propagation characteristics that are not being adequately predicted by the models used here.

Concluding remarks

The questions raised here call for continued efforts aimed at resolving existing uncertainties in our knowledge about anelastic attenuation over a wider range of frequencies.

H. Bungum

References

Aki, K. (1980): Attenuation of shear-waves in the lithosphere for frequencies from 0.05 to 25 Hz. Phys. Earth Planet. Inter., 21, 50-60.

Brune, J.N. (1970): Tectonic stress and spectra of seismic shear waves from earthquakes. J. Geophys. Res., 75, 4997-5009. (Correction: J. Geophys. Res., 76, 5002 (1971)).

Bungum, H (1988): Earthquake occurrence and seismotectonics in Norway and surrounding areas. In: S. Gregersen and P. Basham (eds.): Earthquakes at North Sea Passive Margins: Neotectonics and Postglacial Rebound, Kluwer Academic Publ., in press.

Bungum, H. and P.B. Selnes (1988): Earthquake Loading on the Norwegian Continental Shelf - Summary Report. Norwegian Geotechnical Institute and NORSAR, 36 pp.

Chael, E.P. and R.P. Kromer (1988): High-frequency spectral scaling of a main shock/aftershock sequence near the Norwegian coast. Bull. Seism. Soc. Am., 78, 561-570.

Hanks, T. and H. Kanamori (1979): A moment magnitude scale. J. Geophys. Res., 84, 2348-2350.

Hansen, R.A., H. Bungum, L.B. Kvamme, A Dahle and J. Havskov (1988): The 1988 Møre Basin Earthquake. Report for the SEISNOR Steering Committee, 27 pp.

Havskov, J. and H. Bungum (1987): Source parameters for earthquakes in the northern North Sea. Nor. Geol. Tidsskr., 67, 51-58.

Herrmann, R.B. and A. Kijko (1988): Modeling some empirical component Lg relations. Bull. Seism. Soc. Am., 73, 157-171.

Kvamme, L.B. and J. Havskov (1988): Q in southern Norway. Bull. Seism. Soc. Am., in press.

Muir Wood, R. and G. Woo (1987): The Historical Seismicity of the Norwegian Continental Shelf, ELOCS (Earthquake Loading on the Norwegian Continental Shelf) Report 2-1, 117 pp.

NORSAR and Risk Engineering, Inc. (1988): Ground motions from earthquakes on the Norwegian Continental Shelf. Report for Den norske stats oljeselskap a.s., 100 pp.

Sereno, T.S., S.R. Bratt and T. Bache (1988): Simultaneous inversion of regional wave spectra for attenuation and seismic moment in Scandinavia. J. Geophys. Res., 93, 2019-2035.

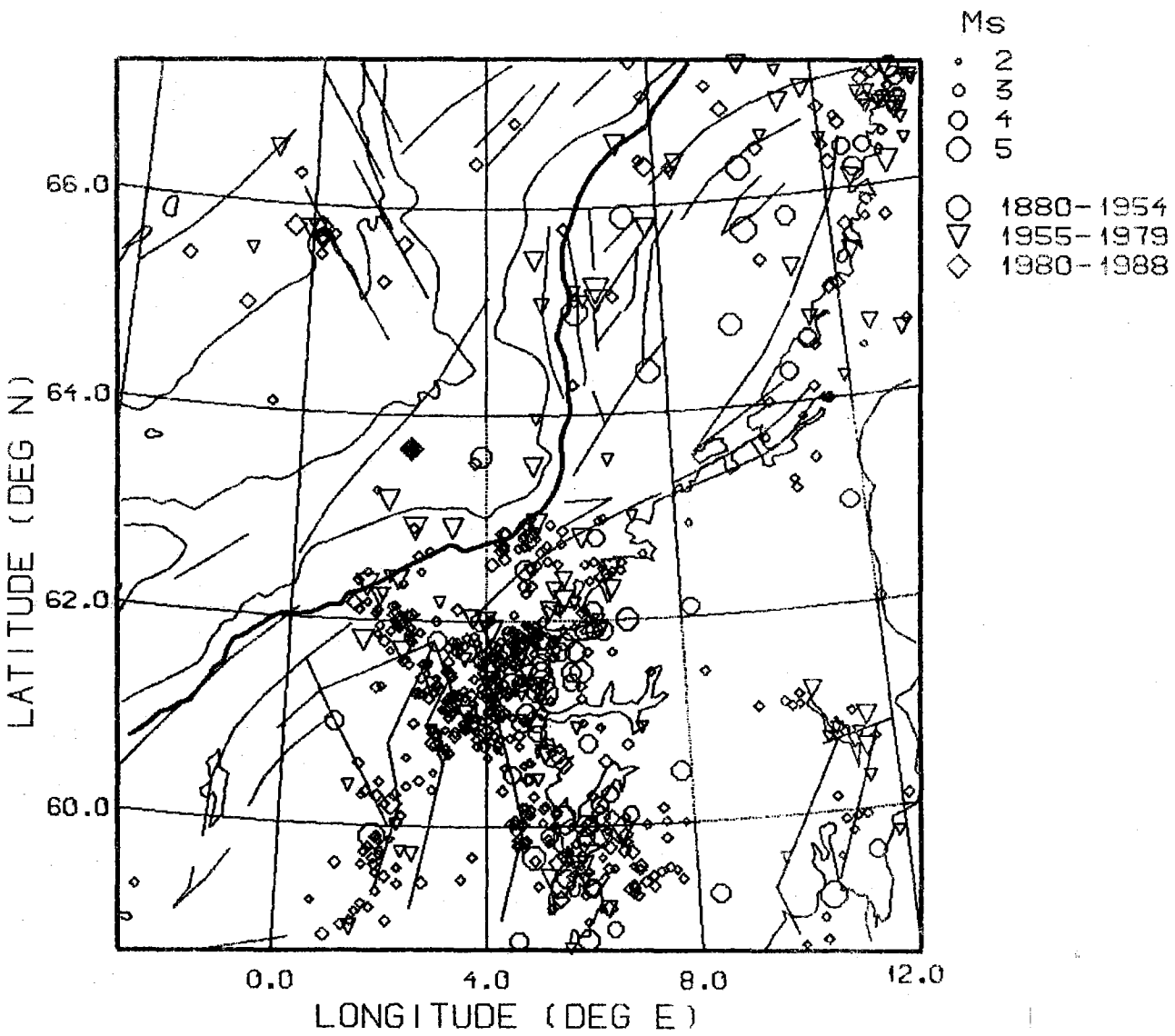

Fig. VII.4.1. Location of the 08.08.88 Møre Basin earthquake (black symbol at 63.7°N, 2.4°E) together with background seismicity for three different time periods, structural information (faults and fracture zones) and bathymetric contours (heavy line is shelf edge).

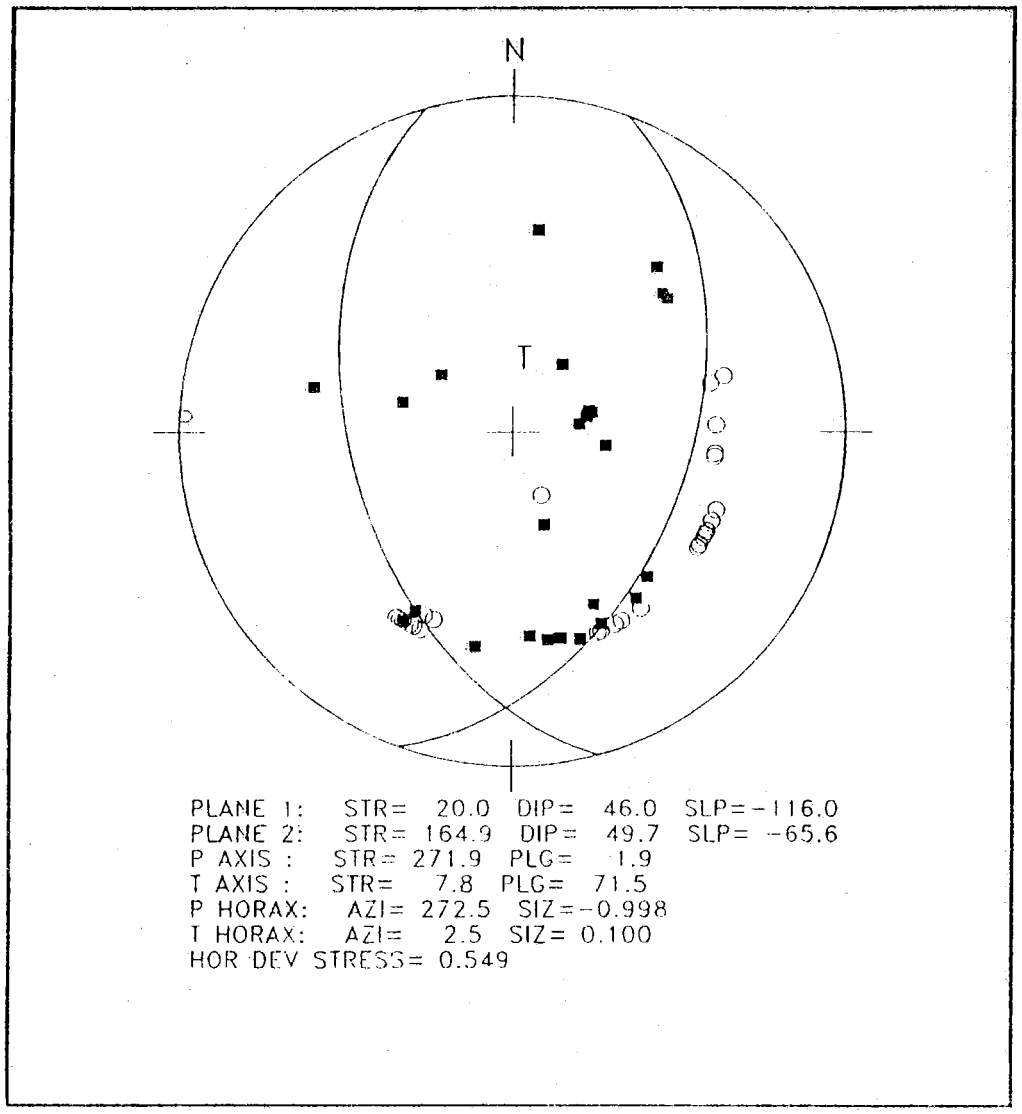

Fig. VII.4.2. Focal mechanism solution (lower hemisphere stereographic projection) for the August 8, 1988, earthquake, based on first motion readings (filled symbols for compressions, open symbols for dilatations) from both local, regional and teleseismic data.
(From Hansen et al, 1988)

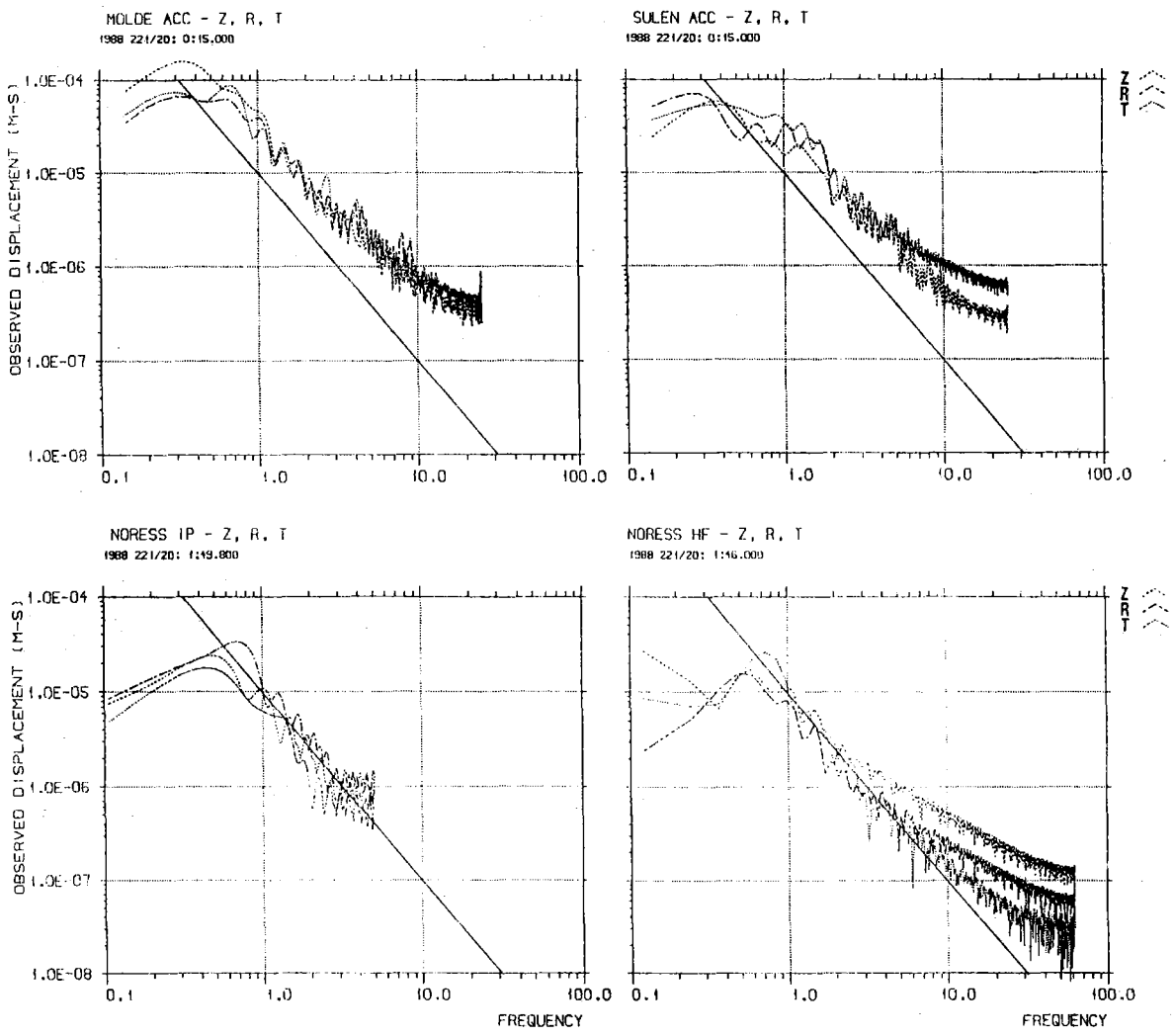

Fig. VII.4.3. Observed ground motion displacement (in m·sec) vs. frequency for Molde (288 km), Sulen (318 km) and NORESS IP and HF (578 km). The data for each station are rotated so as to yield vertical (Z), radial (R) and transverse (T) components. The straight lines correspond to a slope proportional to ω^2.

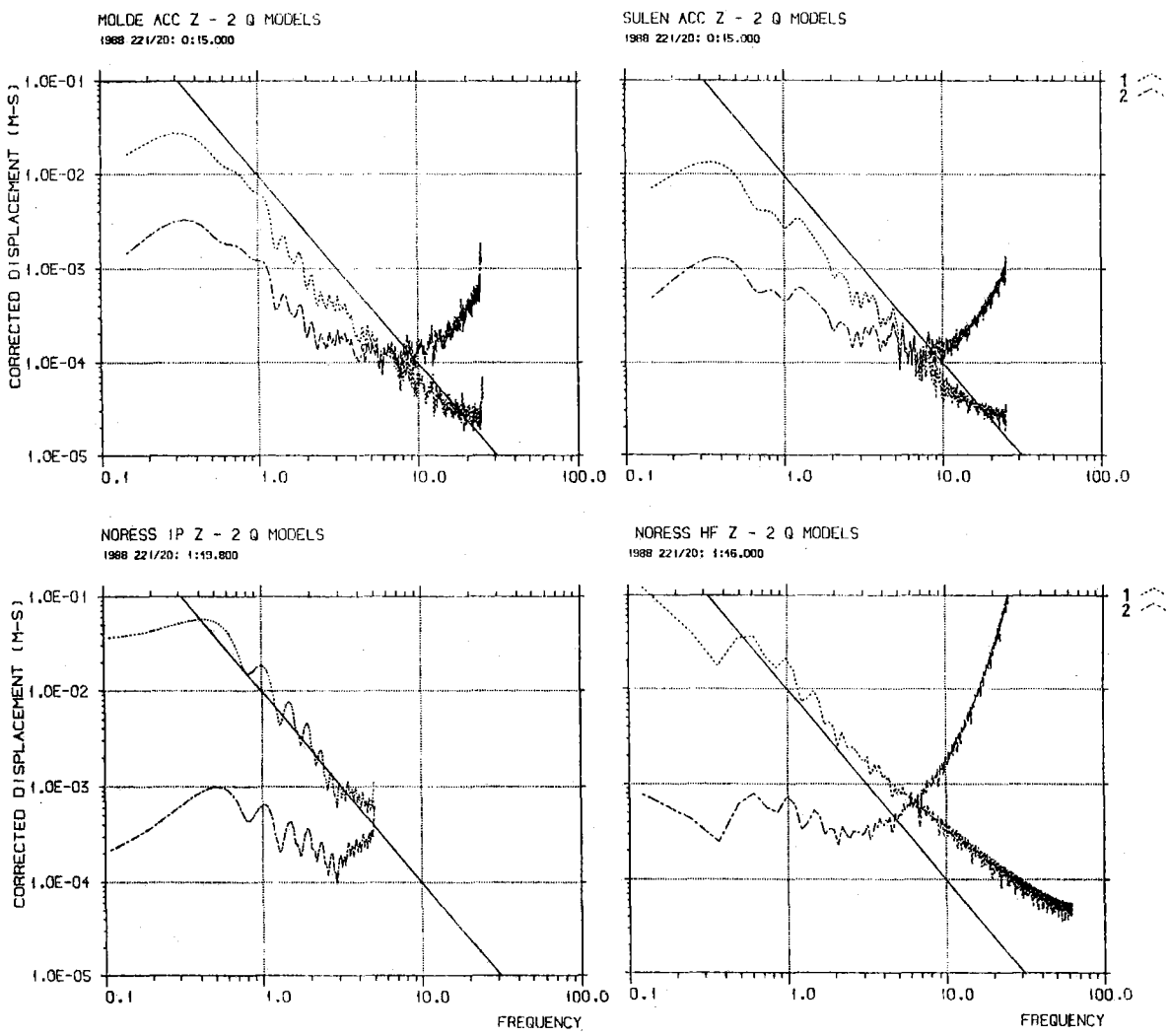

Fig. VII.4.4. Ground motion displacement (in m·sec) vs. frequency for the same data as shown in Fig. VII.4.3 (but for the Z component only), path corrected back to a reference distance of 10 km from the source using the following two Q models: (1) Kvamme and Havskov (1988) and (2) Sereno et al (1988). The straight lines correspond to a slope proportional to ω^2.

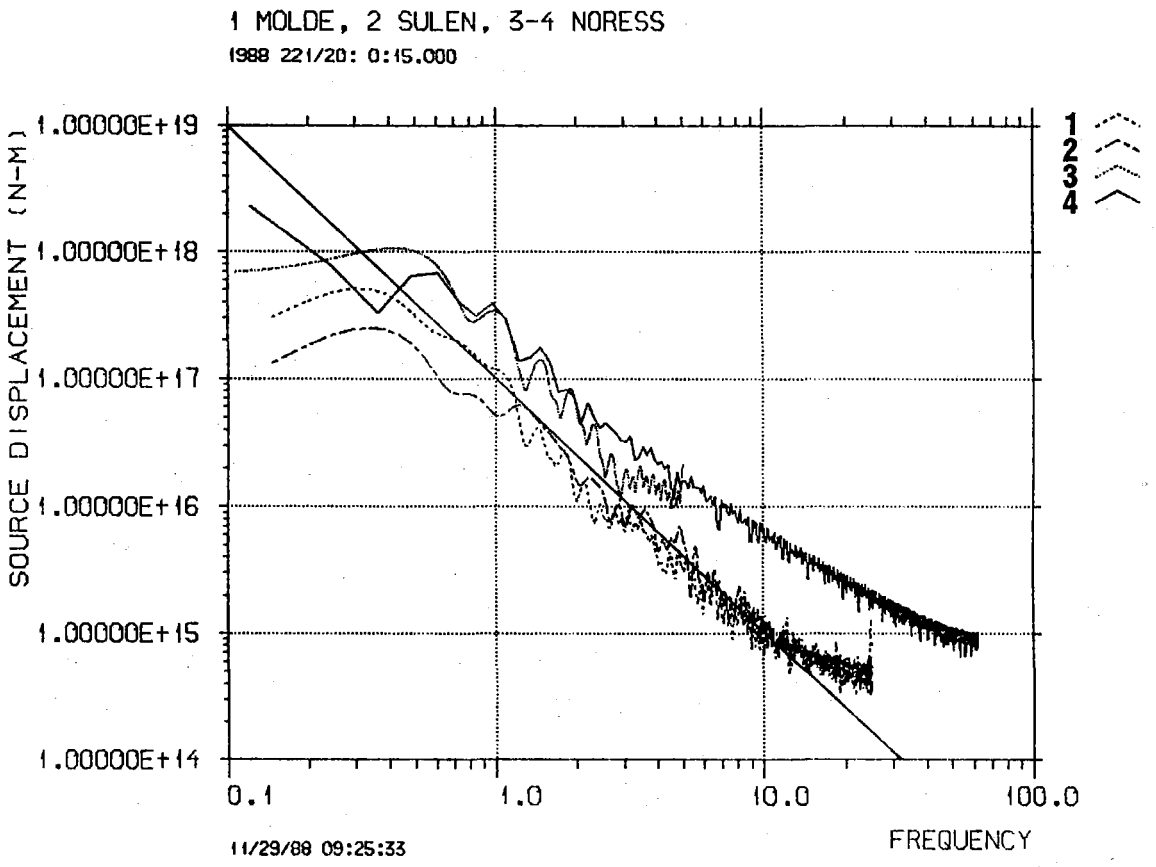

Fig. VII.4.5. Source displacement spectra for the August 8, 1988, earthquake, with corrections for geometrical spreading (Herrmann and Kijko, 1983) and anelastic attenuation (Kvamme and Havskov, 1988). The plot indicates a seismic moment of the order of 10^{17} Newton-meters (equivalent to 10^{24} dyne-cm). The straight line indicates a slope proportional to ω^2, and curves 1 through 4 are Molde, Sulen, NORESS IP and NORESS HF, respectively.

VII.5 Analysis of regional seismic events using the NORESS/ ARCESS/FINESA arrays

This contribution comprises two separate investigations related to analysis of events recorded on the three regional arrays NORESS, ARCESS and FINESA in Fennoscandia. The first investigation is an evaluation of the performance of the recently upgraded FINESA array in Finland, whereas the second investigation utilizes data recorded simultaneously on all three arrays in producing joint event locations.

An evaluation of the performance of the upgraded FINESA array

A description of the FINESA array is given in Korhonen et al (1987). In early 1988, the geometry of the FINESA array was expanded by adding five elements to the array, as shown in Fig. VII.5.1. The FINESA array geometry currently comprises 15 vertical only seismometers within an aperture of 2 km.

FINESA data are recorded on magnetic tape at the array site, and the tape recording is normally event triggered by a built-in voting detector. In order, however, to properly evaluate the performance of the upgraded FINESA array, data were recorded continuously for a 14-day period during March 8-21 of 1988. The tapes were played back and checked at NORSAR, and approximately 55% of the data for this 14-day period could be recovered and were hence subjected to detection processing. The remaining 45% of the data could not be read due to various problems with the tapes, like parity errors, etc.

A beam deployment comprising 72 beams (66 coherent, 6 incoherent) was used for the detection processing of the continuous FINESA data. The beam deployment used is in agreement with the recommendations by Kværna et al (1987) and Kværna (1988). The detection processing results in lists with attributes for each detected signal, like detection time, signal frequency, phase velocity and arrival azimuth. These lists were compared against the regional Finnish bulletin, issued by the Univer-

sity of Helsinki, and the results of the comparison are given in Table VII.5.1. Only those bulletin events occurring when the FINESA array was operating properly are included in the table.

Signals detected on FINESA were associated to the Helsinki bulletin events by requiring a reasonable match of FINESA detection parameters (arrival time, phase type from velocity, and arrival azimuth) with the corresponding ones predicted from the information in the Helsinki bulletin. From Table VII.5.1 we see that out of the 103 reference events listed, 99 had at least one detected P- or S-phase, i.e., 96 per cent. Two of the four events that were not detected, occurred at the Lahnaslampi mine in Finland (64.2°N, 28.0°E), at a distance of 322 km from FINESA. Most blasts at Lahnaslampi are quite small, and are not detected by FINESA. The two remaining events were both small ones (magnitude less than 2 for one event; magnitude not given for the other) at ranges more than 700 km from FINESA.

These results for the upgraded FINESA array are quite encouraging. An investigation based on 14 days of continuous FINESA data from 1986 (with the original array geometry) concluded that 84 per cent of the regional events listed in the Helsinki bulletin were detected by the array (Korhonen et al, 1987). The addition of the five extra sensors to the array geometry thus resulted in a considerable improvement of the array's capability to detect small regional events. It is evident that the FINESA array in its current configuration represents a valuable addition to the network of regional arrays in Fennoscandia. To fully exploit the FINESA data, however, it will be necessary to upgrade the on-site data acquisition system and also provide a communications link. This will allow real time transmission of FINESA data to the NORSAR data processing center at Kjeller for processing jointly with NORESS and ARCESS data.

Joint event locations from three-array data

Data recorded at FINESA were used together with NORESS and ARCESS data in assessing the capabilities of this three-array network in locating events in the Fennoscandian region. A set of 10 events, for which there was at least one detected phase for each array, was selected for an event location experiment. The events are listed in Table VII.5.2 and shown in Fig. VII.5.2. The event magnitudes range from less than 2.0 to 3.2. The origin times and geographical coordinates for the 10 events are taken from the Helsinki bulletin.

The continuous processing of data recorded at each of the three regional arrays in Fennoscandia provides estimates of arrival times and back azimuths. These parameters together with the associated uncertainties were used as input to the TTAZLOC program developed by Bratt and Bache (1988). TTAZLOC incorporates the arrival time and azimuth data into a generalized-inverse location estimation scheme, and can be applied to both single-array and multiple-array data.

Figs. VII.5.3a, 3b and 3c show ARCESS, NORESS and FINESA data, respectively, for event 3 in Table VII.5.2. The panels show on the top three P-wave beams for three different frequency bands. The beams were steered according to the phase velocity and azimuth of the peak of the fk-spectrum computed as part of the online detection processing. The three lower traces of the panels show data for a single channel, also for three different frequency bands. The detection times for the phases used in the location experiment are marked by arrows. The figures show that this event is recorded with a high SNR ratio at the closest array (FINESA), whereas it is marginal at the two other arrays, but is detected due to the SNR gain that is achieved through beamforming. Very simple rules based on phase velocity and relative arrival times and amplitudes are used in the phase assignment, and Pn, Sn and Lg phases only are considered. Another candidate would be the Rg phase, which is clearly seen in Fig. VII.5.3c, following the Lg phase (traces no. 4 and 5 from the top).

Table VII.5.2 gives the results of the location experiment. On the average, the joint three-array locations deviate from the network locations published in the Helsinki bulletin by 16 km. Two-array and one-array locations were computed for all combinations of events and array sub-networks, also using the TTAZLOC algorithm. The resulting average deviations from the network solutions are 26 and 68 km, respectively.

The results for one-array and two-array locations are in general agreement with what has previously been reported (e.g., Mykkeltveit and Ringdal (1988) found an average deviation of 34 km from the Helsinki bulletin locations, using data from seven regional events recorded at NORESS and ARCESS). The improvement in the location accuracy when invoking data from three arrays is significant, and we consider the results reported here as quite promising, when taking the following into account: The arrival times used were those determined automatically by the online processing. It is conceivable that human intervention for adjustment of arrival times and/or refinement of the automatic procedure would improve the location estimates. Only standard travel time tables for the phases Pn, Sn and Lg were used. The introduction of regionalized travel time tables is likely to result in improvements. Finally, master event location schemes of various kinds hold considerable promise and are expected to further enhance the capabilities of accurately locating regional events.

S. Mykkeltveit
J. Fyen
T. Kværna
M. Uski, Univ. of Helsinki

References

Bratt, S.B. and T.C. Bache (1988): Locating events with a sparse network of regional events. Bull. Seism. Soc. Amer., 78, 780-798.

Korhonen, H., S. Pirhonen, F. Ringdal, S. Mykkeltveit, T. Kværna, P.W. Larsen and R. Paulsen (1987): The Finesa array and preliminary results of data analysis. Univ. of Helsinki, Inst. of Seismology, Report S-16.

Kværna, T. (1988): On exploitation of small-aperture NORESS type arrays for enhanced P-wave detectability. Semiannual Tech. Summ., 1 Oct 1987 - 31 Mar 1988, NORSAR Sci. Rep. 2-87/88, Kjeller, Norway.

Kværna, T., S. Kibsgaard, S. Mykkeltveit and F. Ringdal (1987): Towards an optimum beam deployment for NORESS; experiments with a North Sea/Western Norway data base. Semiannual Tech. Summ., 1 Apr - 30 Sep 1987, NORSAR Sci. Rep. 1-87/88, Kjeller, Norway.

Mykkeltveit, S. and F. Ringdal (1988): New results from processing of data recorded at the new ARCESS regional array. Semiannual Tech. Summ., 1 Oct 1987 - 31 Mar 1988, NORSAR Sci. Rep. 2-87/88, Kjeller, Norway.

Date	Time	Lat. (°N)	Lon. (°E)	Magn.	Dist. (km)	P-det.	S-det.
88/03/08	06.01.42	61.2	27.1	<2	61	-	x
88/03/08	07.50.57	62.8	29.1	<2	215	x	x
88/03/08	13.03.50	62.2	23.3	<2	169	x	x
88/03/08	13.29.02	64.2	28.0	<2	322	-	-
88/03/08	14.25.10	62.1	26.4	<2	75	x	x
88/03/08	15.02.39	60.3	24.8	<2	145	x	x
88/03/09	12.05.43	64.2	28.0	<2	322	-	x
88/03/10	08.47.04	59.3	27.2	<2	247	x	x
88/03/10	09.22.08	59.3	27.6	<2	253	x	x
88/03/10	09.57.40	59.2	27.6	<2	264	x	x
88/03/10	10.41.14	59.3	27.6	<2	253	x	-
88/03/10	11.07.37	59.2	27.6	2.1	264	x	x
88/03/10	11.14.23	59.3	27.6	<2	253	x	x
88/03/10	11.25.34	59.5	25.0	2.2	224	x	x
88/03/10	11.49.54	59.3	27.6	<2	253	x	x
88/03/10	12.05.20	59.5	26.5	2.2	218	x	x
88/03/10	12.07.05	61.2	28.9	-	154	x	x
88/03/10	12.10.50	59.3	28.1	2.1	264	x	x
88/03/10	16.03.30	64.3	24.0	<2	335	x	x
88/03/10	16.20.56	62.0	24.4	<2	108	x	x
88/03/10	18.16.15	65.8	24.7	<2	491	-	x
88/03/10	18.29.30	67.1	20.6	2.2	684	x	x
88/03/10	20.27.28	63.6	26.2	<2	240	x	x
88/03/11	08.18.59	62.9	25.9	<2	163	x	x
88/03/11	09.23.17.	67.6	34.0	-	783	-	x
88/03/11	09.24.26	67.6	34.0	-	783	-	x
88/03/11	09.25.40	67.6	34.0	2.7	783	x	x
88/03/11	09.48.06	61.4	34.3	2.3	439	x	x
88/03/11	10.21.09	62.2	25.9	<2	85	x	x
88/03/11	10.21.35	59.3	27.6	2.2	253	x	x
88/03/11	10.56.54	59.5	25.0	2.1	224	x	x
88/03/11	11.27.25	59.3	27.6	<2	253	x	x
88/03/11	11.46.58	69.4	30.8	2.3	913	x	x
88/03/11	12.03.37	63.2	27.8	2.3	215	x	x
88/03/11	12.17.09	59.5	25.0	2.1	224	x	x
88/03/11	12.33.24	60.8	29.3	2.3	188	x	x
88/03/11	12.57.59	59.3	27.6	<2	253	x	x
88/03/11	13.33.05	59.3	28.1	<2	264	x	x

Table VII.5.1. Results from detection processing of FINESA data for the period 8-21 Mar 1988. The table lists the 103 events of the Helsinki bulletin that occurred while the FINESA system was operating properly during the 14-day period. The distance from the FINESA array is given for each event. The table indicates whether or not a P- or S-phase was detected on FINESA, that can be associated with the event in question. (Page 1 of 3)

Date	Time	Lat. (°N)	Lon. (°E)	Magn.	Dist. (km)	P-det.	S-det.
88/03/12	09.12.28	59.4	28.4	2.1	261	x	x
88/03/12	09.59.59	64.7	30.7	2.9	431	x	x
88/03/12	10.43.17	59.5	25.0	2.2	224	x	x
88/03/12	10.48.21	61.8	36.1	2.4	533	x	x
88/03/12	11.03.58	68.1	33.2	2.1	815	x	x
88/03/12	11.11.12	68.1	33.2	2.9	815	x	x
88/03/12	12.25.01	59.3	27.2	2.3	247	x	x
88/03/12	12.40.45	67.6	30.5	-	718	-	-
88/03/12	12.41.07	67.6	30.5	2.4	718	x	x
88/03/12	14.15.38	67.1	20.6	<2	684	-	x
88/03/13	06.49.10	67.7	33.7	2.4	786	x	x
88/03/14	09.01.41	59.3	27.6	<2	253	x	x
88/03/14	09.13.21	62.8	22.6	<2	236	x	x
88/03/14*	09.22.16	59.3	27.2	2.1	247	x	x
88/03/14	10.32.41	59.3	27.6	<2	253	x	x
88/03/14	10.35.25	59.3	27.6	<2	253	x	x
88/03/14	12.41.49	59.6	30.0	2.1	298	x	x
88/03/14	13.10.52	59.5	25.0	2.6	224	x	x
88/03/14	14.07.27	59.3	28.1	<2	264	x	x
88/03/15	08.59.57	67.6	34.0	<2	783	-	x
88/03/15	09.06.42	67.6	34.0	2.4	783	-	x
88/03/15	10.31.30	59.2	27.4	2.5	260	x	x
88/03/15	11.34.36	59.5	26.4	2.5	218	x	x
88/03/15	11.41.57	60.5	25.9	<2	106	x	x
88/03/15	11.26.30	61.6	21.7	<2	234	x	x
88/03/15	12.10.38	59.2	27.6	<2	264	x	x
88/03/15	12.11.37	59.2	27.6	<2	264	-	x
88/03/15	12.19.15	59.3	27.2	2.2	247	x	x
88/03/15	12.33.35	62.5	21.7	<2	258	x	x
88/03/15	12.40.39	59.4	28.5	<2	264	x	x
88/03/15	13.16.45	59.3	24.4	2.3	256	x	x
88/03/15	13.22.14	61.9	30.6	2.0	245	x	x
88/03/15	13.51.30	59.0	25.8	<2	273	x	x
88/03/15	14.09.35	59.5	25.0	<2	224	x	x
88/03/15	14.20.59	60.9	29.2	2.4	179	x	x
88/03/15	14.36.30	63.1	22.2	<2	273	x	x
88/03/15	14.39.35	59.5	25.0	2.3	224	x	x
88/03/15	17.57.51	65.8	24.7	<2	490	-	x
88/03/16	08.37.13	59.2	27.6	<2	264	x	x
88/03/16	09.44.50	69.6	29.9	2.4	926	x	-

---

* The origin time for this event is misprinted as 09.29.16 in the Helsinki bulletin

Table VII.5.1. (Page 2 of 3)

Date	Time	Lat. (°N)	Lon. (°E)	Magn.	Dist. (km)	P-det.	S-det.
88/03/16	10.25.03	59.3	27.6	<2	253	x	x
88/03/16	10.45.40	60.9	26.8	<2	72	x	x
88/03/16	11.26.47	59.2	27.6	<2	264	x	x
88/03/16	11.45.36	63.2	27.8	2.5	215	x	x
88/03/16	11.49.51	59.5	25.0	<2	224	x	x
88/03/16	23.04.26	67.8	20.0	<2	765	-	-
88/03/17	09.07.13	58.3	10.9	2.7	917	x	x
88/03/17	10.21.17	69.6	29.9	2.9	926	x	x
88/03/17	10.27.20	59.2	27.6	2.3	264	x	x
88/03/17	10.46.21	59.2	27.6	<2	264	x	x
88/03/17	11.18.48	59.3	27.2	2.3	247	x	x
88/03/17	12.02.23	64.2	28.0	<2	322	-	-
88/03/17	12.02.36	59.4	28.5	2.1	264	x	x
88/03/17	18.58.07	59.7	5.6	3.2	1135	x	x
88/03/18	05.16.20	69.2	34.7	2.6	952	x	x
88/03/19	10.04.08	61.1	30.2	<2	224	x	x
88/03/19	10.05.02	59.3	27.2	-	247	x	x
88/03/19	12.15.34	68.1	33.2	-	815	x	-
88/03/19	12.15.39	68.1	33.2	-	815	x	x
88/03/19	12.39.09	68.1	33.2	<2	815	x	x
88/03/19	13.03.39	67.6	30.5	-	718	x	x
88/03/19	13.03.54	67.6	30.5	-	718	x	x
88/03/19	13.07.00	61.9	30.6	2.6	245	x	x
88/03/19	13.42.33	67.6	30.5	<2	718	-	x
88/03/20	04.45.17	67.7	33.7	2.5	786	x	x

Table VII.5.1. (Page 3 of 3)

Event No.	Date	Time	Network Lat.	Network Lon.	Mag. M_L	No. of phases used	3-array 'error' (km)	Average 2-array 'error' (km)	Average 1-array 'error' (km)
1	88/03/12	14.15.38	67.1	20.6	<2	5	19	31	36
2	88/03/15	11.34.36	59.5	26.5	2.5	8	9	8	39
3	88/03/15	14.20.49.5	60.93	29.19	2.4	6	34	34	34
4	88/03/15	14.39.35	59.5	25.0	2.3	8	8	23	95
5	88/03/16	11.45.36	63.2	27.8	2.5	6	32	31	41
6	88/03/17	09.07.13.2	58.33	10.93	2.7	7	16	24	44
7	88/03/17	10.21.17	69.6	29.9	2.9	8	4	13	45
8	88/03/17	11.18.48	59.3	27.2	2.3	5	15	36	108
9	88/03/17	18.58.07.1	59.72	5.62	3.2	6	9	51	179
10	88/03/18	05.16.20	69.2	34.7	2.6	5	15	12	57
Average over 10 events							16	26	68

Table VII.5.2. Results from TTAZLOC location experiments using data from NORESS, ARCESS and FINESA. Epicentral location estimates are given as reported by the Helsinki bulletin for a set of ten regional events. The table gives the deviation from these reference locations, as inferred from the TTAZLOC experiments described in the text.

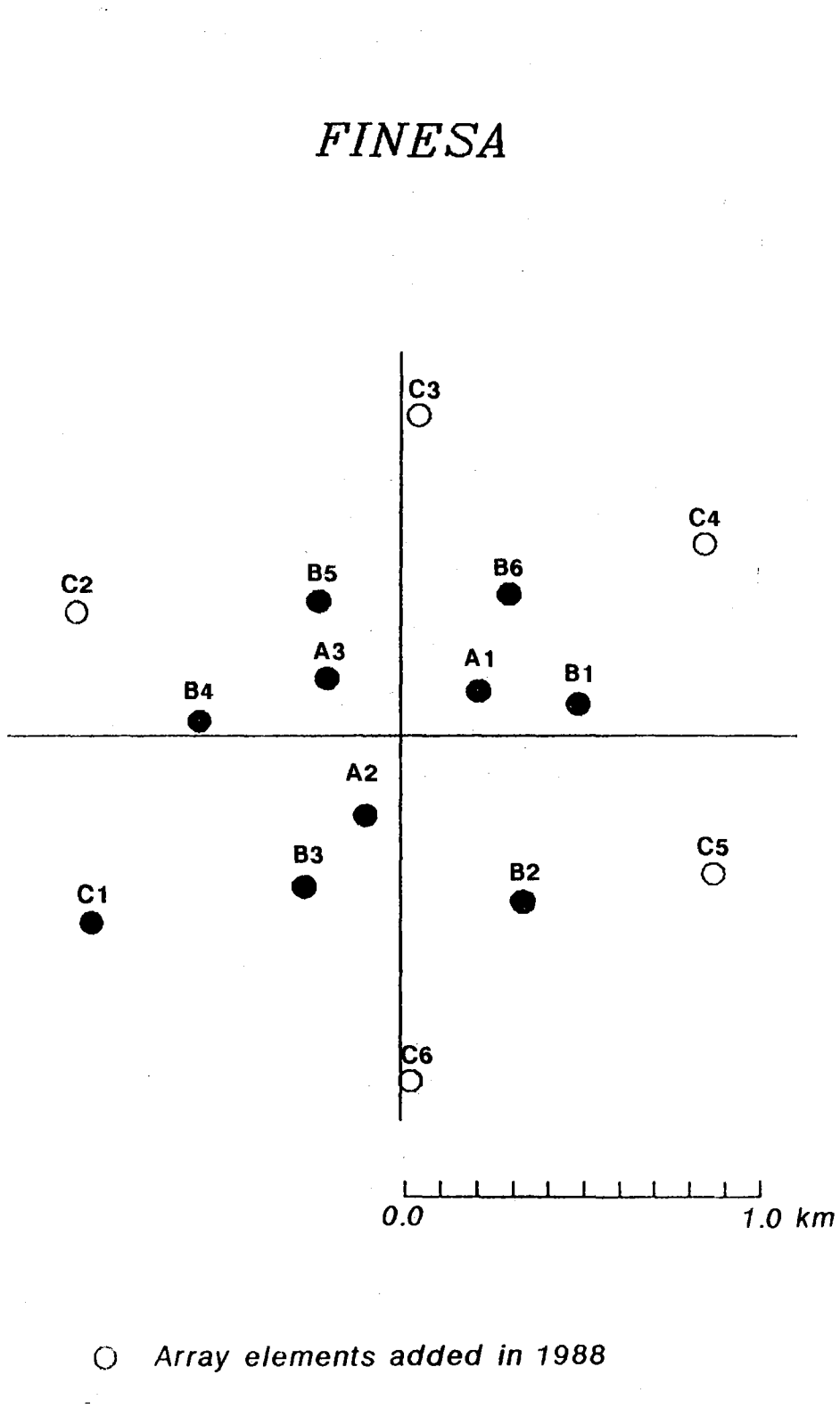

Fig. VII.5.1. The geometry of the FINESA array in Finland. Open circles denote array elements that were added in 1988.

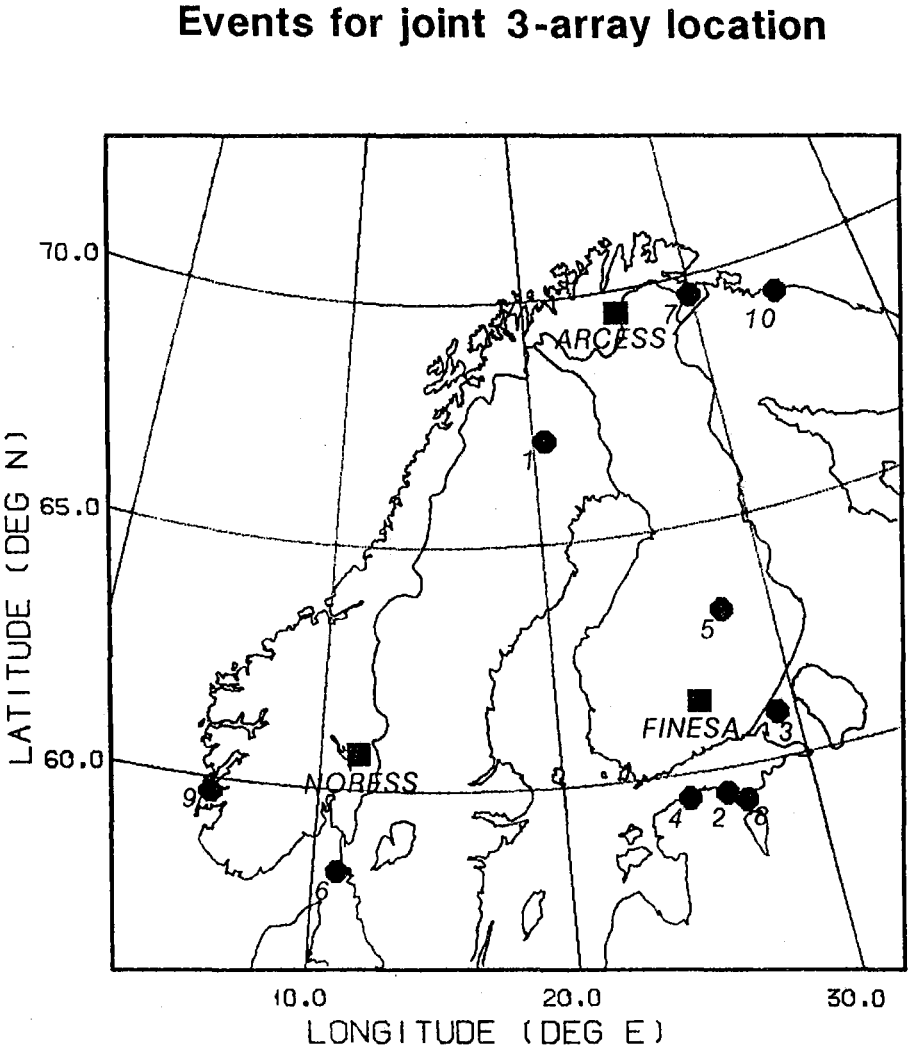

Fig. VII.5.2. The map shows the location of the three regional arrays NORESS, ARCESS and FINESA, as well as the location of ten events used in the TTAZLOC location estimation experiment.

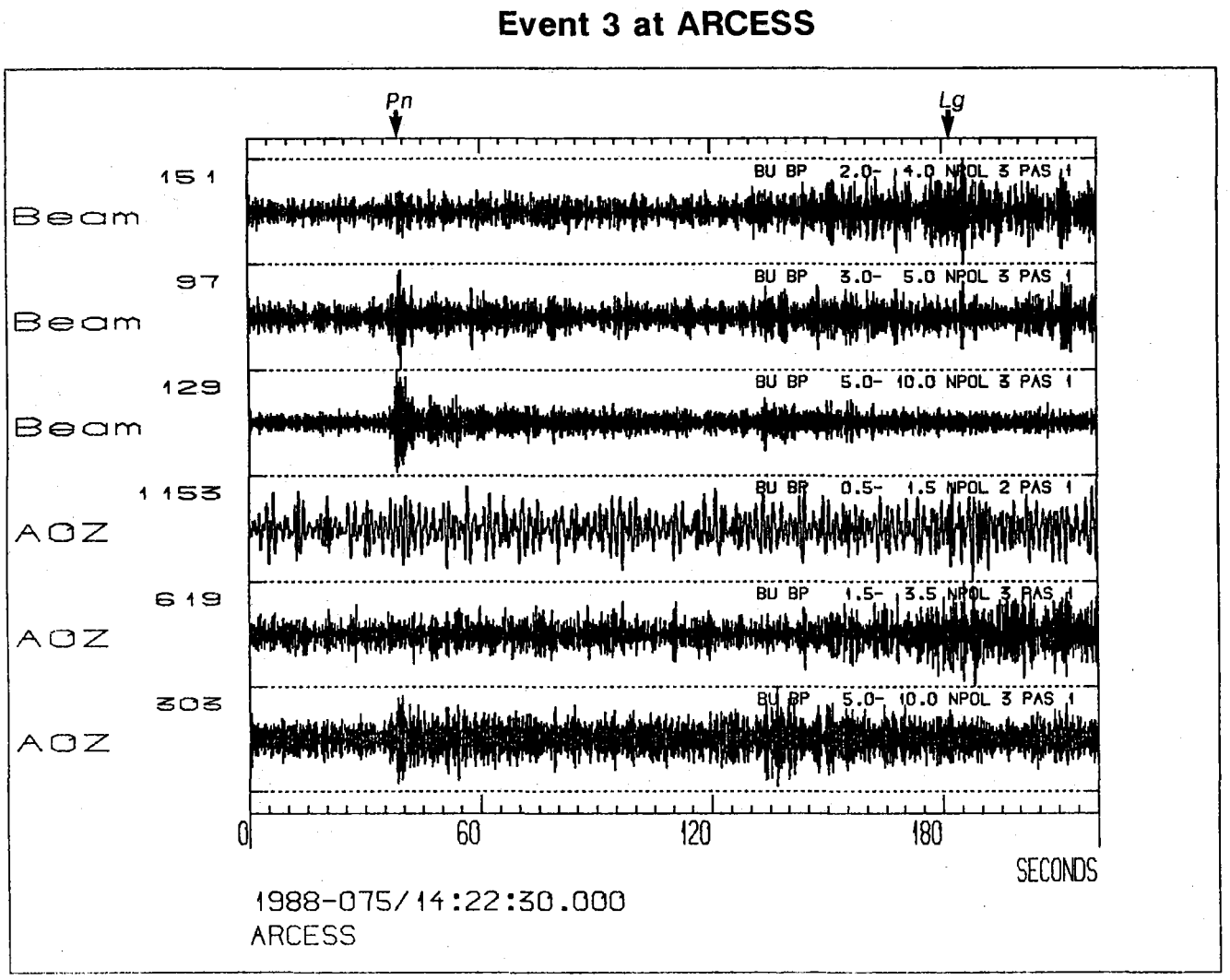

Fig. VII.5.3a. ARCESS data for event 3 in Table VII.5.2. The panel shows on top three P-beams steered towards the epicenter, for three different filter bands. The three bottom traces correspond to three different filters applied to the vertical sensor at site AO. The detection times (by the automatic online processor) for the phases Pn and Lg are indicated by arrows.

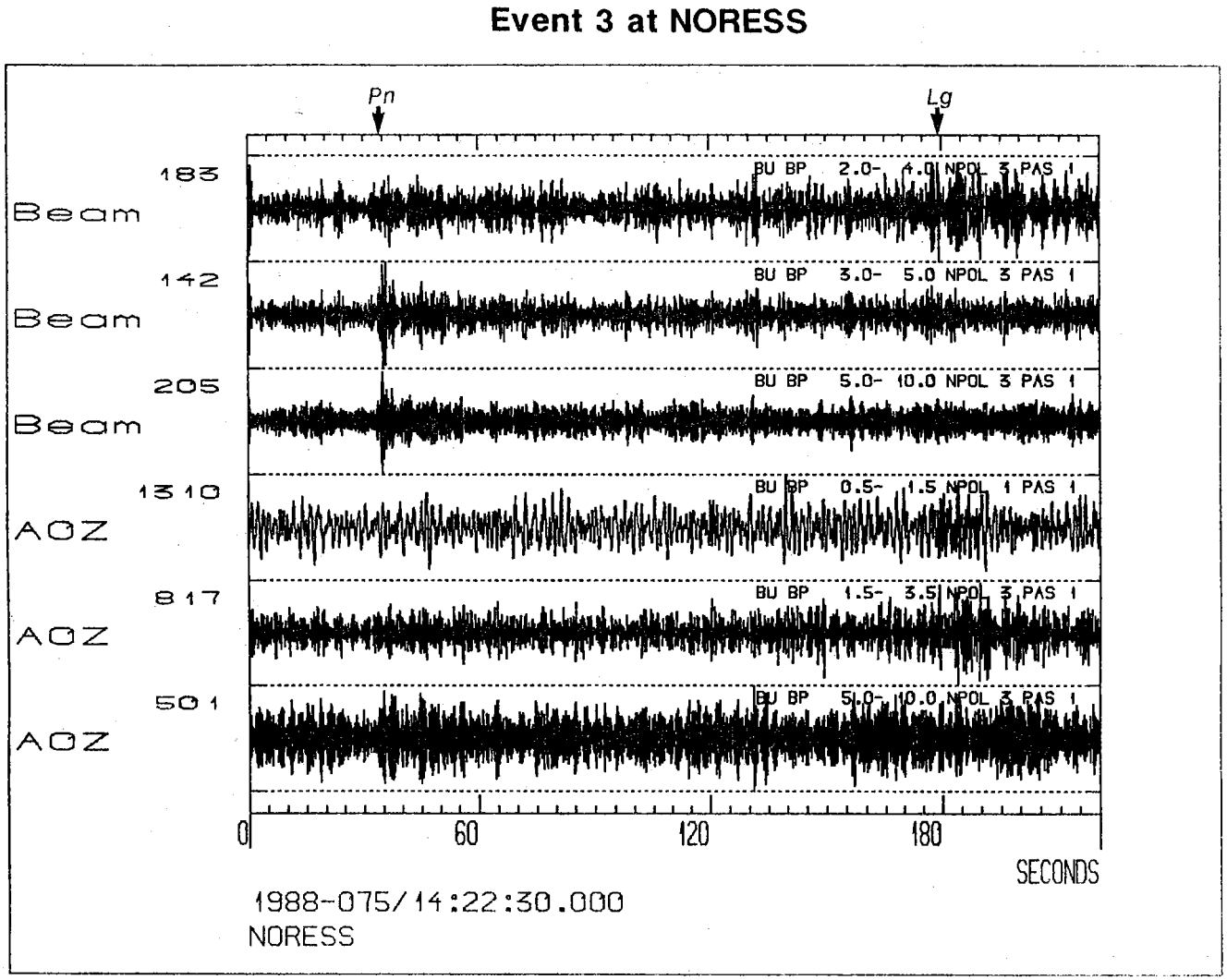

Fig. VII.5.3b. Same as Fig. VII.5.3a, but for NORESS data.

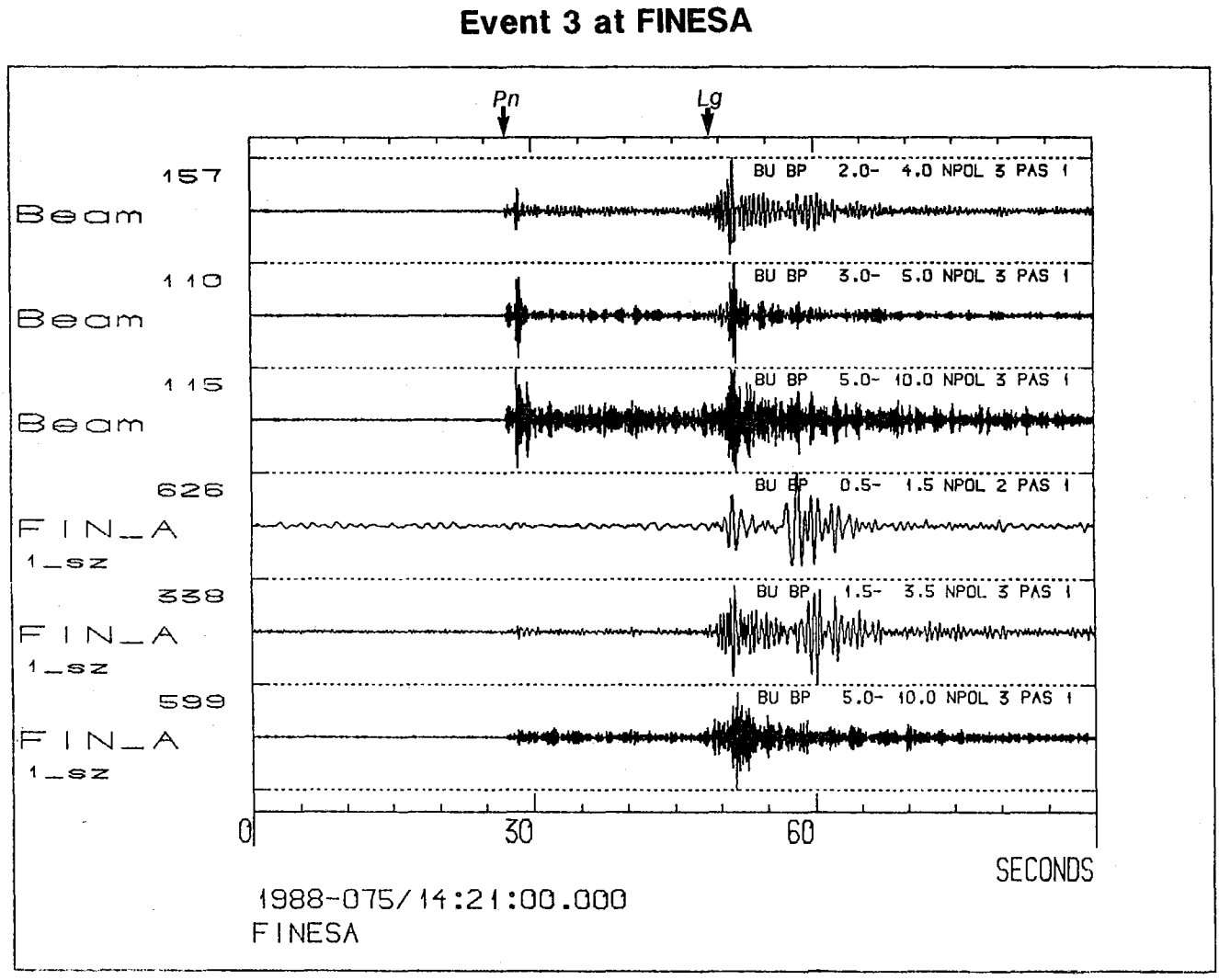

Fig. VII.5.3c. Same as Fig. VII.5.3a, but for FINESA data. The single channel data are taken from the sensor at site A1 (see Fig. VII.5.1).

VII.6 Comparative analysis of NORSAR and Gräfenberg Lg magnitudes for Shagan River explosions

Introduction

The seismic Lg wave propagates in the continental lithosphere and can be observed as far away as 5000 km in shield and stable platform areas (Nuttli, 1973; Baumgardt, 1985). Lg is generally considered to consist of a superposition of many higher-mode surface waves of group velocities near 3.5 km/s, and its radiation is therefore expected to be more isotropic than that of P waves. Thus, full azimuthal coverage is not essential for reliable determination of Lg magnitude. Furthermore, Lg is not affected by lateral heterogeneities in the upper mantle, which can produce strong focussing/defocussing effects of P-waves, and therefore contribute to a significant uncertainty in P-based m_b estimates.

Nuttli (1986a) showed that the amplitudes of Lg near 1 second period provide a stable estimate of magnitude, m_b(Lg) and explosion yield for Nevada Test Site explosions. He also applied his measurement methods to Semipalatinsk explosions (Nuttli, 1986b), using available WWSSN records to estimate m_b(Lg) and yields of these events.

Ringdal (1983) first suggested a method to determine Lg magnitudes based on digitally recorded array data. The main idea was to improve the precision of such estimates by averaging over time (computing RMS values over an extended Lg window), frequency (using a bandpass filter covering all frequencies with significant Lg energy) and space (by averaging individual array elements). For a detailed description of the method and initial studies, reference is made to Ringdal and Hokland (1987); and Ringdal and Fyen (1988).

In this paper, we present some additional results from analysis of NORSAR and Gräfenberg Lg recordings of presumed underground explosions at the Shagan River area near Semipalatinsk, USSR. In particular, relative to earlier results, the Gräfenberg data base has been expanded to include all available recordings from these events. Furthermore, we

have assessed the effects of introducing station corrections for individual array elements and epicentral distance corrections in the estimation procedure. The precision in the estimates has been investigated taking into account the signal-to-noise ratios, and a comparative analysis of NORSAR and Gräfenberg Lg measurements has been carried out.

Data sources

The NORSAR array (Bungum, Husebye and Ringdal, 1971) was established in 1970, and originally comprised 22 subarrays, deployed over an area of 100 km diameter. Since 1976 the number of operational subarrays has been 7, comprising altogether 42 vertical-component SP sensors (type HS-10). In this paper, analysis has been restricted to data from these 7 subarrays. Sampling rate for the NORSAR SP data is 20 samples per second, and all data are recorded on digital magnetic tape.

The Gräfenberg array (Harjes and Seidl, 1978) was established in 1976, and today comprises 13 broadband seismometer sites, three of which are 3-component systems. The instrument response is flat to velocity from about 20 second period to 5 Hz. Sampling rate is 20 samples per second, and the data are recorded on digital magnetic tape.

The location of NORSAR and Gräfenberg relative to Semipalatinsk is shown in Fig. VII.6.1, where also the propagation paths to the two arrays are indicated.

Based on ISC and NEIC reports, a total of 94 events, presumed to be nuclear explosions at the Shagan River area, have been selected as a data base. The time span is from 1965 to September 14, 1988, when the second Joint Verification Experiment (JVE) explosion was carried out. Table VII.6.1 lists the dates of these events together with pertinent measurements discussed later in the text.

Data analysis

All available recordings from NORSAR and GRF have been analyzed for the event set of 94 Shagan River explosions, using the procedure described by Ringdal and Hokland (1987).

Briefly, this procedure comprises filtering all array channels with a 0.6-3.0 Hz bandpass filter, computing RMS value of each filtered trace in a 2-minute Lg window (starting 12 min after P onset for NORSAR, 14 min for GRF), and compensating for background noise preceding P-onset. The Lg magnitude is then estimated by logarithmic averaging across each array.

The total number of available recordings with sufficient signal-to-noise ratio to allow reliable Lg measurement was 70 for NORSAR (starting in 1971) and 60 for GRF (starting in 1976).

While the NORSAR array configuration has been stable over the time period considered, the GRF array initially comprised only the four instruments A1 - A4, and was later expanded to its full configuration of 13 sites. In order to reduce as far as possible the bias due to changing array configurations, we have therefore computed station corrections for each individual GRF sensor (Table VII.6.2) and applied these in the array averaging procedure. A similar set of corrections for NORSAR are listed in Table VII.6.3. In practice, the introduction of station corrections has made little difference for the NORSAR magnitude estimates, but had a significant effect for GRF.

The effects of epicentral distance differences on the Lg magnitude estimates have also been assessed. The distance correction $B(\Delta)$ is determined through (Nuttli, 1986b):

$$B(\Delta) = [\sin(\Delta/111) \,/\, \sin(\Delta_0/111)]^{1/2} \cdot \exp[\gamma(\Delta-\Delta_0)]$$

Δ_0 is the distance (km) to a fixed reference location within the epicentral area (for Semipalatinsk we have used 50°N, 49°E) and Δ is the distance (km) to the event. γ is the coefficient of anelastic

attenuation. We have used $\gamma = 0.001$ km^{-1}, which is near the value obtained by Nuttli (1986b) for 1 second Lg waves for paths from Semipalatinsk to Scandinavian stations. Note that a very accurate value of γ is not required when considering a limited source region, as the effects of small variations in this parameter on the resulting m_b(Lg) values are negligible.

The Lg magnitudes at NORSAR and GRF of events in the data base are listed in Table VII.6.1. Since these estimates take into account both station terms and epicentral distance corrections, they are slightly different from values published earlier, but nevertheless in good agreement.

Table VII.6.1 also contains estimated standard deviations of the Lg magnitudes, taking into account both the scattering across each array, the signal-to-noise ratios and the variance reduction obtained by the averaging procedure (see Appendix). We emphasize that these standard deviations are indicative only of the precision of measurement, and should not be interpreted as being representative of the accuracy of these magnitudes as source size estimators. We note that magnitudes of the larger explosions may be measured with very high precision, whereas the uncertainty is greater for the smaller events, due to the lower signal-to-noise ratios. It is also clear that the NORSAR-based estimates are more precise than those using GRF data, especially for events for which full GRF array recordings are not available.

Fig. VII.6.2 shows a scatter plot of NORSAR versus GRF magnitudes for all common events. The straight line represents a least squares fit to the data, assuming no errors in NORSAR magnitudes. We note that the two arrays show excellent consistency, although there is some increase in the scattering at low magnitudes. The standard deviation of the differences relative to the least squares fit is 0.045 magnitude units. Also there is no significant separation between events from NE and SW Shagan with regard to the relative Lg magnitudes observed at the two arrays.

In Fig. VII.6.3 a similar plot is shown, including only "well-recorded" events, i.e., requiring at least 5 operational GRF channels and a standard deviation of each array estimate not exceeding 0.04 magnitude units. The slope of the straight line fit has been restricted to the same value (1.15) as in Fig. VII.6.2. We note that there is a significant reduction in the scatter, and the standard deviation of the residuals is only 0.032 magnitude units. Thus the Lg magnitudes measured at the two arrays show excellent consistency for high signal-to-noise ratio events.

The slope (1.15) of the straight-line fit in Fig. VII.6.2 is slightly greater than 1.00, a tendency also noted by Ringdal and Fyen (1988): The interpretation of this observation is somewhat uncertain; a possible explanation is scaling differences in the Lg source spectrum (Kværna and Ringdal, 1988), in combination with the response differences of the NORSAR and GRF instruments. We have attempted to compare the two data sets after adjusting the GRF recordings to a NORSAR-type response. However, the results were inconclusive since the GRF signal-to-noise ratio then became too low for the smaller events.

Fig. VII.6.4 illustrates the pattern of P-Lg bias in the Shagan River area, using m_b values computed at Blacknest (Marshall, personal communication) together with combined NORSAR/GRF Lg magnitudes. The latter have been derived by adjusting the GRF magnitudes to an "equivalent" NORSAR value using the straight-line relation of Fig. VII.6.3, and then calculating a weighted average using the inverse variances (Table VII.6.1) as weighting factors. Fig. VII.6.4 includes all events of $m(Lg) \geq 5.6$, assuming either two-array observations or very precise Lg measurements from one array ($\sigma < 0.04$).

Although both the m_b values and the Lg magnitudes have been revised relative to those used in earlier studies, Fig. VII.6.4 confirms the observations previously made regarding the systematic difference between P-Lg residuals from NE and SW Shagan. In the NE area, $m_b(P)$ is generally lower than m(Lg), whereas the opposite behavior is seen in the SW portion. The JVE explosion of 14 September 1988 has a P-Lg bias

of 0.06 which is close to the average for the SW region. Furthermore, there appears to be a transition zone between the two portions of the test site, where the residuals are close to zero.

Conclusions

From this and previous studies, we can conclude that the Lg RMS estimation methods provide very stable, mutually consistent results when applied to two widely separated arrays (NORSAR and GRF). This is of clear significance regarding the potential use of such Lg measurements for yield estimation. Further research will be directed toward expanding the data base by conducting similar studies using other available station data as well as studying Lg recordings from other test sites. In particular, seismic data that might become available from USSR stations in the future would be of importance both in further assessing the stability of the estimates and to obtain Lg magnitudes for explosions of low yields.

F. Ringdal
J. Fyen

References

Baumgardt, D.R. (1985): Comparative analysis of teleseismic P coda and Lg waves from underground explosions in Eurasia. Bull. Seism. Soc. Amer., 75, 1413-1433.

Bungum, H., E.S. Husebye and F. Ringdal (1971): The NORSAR array and preliminary results of data analysis. Geophys. J., 25, 115-126.

Harjes, H.-P. and D. Seidl (1978): Digital recording and analysis of broadband seismic data at the Gräfenberg (GRF) array. J. Geophys. Res., 44, 511-523.

Kværna, T. and F. Ringdal (1988): Spectral analysis of Shagan River explosions recorded at NORSAR and NORESS (This volume).

Nuttli, O.W. (1973): Seismic wave attenuation and magnitude relations for eastern North America. J. Geophys. Res., 78, 876-885.

Nuttli, O.W. (1986a): Yield estimates of Nevada test site explosions obtained from seismic Lg waves. J. Geophys. Res., 91, 2137-2151.

Nuttli, O.W. (1986b): Lg magnitudes of selected East Kazakhstan underground explosions. Bull. Seism. Soc. Amer., 76, 1241-1251.

Ringdal, F. (1983): Magnitudes from P coda and Lg using NORSAR data. In: NORSAR Semiannual Tech. Summ., 1 Oct 1982 - 31 Mar 1983, NORSAR Sci. Rep. 2-82/83, Kjeller, Norway.

Ringdal, F. and B.Kr. Hokland (1987): Magnitudes of large Semipalatinsk explosions using P coda and Lg measurements at NORSAR. In: Semiannual Tech. Summ., 1 Apr - 30 Sep 1987, NORSAR Sci. Rep. 1-87/88, Kjeller, Norway.

Ringdal, F. and J. Fyen (1988): Analysis of Gräfenberg Lg recordings of Semipalatinsk explosion. In: Semiannual Tech. Summ., 1 Oct 1987 - 31 Mar 1988, NORSAR Sci. Rep. 2-87/88, Kjeller, Norway.

No.	ORIGIN DATE	ORIGIN TIME	MB	**** NORSAR **** M(LG)	N	STD	***** GRF ***** M(LG)	N	STD
1	01/15/65	5 59 58	5.8	-	-	-	-	-	-
2	06/19/68	5 05 57	5.4	-	-	-	-	-	-
3	11/30/69	3 32 57	6.0	-	-	-	-	-	-
4	06/30/71	3 56 57	5.2	-	-	-	-	-	-
5	02/10/72	5 02 57	5.4	-	-	-	-	-	-
6	11/02/72	1 26 57	6.1	6.116	42	0.014	-	-	-
7	12/10/72	4 27 7	6.0	6.115	42	0.009	-	-	-
8	07/23/73	1 22 57	6.1	6.195	40	0.006	-	-	-
9	12/14/73	7 46 57	5.8	5.866	42	0.033	-	-	-
10	04/16/74	5 52 57	4.9	-	-	-	-	-	-
11	05/31/74	3 26 57	5.9	-	-	-	-	-	-
12	10/16/74	6 32 57	5.5	5.409	42	0.024	-	-	-
13	12/27/74	5 46 56	5.6	5.711	42	0.056	-	-	-
14	04/27/75	5 36 57	5.6	5.547	42	0.057	-	-	-
15	06/30/75	3 26 57	5.0	-	-	-	-	-	-
16	10/29/75	4 46 57	5.8	5.628	42	0.046	-	-	-
17	12/25/75	5 16 57	5.7	5.794	42	0.035	-	-	-
18	04/21/76	5 2 57	5.3	-	-	-	-	-	-
19	06/09/76	3 2 57	5.3	5.200	42	0.089	-	-	-
20	07/04/76	2 56 57	5.8	5.811	42	0.009	5.785	4	0.024
21	08/28/76	2 56 57	5.8	5.734	41	0.013	5.654	3	0.052
22	11/23/76	5 02 57	5.8	-	-	-	5.794	3	0.057
23	12/07/76	4 56 57	5.9	-	-	-	5.702	3	0.088
24	05/29/77	2 56 57	5.8	5.673	41	0.035	5.570	3	0.038
25	06/29/77	3 6 58	5.3	5.031	40	0.110	-	-	-
26	09/05/77	3 2 57	5.8	5.893	40	0.017	5.768	3	0.036
27	10/29/77	3 7 2	5.6	5.788	41	0.043	5.685	3	0.041
28	11/30/77	4 06 57	6.0	-	-	-	5.716	3	0.041
29	06/11/78	2 56 57	5.9	5.750	39	0.029	5.724	4	0.039
30	07/05/78	2 46 57	5.8	5.795	39	0.010	-	-	-
31	08/29/78	2 37 6	5.9	6.009	39	0.008	6.001	6	0.022
32	09/15/78	2 36 57	6.0	5.908	38	0.018	-	-	-
33	11/04/78	5 5 57	5.6	5.672	39	0.088	5.624	6	0.080
34	11/29/78	4 33 2	6.0	5.969	39	0.013	5.828	2	0.075
35	02/01/79	4 12 57	5.4	-	-	-	-	-	-
36	06/23/79	2 56 57	6.2	6.056	21	0.009	6.113	4	0.021
37	07/07/79	3 46 57	5.8	5.968	38	0.008	5.940	7	0.021
38	08/04/79	3 56 57	6.1	6.101	39	0.008	6.106	9	0.015
39	08/18/79	2 51 57	6.1	-	-	-	6.138	7	0.017
40	10/28/79	3 16 56	6.0	6.054	34	0.010	6.050	8	0.023
41	12/02/79	4 36 57	6.0	5.916	28	0.021	5.949	10	0.025
42	12/23/79	4 56 57	6.2	-	-	-	6.042	9	0.021
43	04/25/80	3 56 57	5.5	-	-	-	-	-	-
44	06/12/80	3 26 57	5.6	-	-	-	5.575	11	0.105
45	06/29/80	2 32 57	5.7	5.680	16	0.026	5.744	8	0.046
46	09/14/80	2 42 39	6.2	-	-	-	-	-	-
47	10/12/80	3 34 14	5.9	5.927	28	0.013	5.938	13	0.034
48	12/14/80	3 47 6	5.9	5.931	28	0.018	5.948	10	0.027
49	12/27/80	4 9 8	5.9	5.936	27	0.014	5.886	11	0.034
50	03/29/81	4 3 50	5.6	5.555	28	0.085	5.439	11	0.184

Table VII.6.1. List of presumed explosions at the Shagan River test area near Semipalatinsk, USSR. The m_b values are those published in the ISC bulletins for events prior to 1986, and are otherwise taken from NEIC/PDE reports. NORSAR and Gräfenberg Lg RMS magnitudes are given for all events with available recordings of sufficient signal-to-noise ratio. The number of data channels used and the estimated precision of measurements (see Appendix) are given for each magnitude value. (Page 1 of 2).

No.	ORIGIN DATE	ORIGIN TIME	MB	**** NORSAR **** M(LG)	N	STD	***** GRF ***** M(LG)	N	STD
51	04/22/81	1 17 11	6.0	5.907	28	0.022	5.956	11	0.027
52	05/27/81	3 58 12	5.5	5.456	27	0.023	-	-	-
53	09/13/81	2 17 18	6.1	6.114	29	0.008	6.109	9	0.015
54	10/18/81	3 57 2	6.1	5.984	34	0.010	5.956	9	0.021
55	11/29/81	3 35 8	5.7	5.545	28	0.121	5.512	12	0.192
56	12/27/81	3 43 14	6.2	6.071	34	0.009	6.050	9	0.021
57	04/25/82	3 23 5	6.1	6.078	35	0.008	6.069	10	0.017
58	07/04/82	1 17 14	6.1	-	-	-	-	-	-
59	08/31/82	1 31 0	5.3	-	-	-	-	-	-
60	12/05/82	3 37 12	6.1	5.988	31	0.019	6.001	13	0.020
61	12/26/82	3 35 14	5.7	5.655	39	0.080	5.598	13	0.067
62	06/12/83	2 36 43	6.1	6.073	25	0.009	-	-	-
63	10/06/83	1 47 6	6.0	5.867	19	0.033	5.851	11	0.040
64	10/26/83	1 55 4	6.1	5.999	33	0.021	6.035	11	0.020
65	11/20/83	3 27 4	5.5	-	-	-	-	-	-
66	02/19/84	3 57 3	5.9	5.723	29	0.038	-	-	-
67	03/07/84	2 39 6	5.7	5.695	29	0.065	5.575	12	0.108
68	03/29/84	5 19 8	5.9	5.899	29	0.012	5.961	13	0.043
69	04/25/84	1 9 3	6.0	5.869	35	0.008	5.804	13	0.031
70	05/26/84	3 13 12	6.0	6.073	33	0.007	6.132	13	0.015
71	07/14/84	1 9 10	6.2	6.055	32	0.007	6.066	12	0.015
72	09/15/84	6 15 10	4.7	-	-	-	-	-	-
73	10/27/84	1 50 10	6.2	6.082	33	0.011	6.143	13	0.016
74	12/02/84	3 19 6	5.8	5.881	29	0.020	5.864	12	0.036
75	12/16/84	3 55 2	6.1	6.046	29	0.010	6.037	13	0.014
76	12/28/84	3 50 10	6.0	5.982	35	0.009	5.944	13	0.021
77	02/10/85	3 27 7	5.9	5.801	40	0.024	5.800	13	0.058
78	04/25/85	0 57 6	5.9	5.859	29	0.045	5.848	7	0.047
79	06/15/85	0 57 0	6.0	5.976	30	0.009	6.031	13	0.017
80	06/30/85	2 39 2	6.0	5.928	30	0.009	5.905	12	0.018
81	07/20/85	0 53 14	5.9	5.858	37	0.013	5.867	12	0.031
82	03/12/87	1 57 17	5.5	5.215	33	0.076	-	-	-
83	04/03/87	1 17 8	6.2	6.051	33	0.008	6.126	11	0.017
84	04/17/87	1 3 4	6.0	5.898	33	0.020	5.912	12	0.026
85	06/20/87	0 53 4	6.1	5.968	36	0.007	5.943	10	0.028
86	08/02/87	0 58 6	5.9	-	-	-	5.856	11	0.022
87	11/15/87	3 31 6	6.0	5.973	37	0.008	5.983	13	0.022
88	12/13/87	3 21 4	6.1	6.091	31	0.010	6.066	12	0.015
89	12/27/87	3 5 4	6.1	6.046	31	0.011	6.032	13	0.019
90	02/13/88	3 5 5	6.1	6.042	26	0.009	6.047	13	0.029
91	04/03/88	1 33 5	6.1	6.067	31	0.007	6.076	13	0.014
92	05/04/88	0 57 6	6.1	6.040	31	0.008	6.064	13	0.020
93	06/14/88	2 27 6	4.9	-	-	-	-	-	-
94	09/14/88	4 0 0	6.0	5.969	37	0.010	5.970	12	0.043

Table VII.6.1. (Page 2 of 2)

CHANNEL NO	BIAS	N	STD
1	0.15	24	0.029
2	0.15	31	0.031
3	0.19	24	0.042
4	0.08	19	0.034
5	0.01	12	0.046
6	-0.11	18	0.030
7	0.01	16	0.041
8	0.09	15	0.036
9	-0.09	19	0.039
10	-0.15	13	0.024
11	-0.04	7	0.033
12	-0.17	12	0.039
13	-0.12	14	0.045

Table VII.6.2. List of station terms (station RMS Lg value minus array average) for the Gräfenberg array. The 13 individual vertical component seismometers are listed in the sequence A1-4, B1-5 and C1-4. The bias values are based on high signal-to-noise ratio events recorded by at least 10 channels. The number of observations and the sample standard deviation is listed for each instrument.

CHANNEL NO	BIAS	N	STD
1	0.05	49	0.051
2	0.11	31	0.044
3	0.17	23	0.044
4	0.04	6	0.025
5	0.10	45	0.028
6	-0.01	49	0.060
7	0.01	43	0.033
8	0.08	39	0.045
9	-0.01	42	0.029
10	0.13	42	0.036
11	0.00	34	0.047
12	0.05	43	0.042
13	0.03	48	0.038
14	-0.11	48	0.028
15	-0.01	49	0.033
16	-0.01	49	0.035
17	0.03	49	0.032
18	-0.02	49	0.040
19	-0.02	43	0.033
20	-0.01	44	0.043
21	-0.05	45	0.034
22	-0.05	45	0.024
23	-0.03	44	0.049
24	-0.04	46	0.022
25	-0.10	45	0.031
26	0.02	45	0.037
27	-0.07	44	0.027
28	-0.08	45	0.023
29	-0.02	45	0.031
30	-0.02	45	0.038
31	-0.06	42	0.031
32	-0.01	42	0.025
33	-0.03	41	0.047
34	-0.02	43	0.033
35	-0.04	44	0.029
36	0.01	40	0.055
37	-0.04	21	0.031
38	-0.05	32	0.030
39	0.01	20	0.064
40	-0.01	19	0.046
41	0.02	18	0.036
42	0.05	20	0.029

Table VII.6.3. List of station terms (station RMS Lg value minus array average) for the NORSAR array. The 42 individual seismometers are listed in the standard sequence (subarrays 01A through 06C). The bias values are based on events with high signal-to-noise ratio (Lg magnitude > 5.8). The number of observations and the sample standard deviation are listed for each instrument.

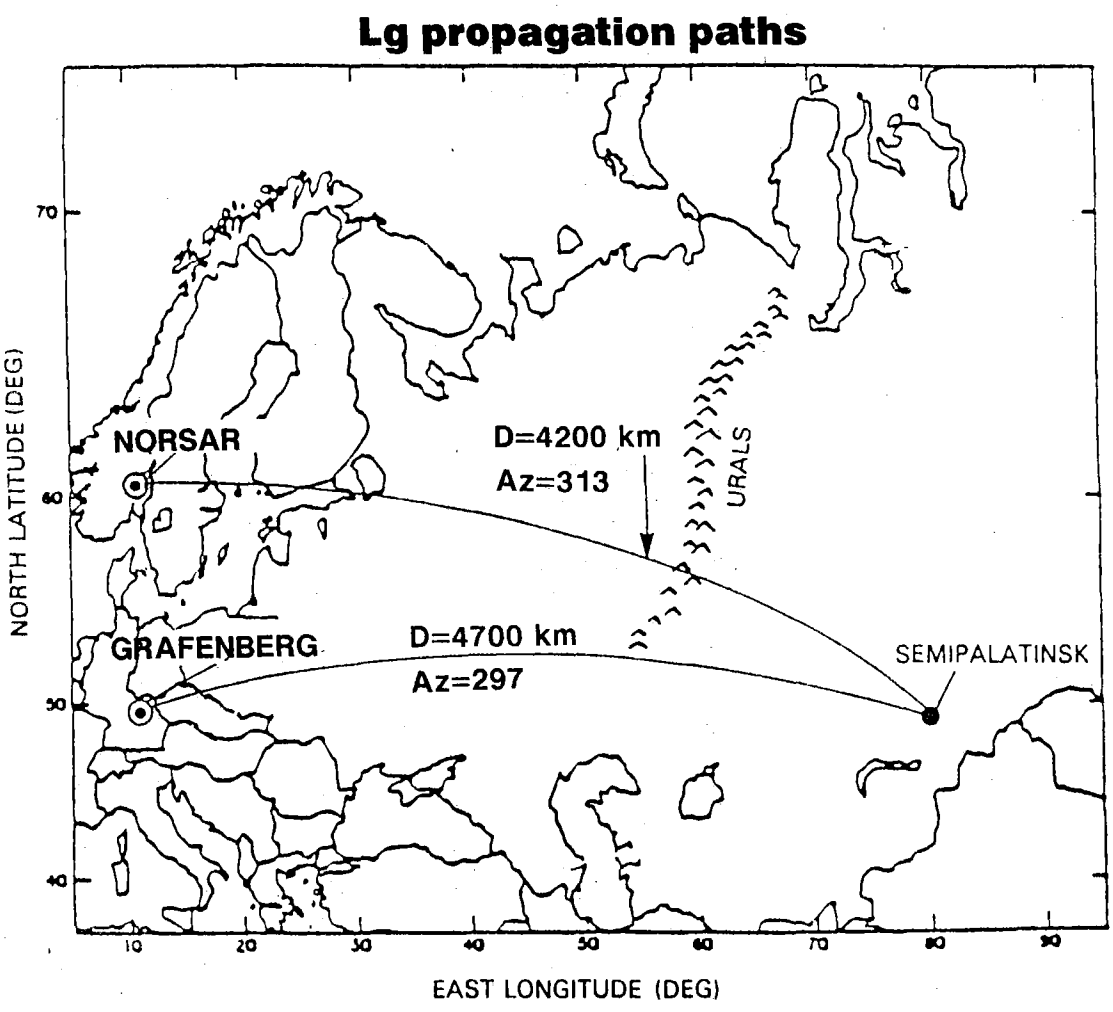

Fig. VII.6.1. Location of the NORSAR and Gräfenberg arrays in relation to the Semipalatinsk test site.

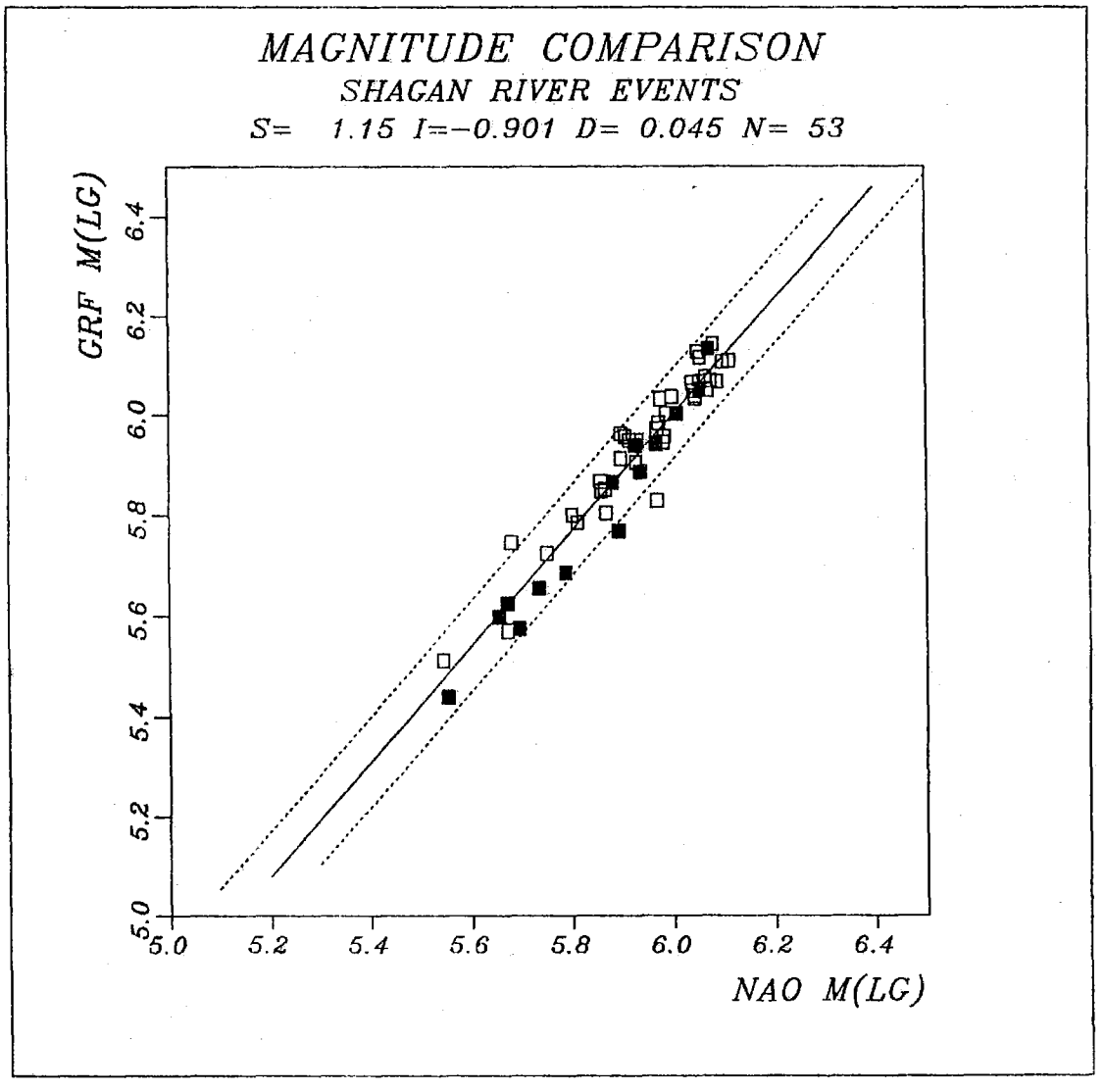

Fig. VII.6.2. Plot of Gräfenberg (GRF) versus NORSAR (NAO) Lg magnitudes for Shagan River explosions. The figure includes all common events in Table VII.6.1. Events in the NE and SW parts of Shagan are marked as filled squares and open squares, respectively. The straight line (slope 1.15) represents a least squares fit to the data, assuming no error in NORSAR Lg measurements. The standard deviation of the residuals along the vertical axis relative to the straight line is 0.045, and the dotted lines correspond to plus/minus two standard deviations.

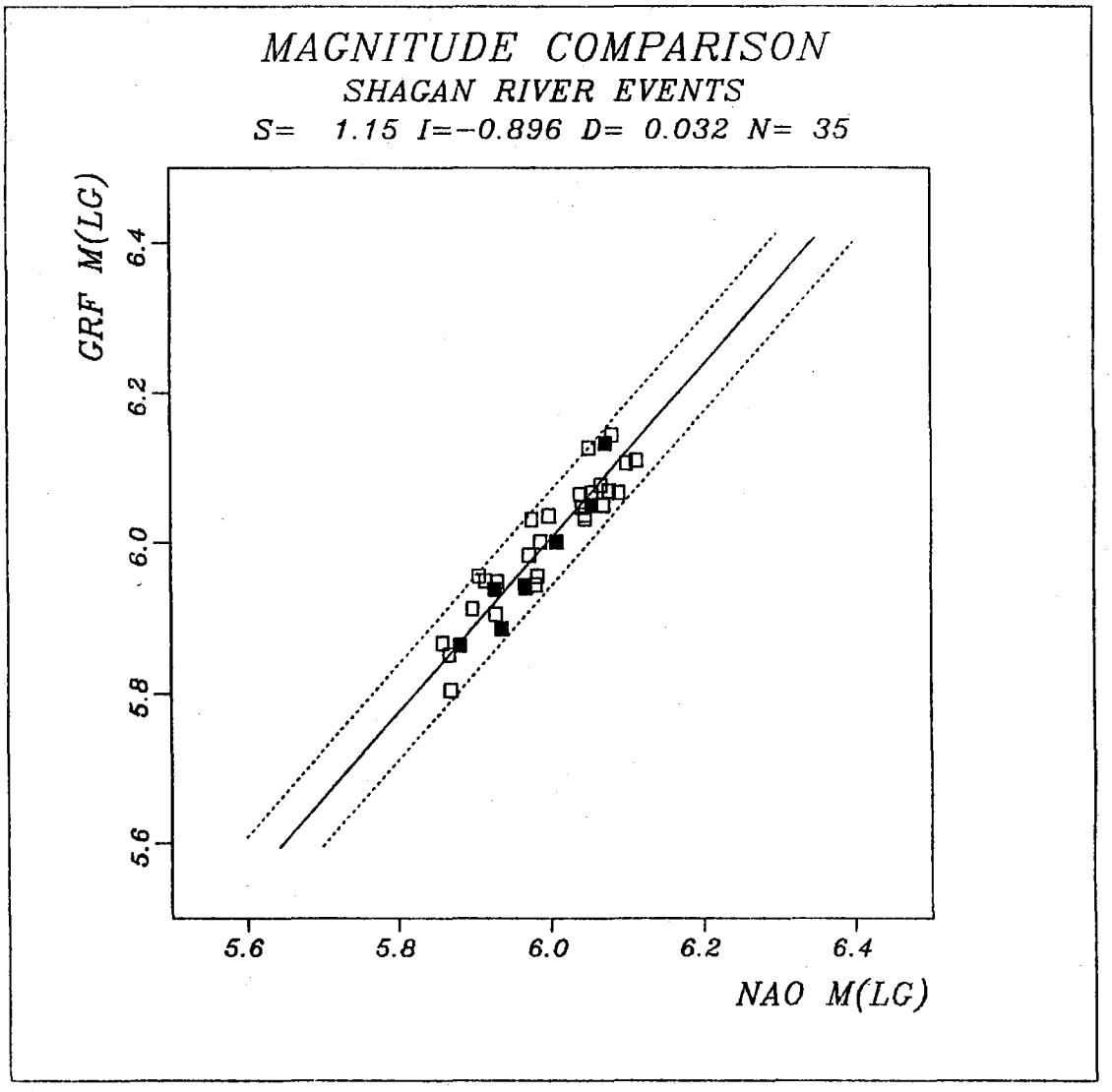

Fig. VII.6.3. Same as Fig. VII.6.2, but showing only "well-recorded" events, i.e., requiring at least 5 operational GRF channels and a standard deviation of each array estimate not exceeding 0.04. The slope of the straight line has been restricted to the value obtained in Fig. VII.6.2. Note that the scatter in the data has been significantly reduced, and the standard deviation in the vertical direction is only 0.032 magnitude units for this data set.

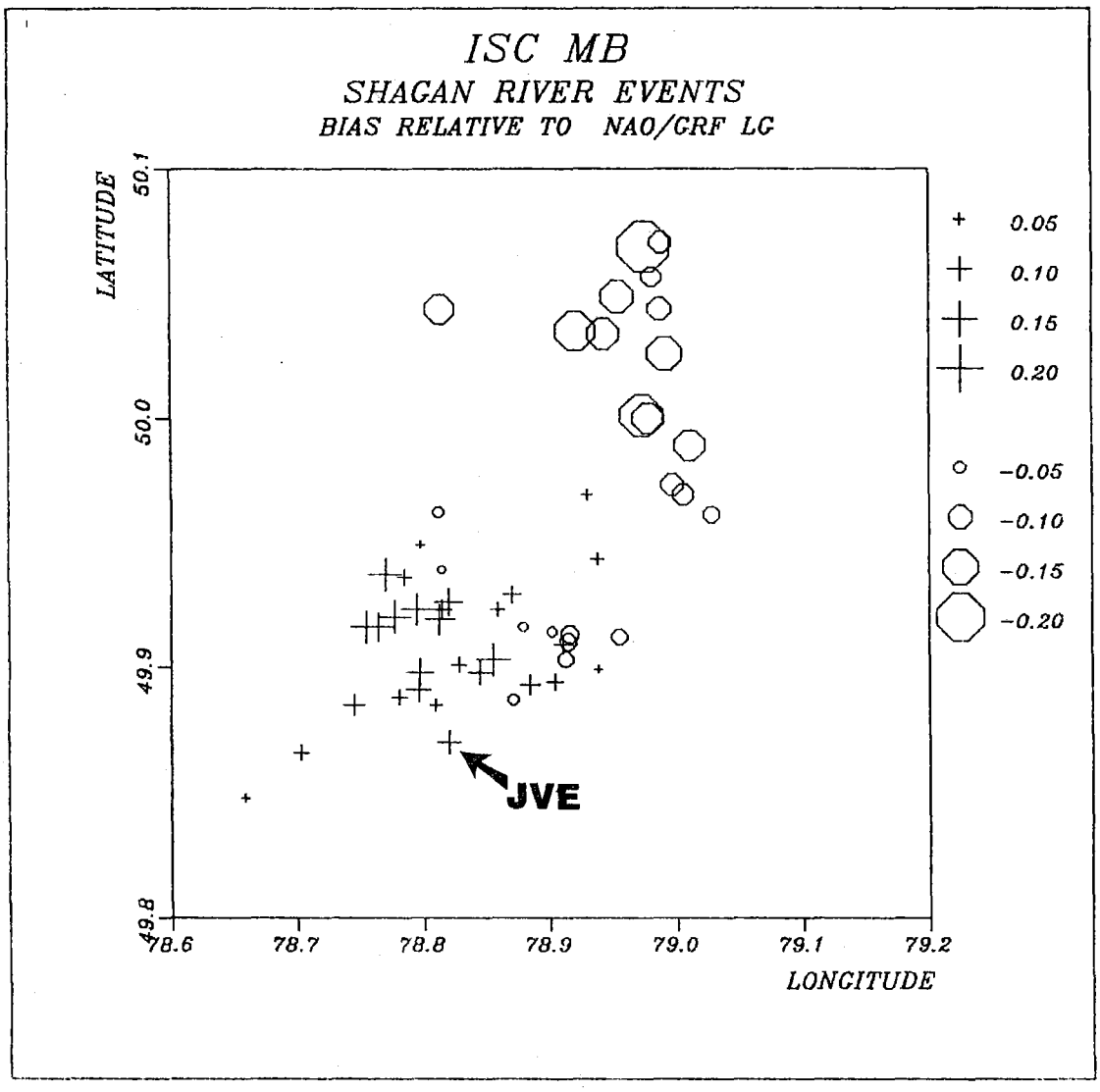

Fig. VII.6.4. Plot of P-Lg magnitude residuals (ISC maximum likelihood minus NORSAR/Gräfenberg Lg magnitudes) as a function of event location (Marshall, personal communication) within the Shagan River area. Plusses and circles correspond to residuals greater or less than the average, respectively, with symbol size proportional to the deviation. All events of $m_b(Lg) \geq 5.6$ for which we have precise locations have been included, assuming either two-array observations or very precise Lg measurements from one array. The JVE explosion is especially marked. Note the systematic variation from NE to SW Shagan, with an apparent transition zone in between.

Appendix to Section VII.6

In this appendix we develop an approximate expression for the uncertainty in the RMS Lg magnitude estimates described earlier. We first consider the case of a single sensor measurement, and afterwards address the array averaging procedure.

Denote by $x_1(t)$ the recorded signal in the "Lg window", and assume that this is composed of a noise component $x_2(t)$ and a signal component $x_3(t)$ as follows:

$$x_1(t) = x_2(t) + x_3(t) \qquad (1)$$

Here, we assume that the noise component $x_2(t)$ can be modelled as a zero-mean random process which is stationary over a time interval long enough to include both the Lg window and a suitable noise window preceding the P onset. The signal $x_3(t)$ is considered a zero-mean random process defined in the Lg time window, and being uncorrelated with $x_2(t)$.

We can thus obtain an estimate of the mean square value X_3 of $x_3(t)$ by

$$X_3 = X_1 - X_2 \qquad (2)$$

where X_1 is the mean square value of $x_1(t)$ in the signal window, and X_2 is the mean square value of $x_2(t)$ in the noise window.

The Lg RMS magnitude is then (apart from an additive constant) determined as $\log_{10} \sqrt{X_3}$.

We now make the assumption that the quantities X_i $(i=1,\ldots,3)$ each follow a lognormal distribution, when considered as random variables. We emphasize that this assumption, which is reasonable in view of empirical studies of logarithmic amplitude patterns of signals and noise, represents an approximation only. Thus, we know that the

difference between two lognormal variables is usually not another lognormal variable, but for our purposes this approximation is useful.

We may thus write (using natural logarithms):

$$\log X_i \text{ is } N(m_i, 4\sigma_i^2) \qquad i = 1,\ldots,3 \tag{3}$$

Note that using $4\sigma_i^2$ as the variance of $\log X_i$ corresponds to σ_i^2 representing the variance of the log RMS estimate.

The mean and variances of the respective variables can then be expressed by (Aitchison and Brown, 1969):

$$EX_i = e^{m_i+2\sigma_i^2} \qquad i = 1,\ldots,3 \tag{4}$$

$$\text{var } X_i = (EX_i)^2 \cdot (e^{4\sigma_i^2} - 1) \qquad i = 1,\ldots,3 \tag{5}$$

From eq. (2) we furthermore obtain

$$EX_3 = EX_1 - EX_2 \tag{6}$$

$$\text{var } X_3 = \text{var } X_1 + \text{var } X_2 \tag{7}$$

Combining (5) and (7), this leads to the relation:

$$(EX_2 - EX_1)^2 \cdot (e^{4\sigma_3^2} - 1) = (EX_1)^2 \cdot (e^{4\sigma_1^2} - 1) + (EX_2)^2 \cdot (e^{4\sigma_2^2} - 1) \tag{8}$$

Substituting EX_1 and EX_2 by the observed values $\hat{X}_1$ and $\hat{X}_2$, respectively, and assuming small values of σ_i ($i = 1,\ldots,3$) we obtain from (8) the following simplified relation:

$$\sigma_3^2 = \frac{\sigma_1^2 \cdot \hat{X}_1^2 + \sigma_2^2 \cdot \hat{X}_2^2}{(\hat{X}_1 - \hat{X}_2)^2} \qquad (9)$$

which represents an approximate expression for the variance of $\log\sqrt{X_3}$. Note that (9) is developed using natural logarithms, it applies without change if base 10 logarithms are used throughout.

Although we have used a number of simplifications in arriving at (9), simulation experiments using randomly generated distributions have shown that this formula gives a useful approximation to the actual scatter in the estimates within a reasonable range of parameter values.

We note that in cases of high signal-to-noise ratios, (i.e., $\hat{X}_1 \gg \hat{X}_2$), we obtain from (9) $\sigma_3^2 \approx \sigma_1^2$; thus the noise variance has no significant effect on the Lg magnitude variance. On the other hand, as the signal-to-noise ratio becomes small, the variance σ_3^2 will increase rapidly.

In the array averaging procedure, we assume that the term σ_1^2 is reduced in proportion to the number of array elements, whereas we consider σ_2^2 to represent mainly a systematic noise fluctuation that is not reduced through array averaging.

Defining the signal-to-noise ratio α by $\alpha = \hat{X}_1/\hat{X}_2$, and denoting by N the number of array elements, we thus obtain from (9)

$$\sigma_3^2 = \frac{(\sigma_1^2 \cdot \alpha^2)/N + \sigma_2^2}{(\alpha - 1)^2} \qquad (10)$$

As a numerical example, consider the JVE explosion (event 94 in Table VII.6.1).

For NORSAR, we have estimated $\alpha = 13.12$, with $N = 37$, and we assume $\sigma_1 = 0.04$, $\sigma_2 = 0.08$. Formula (10) then gives $\sigma_3 = 0.010$.

For GRF, we have $\alpha = 3.03$, with $N = 12$, and the same input σ values as above then give $\sigma_3 = 0.043$. Thus, the estimated uncertainty of the GRF Lg magnitude is considerably greater than that of NORSAR, the main reason being the lower signal-to-noise ratio for GRF.

Reference

Aitchison, J. and J.A.C. Brown (1969): The Lognormal Distribution, Cambridge University Press, UK.